7-2-2020

Hydrogeophysical Characterization and Imaging in the Mangrove Lakes Region of Everglades National Park and Big Pine Key, Florida, USA

Michael Eyob Kiflai
mkifl001@fiu.edu

FLORIDA INTERNATIONAL UNIVERSITY

Miami, Florida

HYDROGEOPHYSICAL CHARACTERIZATION AND IMAGING IN THE MANGROVE LAKES REGION OF EVERGLADES NATIONAL PARK AND BIG PINE KEY, FLORIDA, USA

A dissertation submitted in partial fulfillment of

the requirements for the degree of

DOCTOR OF PHILOSOPHY

in

EARTH SYSTEM SCIENCE

by

Michael Eyob Kiflai

2020

To: Dean Michael R. Heithaus
College of Arts, Science and Education

This dissertation, written by Michael Eyob Kiflai, and entitled Hydrogeophysical Characterization and Imaging in the Mangrove Lakes Region of Everglades National Park and Big Pine Key, Florida, USA, having been approved in respect to style and intellectual content, is referred to you for judgment.

We have read this thesis and recommend that it be approved.

_____
René M. Price

_____
Assefa M. Melesse

_____
Pete E. Markowitz

_____
Dean Whitman, Major Professor

Date of Defense: July 02, 2020

The dissertation of Michael Eyob Kiflai is approved.

_____
Dean Michael R. Heithaus
College of Arts, Science and Education

_____
Andrés G. Gil
Vice President for Research and Economic Development
and Dean of the University Graduate School

Florida International University, 2020

DEDICATION

I dedicate this dissertation work to my father Eyob Kiflai, my mother Almaz Tekie, and my siblings Shewit, Hermon, Merhawi, Adonay, Metkel, and Medhanie. Without their support and love, the completion of this work would not have been possible.

ACKNOWLEDGMENTS

I would like to thank my committee members, Dr. Dean Whitman, Dr. René Price, Dr. Assefa Melesse, and Dr. Pete Markowitz, for their support and guidance. My sincere appreciation to my advisor Dr. Dean Whitman for his supervision, valuable discussion, and selfless willingness assistance in the field and lab during the past five years. I extended my gratitude to Dr. René Price for securing funding for the project and valuable suggestions. I am deeply indebted to Dr. Assefa Melesse for his continuous encouragement and taught me the Water Resources Assessment and GIS in Water Resources. I am grateful to Dr. Pete Markowitz for his guidance and motivation.

I wish to extend my appreciation for Tom A. Frankovich, Henok T Tewelde, Michael Ross, Danielle Oguracak, and Michael Sukop. They were generous to share their technical advice on the geophysical surveys, ecosystem dynamics, and groundwater modeling. I am indebted to Tom A. Frankovich, Joshua Allen, Nicole Tucker, Alejandro Garcia, Himadri Biswas, Temesgen Gebrekidan, and Lazaro Oliva, who contributed to the data acquisition. I extend my gratitude to Thomas Anthony for his dedication and technical assistance in designing the floating electrical resistivity array. I would also like to thank Gail Excell, Diane Pirie, Andrew Joesoef, Rafael Gonzalez for coordination office work and logistics needed for the fieldwork.

I thank South Florida Water Management District (SFWMD) for funding the geophysical mangrove lakes of Everglades National Park project and the US Fish and Wildlife Service (USFWF) for funding the Hurricane Irma project in Big Pine Key, FL. I am grateful for the support I received from Florida International University (FIU) Graduate School through teaching assistantship and the Dissertation Year Fellowship (DYF).

My most profound appreciation to my brother Hermon Eyob, for his sacrifices, to assist my family and me throughout my study and my fiancé Tedora Tsegay Tewelde for her understanding and encouragement during the last five years.

ABSTRACT OF THE DISSERTATION

HYDROGEOPHYSICAL CHARACTERIZATION AND IMAGING IN THE MANGROVE LAKES REGION OF EVERGLADES NATIONAL PARK AND BIG PINE KEY, FLORIDA, USA

by

Michael Eyob Kiflai

Florida International University, 2020

Miami, Florida

Professor Dean Whitman, Major Professor

Coastal groundwater aquifers are susceptible to saltwater intrusion from natural and anthropogenic sources. Everglades National Park (ENP) has been adversely impacted by past human activities that altered freshwater flow through the system. In Big Pine Key (BPK), the flat and low-lying topography less than 2m makes the freshwater lens vulnerable to tidal and storm surge events. This study investigated different inversion scenarios and used Electrical Resistivity Tomography (ERT) and Electromagnetic (EM) survey to characterize the spatial and temporal change of the groundwater chemistry and image the aquifers. In Big Pine Key, Hurricane Irma made landfall as a category 4 storm with storm surge heights in excess of 2 m. The study compared ERT images along three profiles ranging between 220 and 280 m length collected in 2011 with post-storm data collected about 3 to 4 months (November 2017/January 2018) and 8 to 11 months (May/December 2018) after Irma. The post-storm data documented that the storm surge impacted the freshwater lens on all three profiles with low resistivity (i.e., high salinity)

zones in the upper 2 m. These data showed 40 % and 70 % recovery of the freshwater lens in May and December 2018 and most pronounced in the lower elevation of the profiles.

In the Mangrove lakes of the Everglades, a constrained water depth (fixed water layer thickness) inversion model is selected as an effective inversion approach. In our study, we estimated a formation factor 10.7 with a standard deviation of 1.81 by comparing the bulk resistivity measured using a floating Dipole-Dipole array and coincident conductivity data from the wells. Between, 2016 to 2019, the spatial salinity variation on the lakes showed west to east increase in surface water salinity and west to east decrease in groundwater salinity. In addition, the salinity of the surface water and groundwater increased from North to South and suggested freshening of the groundwater and may reflect the effects of increased flow caused by restoration efforts.

TABLE OF CONTENTS

LIST OF TABLES

TABLES PAGE

LIST OF FIGURES

FIGURES PAGE

ABBREVIATIONS AND ACRONYMS

Apparent Conductivity	σ_a
Apparent Resistivity	ρ_a
Cumulative Response Function	R
Depth of Investigation	DOI
Distance between dipoles (coil spacing)	s
Electrical Conductivity	σ
Electrical Resistivity	ρ
Electrical Resistivity Tomography	ERT
Electromagnetic Induction	EMI
Electromagnetism	EM
Everglades National Park	ENP
Frequency	f
Horizontal Coplanar Loops	HCP
Induction Number	D
Low Induction Number	LIN
Magnetic Permeability	μ
Mean sea level	msl
North American vertical datum	NAVD
One Dimension	1-D
Primary Magnetic Field	H^P
Root Mean Square Error	RMS
Secondary Magnetic Field	H^S

Skin Depth	δ
South Florida Water Management District	SFWMD
Three Dimension	3-D
Two Dimension	2-D
United States Geological Survey	USGS
US Fish and Wildlife Service	USFWF
Vertical Coplanar Loops	VCP
Vertical Electrical Soundings	VES

1. Introduction

1.1. Background

Groundwater is one of the most important natural resources worldwide and used for drinking, agriculture, industry, recreation, and environmental activities. It is the world's most extracted raw material, with an estimated withdrawal rate of 982 km^3/year (NGWA 2013). The global distribution of saltwater on earth accounts for 97%, and only 3% is fresh water. Out of the freshwater, 68.7 % is frozen in glaciers and polar ice caps (Igor 1993, NSIDC 2020). The remaining part found as groundwater accounts for 30.1 % with a small fraction in surface and atmospheric water (UNESCO 2015). Coastal groundwater aquifers are susceptible to saltwater intrusion and storm surge caused by natural and anthropogenic sources. In Florida, the Everglades National Park (ENP) has been adversely impacted by past human activities that altered freshwater flow through the system, which results in ecosystem degradation. Besides, the recurrence of storm surge induced disturbance is frequent in Big Pine Key (BPK), FL, yet its impact and recovery rate of the freshwater lens is not well documented. Therefore, mapping of the freshwater resources and regularly monitoring the hydrological condition is required for proper water management practice and conservation actions.

Geophysical methods such as electrical resistivity and electromagnetics are rapid and noninvasive geophysical methods for measuring groundwater properties and characterizing the spatial and temporal variability of subsurface formations (Binley and Kemna 2005). These methods include electrical and electromagnetic (EM) methods such as DC resistivity, electrical resistivity tomography (ERT), Frequency domain electromagnetic

(FDEM), and time-domain electromagnetic (TDEM) surveying. These methods are commonly used in near-surface geophysics because the subsurface electrical properties are easily correlated to the physical and chemical properties of fluids within the pore space (Binley 2015). These methods can produce a high-resolution image of the shallow subsurface formation and have been widely used in hydrogeology and environmental studies.

Geophysical methods have been used increasingly in groundwater and surface water interaction study. Generally, the near-surface geophysical technique aims at (1) characterization of the subsurface formation, (2) delineating the groundwater and surface interaction zones, and (3) monitoring the hydrological dynamics (McLachlan 2017). Specific examples include detection depth to bedrock, depth to the water table, saltwater intrusion dynamics, contaminant transport, mapping of lithology, aquifer storage recharge, and so on. Some limitations of the geophysical methods include measurement scale and resolution if the target area is small (Binley 2015), non-uniqueness of the solution (Loke et al. 2013; Day-Lewis et al. 2006), and calibration problems in EM methods (Tan et al. 2019).

In this study, to overcome some of the challenges, we compared 1-D constrained and unconstrained electrical resistivity and EM inversion methods. In addition, we proposed a multi-linear regression EM calibration approach. Furthermore, we focused on evaluating the spatial and temporal changes in the groundwater chemistry in the Mangrove Lakes of Everglades National Park (ENP) using electrical and electromagnetic geophysical surveys and surface water and groundwater sampling. Understanding the hydrochemistry of the aquifer can help to establish sustainable water resources management. Secondly, we

focused on assessing the impact of Hurricane Irma storm surge on the freshwater lenses and recovery history in Big Pine Key (BPK) using ERT and well data. Documentation of the freshwater availability will promote conservation actions and management efforts for the habitats.

1.2. Geology of the Study Area

The hydrogeological framework of Florida is comprised of the Floridan aquifer system (FAS) and the surficial aquifer system (SAS). The surficial aquifer system is divided into two flow units, separated by the less permeable semi-confining unit. The SAS is approximately 50 to 80 m thick and comprises the upper Biscayne aquifer flow unit and lower Biscayne flow unit (Cunningham et al. 2001). The Biscayne aquifer is the principal aquifer system in south Florida and declared as a sole-source aquifer. It is one of the most permeable shallow non-artesian (unconfined) aquifers in the world and covers an area of about 10000 square Km (Miller 1990). The aquifer extends along the eastern coast from southern Miami-Dade County into coastal Palm Beach County. The Biscayne aquifer underlies the Everglades as far north as northern Broward County (Fish and Stewart 1991). It is wedge-shaped about 60 m thick near the coast and thins out to west about 12 m near the Everglades (Fish and Stewart 1991).

The geology of the study area consists of Miami formation and Key Largo Limestone. The Miami formation occurs in the southern part of Florida and the southernmost Keys and consists of two facies, namely the Oolitic facies and a bryozoan facies (Neal et al. 2008). The Miami Oolite is composed of white to gray, poorly to moderately consolidated sand and Oolitic limestone, while the bryozoan facies consists of fossiliferous limestone.

In Biscayne aquifer, the porosity ranges from 5.5 % to 79 %, with a maximum porosity around 40 % in most sites (Yeboah-Forson et al. 2014). The highly porous and permeable upper Biscayne aquifer has the highest hydraulic conductivity of average value 2500 m/day and ranges from 2000 m/day to 3000 m/day (Prinos et al. 2014). As a result of the high porosity and permeability, the aquifer is highly susceptible to ground-water contamination and most commonly vulnerable to saltwater encroachment, storm surge, and infiltration of various chemicals and pesticides.

1.3. Electrical and Electromagnetic methods

1.3.1. Electrical Properties of Porous Media

Apparent conductivity and its reciprocal apparent resistivity are commonly used physical parameters in electrical and electromagnetic methods. Apparent conductivity is the conductivity of homogeneous earth that would produce the same electric and /or magnetic fields measured by the instrument. Apparent conductivity (σ) is used mostly in EM methods, and the SI unit is Siemens per meter (S/m). Electrical resistivity is defined as a bulk property of material describing how materials allow electric currents to flow through it. Resistivity is commonly used in DC electrical resistivity methods. The SI unit of resistivity (ρ), is ohm-m (Ω.m). In electrical resistivity, for a homogeneous and isotropic half-space, the measured relationship between current and potential difference for a particular electrode spacing is referred to as apparent resistivity.

The electrical conductivity (resistivity) of materials varies by several orders of magnitude. Most rock-forming minerals are insulators, and an electric current is carried by the passage of ions in pore water. Thus, most rocks conduct electricity by electrolytic

conduction of ions that take places through the moistures filled the pores media. The resistivity of a material depends upon rock type, porosity, connectivity of pores, nature of the fluid, and metallic content.

Electrical and electromagnetic methods can provide an effective mechanism to map the salinity of the subsurface formation by measuring the electrical conductivity. The bulk conductivity of rock is mainly caused by the electrolytic conduction in the pore fluids and depends on several parameters such as porosity, clay content, degree of saturation, and cementation. The pore fluid conductivity σ_{GW}, and the bulk conductivity of the rock σ_{rock} are related by:

$$\sigma_{GW} = F\sigma_{rock} \tag{1.1}$$

where F is the formation factor. The formation factor can be determined by coincident measurements of groundwater and formation conductivity or from empirical relationships such as Archie's Law (Archie 1942). The estimated formation factor can be used to infer the electrical conductivity of the pore fluids. Then, the salinity of the subsurface formation can be calculated using the general equation given by Wagner et al. (2006).

1.3.2. Electrical Resistivity

Electrical Resistivity provides a rapid and noninvasive set of techniques for monitoring groundwater. It is a powerful tool to characterize the spatial and temporal variability of subsurface formations. In this method, a current is injected across a pair of electrodes. Then, the voltage difference between the potential electrodes is measured. The voltage difference is a function of the current injected and the resistivity beneath the

electrode array. For a 3-D, isotropic distribution electrical resistivity $\rho(x, y, z)$, electrical potential $V(x, y, z)$ due to the current electrode (I) is defined as

$$\boldsymbol{\nabla} \cdot \left(\frac{\mathbf{1}}{\rho}\boldsymbol{\nabla}\mathbf{V}\right) = \text{-I } \delta(\text{x}) \tag{1.2}$$

(Binley 2015; Sharma and Verma 2015).

In the electrical resistivity method, commonly used electrode configurations include the Wenner, Schlumberger, and Dipole-Dipole arrays (Figure 1.2). In the Wenner array, the electrode spacing (a) are all equal, and the apparent resistivity can be expressed as:

$$\rho_a = \frac{\mathbf{2}\,\pi a \Delta V}{I} \tag{1.3}$$

In Schlumberger array, the potential electrodes (M and N) spacing is much smaller than the current electrodes (MN<0.2* AB) (Binley 2015). The apparent resistivity can be expressed as:

$$\rho_a = \frac{\pi(s^2 - a^2)\Delta V}{I} \tag{1.4}$$

In Dipole-Dipole arrays, the dipoles are equal in width (a) and separated by a distance n*a, where n is an integer multiplier. The apparent resistivity can be expressed as:

$$\rho_a = \pi n(n+1)(n+2)a\frac{\Delta V}{I} \tag{1.5}$$

The fundamental relationship between electrical potential and resistivity of stratified earth is given by:

$$V(r) = \frac{I\rho_1}{2\pi r}\left(1 + 2r\int_0^\infty K(\lambda)\,.J_0(\lambda r).\,\mathrm{d}\lambda\right) \tag{1.6}$$

where K is the Kernel function, controlled by the resistivities ρ_i $(i = 1,2,3 \ldots n)$ and thickness of the layers h_i $(i = 1,2,3 \ldots n-1)$ and J_0 is the zero-order of the 1st kind Bessel

function. For the 1-D case of flat homogeneous layers, computation of electrical potential and resistivity can be achieved using recurrence formulas and linear filtering techniques (Koefoed 1979; Anderson 1979).

Vertical electrical sounding (VES) is a 1-D resistivity method using measurements are made at the surface by systematically varying the electrode spacing. When the electrode spacing increases, the depth of penetration increases, and we capture in-depth information of the subsurface. Electrical resistivity tomography (ERT) provides a 2-D and 3-D resistivity method for imaging sub-surface formations using electrical resistivity measurements made at the surface. In electrical resistivity, a 1-D, 2-D, or 3-D images can be produced by combining a vertical sounding and /or surface profiling. Computation for 2-D and 3-D models are typically performed with finite difference or finite element techniques (Sharma and Verma 2015).

In my current research project, an electrical resistivity method such as a floating Dipole-Dipole configuration array and electrical resistivity tomography (ERT) were used. In ENP, the floating array was designed to gain better information about the lake sub-bottom conductivity and inverted to 1-D sounding models. In BPK, we used ERT to produce a 2-D subsurface image along the profile lines and VES data to calibrate EM measurements.

1.3.3. Electromagnetism (EM)

Electromagnetism uses the principles of electromagnetic induction to map variations in electrical conductivity. EM waves from a transmitting coil induce eddy currents in the subsurface, which resulting in a secondary magnetic field detected in a

receiver coil. The EM data are modeled to infer the electrical conductivity of the subsurface. Electromagnetic methods measure the response of the subsurface formation that results from the propagation of an electromagnetic wave (Oristaglio, and Hohmann 1984). The waves propagation is governed by the damped wave equation

$$\nabla^2\vec{B} - \mu_0\sigma\frac{\partial\vec{B}}{\partial t} - \mu_0\epsilon\frac{\partial^2 B}{\partial t^2} = \mu_0\nabla\times\vec{J} \tag{1.7}$$

where $\vec{B}$ is magnetic induction, μ_0 is magnetic permeability in free space ($4\pi \times 10\text{^}(-7)\ H/m$),$\sigma$ is electrical conductivity, ϵ is dielectric permittivity and $\vec{J}$ is the current density. FDEM methods applied at a frequency range of (100 Hz – 200 KHz) and the propagation term $\mu_0\epsilon\frac{\partial^2 B}{\partial t^2}$ (equation 1.7) is small in this frequency range (Everett and Chave 2019). As a result of this, the propagation term is neglected and the damped wave equation reduced to the quasi-static formulation of EM induction

$$\nabla^2\vec{B} - \mu_0\sigma\frac{\partial\vec{B}}{\partial t} = \mu_0\nabla\times\vec{J} \tag{1.8}$$

Frequency domain electromagnetic (FDEM) methods use two coils that transmit and receive primary and secondary magnetic fields. The two commonly used transmitter-receiver geometries are horizontal coplanar loop (HCP) and vertical coplanar loop (VCP) (Figure 1.3). In FDEM methods, the data of interest are in the in-phase (real), and out-of-phase (imaginary) components. The measured quantity is usually the ratio of the secondary magnetic field (H_s) to the primary magnetic field (H_p). The ratio of secondary to the primary field of a vertical dipole (horizontal coils) homogenous half-space is expressed as:

$$\frac{H_s}{H_p} = \frac{2}{\gamma^2 s^2}[9 - (9 + 9\gamma s + 4\gamma^2 s^2 + \gamma^3 s^3)e^{-\gamma s}] \tag{1.9}$$

where $\gamma = \sqrt{i\omega\mu_0\sigma}$ is a complex wave number and s is coil spacing (m) (Keller and Frischnecht 1982; McNeill 1980). The ratio of the secondary to the primary magnetic field (H_s/H_p) is a complex function that depends on inter-coil spacing (s), frequency (f), and conductivity (σ). The relationship can be simplified and linearly proportional to conductivity over a homogeneous subsurface under the low induction number approximation (LIN). The induction number (D) is the ratio of the coil spacing (s) to skin depth(δ) $= 1/\sqrt{\pi\mu_0\sigma f}$. The LIN approximation is valid when the conductivities are sufficiently low that the operational constraints of the induction number (D<<1) are respected. McNeill (1980) recommends the LIN approximation should be used where σ ≤ 100 mS/m. Under these conditions, the apparent conductivity is proportional to the quadrature component of the ratio of the magnetic field. Thus, the apparent conductivity under the low induction number (D) approximation is

$$\sigma_a = \frac{4}{\mu_0\omega s^2}\left(\frac{H_s}{H_p}\right) \tag{1.10}$$

and the contribution of each layer can be modeled independently as a linear combination of the response of each layer (Figure 1.4). For example, for a three-layer model

$$\sigma_a = \sigma_1[1 - R(z_1)] + \sigma_2\,[R(z_1) - R(z_2)] + \sigma_3 R(z_2) \tag{1.11}$$

where σ_n the conductivity of the nth layer, R is the cumulative response, and z is the ratio of depth to coil spacing of the layers (Mc Neill, 1980). The cumulative response function for a vertical dipole $R_v(z)$ is give by:

$$R(z) = 1/\sqrt{4z^2 + 1} \tag{1.12}$$

For a multiple layered half-space, the mutual coupling ratio varies with the arrangement of the loops. The coupling ratio (Z) for a pair of vertical dipoles (horizontal coplanar loops)

above a multi-layer over an infinite half-space was derived by (Wait 1958; Keller and Frischknecht 1966):

$$Z = 1 + B^3 T_0 \tag{1.13}$$

where B is the ratio of the coil spacing (s) to skin depth $(\delta) = 1/\sqrt{\pi \mu_0 \sigma f}$. The complex value function T_0 can be evaluated using the Hankel transform. The basic integral of the Hankel transform has an input of kernel function $R(\lambda)$ of an integer n order is given as:

$$T_0 = \int_0^\infty R(\lambda)\, \lambda^2\, e^{-\lambda A} J_0(\lambda B)\; d\lambda \quad , b > 0 \tag{1.14}$$

where J_0 is the zero-order Bessel function, λ is the radial wave number, A is the normalized height of the transmitter and receiver coil height, $R(\lambda)$ is the kernel function controlled by conductivities σ_i $(i = 1,2,3 \ldots n)$ and thickness of the layers h_i $(i = 1,2,3 \ldots n-1)$. The kernel function can be obtained by the recursion relationship (Koefoed 1979; Verma 1977; Fitterman 2015).

1.4. Inverse Model

The electrical properties of a rock can be measured using electrical and EM measurements using the governing equations mentioned above. The electrical conductivity and resistance measurement can be modeled using the inverse model. Thus, the inverse model helps to recover information about the subsurface physical properties (Figure 1.5). Inversion is a mathematical process for determining a model that produces the best fit between the observed data (d) and the model response (m). The forward operator (F) relates the agreement between the model and the data (Figure 1.5). In inverse modeling, an infinite number of models can fit the data with a certain level of uncertainty. The non-

uniqueness of the inverse problem and the uncertainty of the data error can lead to an extremely ill-posed solution. Thus, in the inversion process, a unique solution can be obtained by using additional constraints to the data and the model (Binley and Kemna, 2005; Fitterman 2015), which can be done as a regularized optimization problem. In regularized optimization, the objective function of the form

$$\phi(m) = \phi_d + \beta\phi_m \tag{1.15}$$

is sought to be minimized. The data objective function (ϕ_d) attempts to honor the data and the aim of the model function (ϕ_m) is to put constraints on the model (Fitterman 2015). The regularization parameter (β) sets a balance between the effects of the data and model objective functions (Farquharson et al. 2014).

Different regularization optimization techniques have been developed and used by different authors, such as Occam's inversion (Constable et al. 1984), layered and laterally constrained (Auken et al. 2004), versatile inversion (Oldenburg and Jones 2011b), ridge regression (Stoyer 2008; Inman 1975) and so on. For example, Occam's inversion solution fits the measurement with the smoothest possible model, and the inverted models generally do not show sharp changes (Constable et al. 1984). The Occam's inversion trades off the roughness of the model improvement and the least-squares error predicted from the linearized forward problem. Whereas, the ridge regression, trades off the size of the model improvement (Stoyer 2008; Inman 1975). In the ridge regression, for each iteration, a model correction is calculated using the best damping factor available for that iteration (Stoyer 2008).

Equivalency analysis shows the possible range of models that can fit the data. The results obtained from the inverse model needs careful interpretation. The common

phenomenon is a different combination of resistivity and thicknesses of the subsurface layer can produce the same or similar result known as a principle of equivalence Koefoed (1969). Furthermore, the suppression principle suggests a thin layer with resistivity values sandwiched between two conducting beds would produce no effect on the resistivity curves if the products of their thicknesses and resistivities are the same (Kunetz 1966; Sanuade et al. 2019). Therefore, to reduce this such ambiguity, it is recommended to integrate resistivity data with other geological or geophysical methods. In addition, the integration of electrical resistivity data with electromagnetic data is advisable.

1.5. Research Questions and Objectives of this Study

Geophysical methods have been used and applied to solve hydrogeological problems. In different environmental settings (water or land), the choice of Electromagnetic (EM) modeling approach depends on the type of instrument used and geological setting. Similarly, in the electrical resistivity method, it depends on electrical array configuration and geological setting. My project aims to answer the research questions:

I. Can geophysical techniques accurately and efficiently characterize groundwater salinity in the southern Mangrove Lake region of ENP?

II. Does the groundwater conductivity (salinity) in the Mangrove Lakes of ENP show a spatial and temporal variation with regard to climate and CERP initiatives?

III. How did Hurricane Irma storm surge impact the freshwater lens availability in BPK?

We used a floating Dipole-Dipole electrical resistivity array, electrical resistivity tomography (ERT), frequency domain electromagnetism method (FDEM), surface water, and groundwater sample to address the research questions mentioned above. Besides, different inversion scenarios, namely (1) free model, (2) constrained water depth, (3) constrained water column resistivity, and (4) constrained water depth and resistivity model, were compared to select an efficient inversion method. Then, the best model was used to characterize the conductivity of the subsurface formation.

The specific objective of the research can be summarized and organized as follows:

1. To assess and document the impact of Hurricane Irma storm surge and recovery history of the freshwater lens in BPK.
2. To improve the EM calibration approach and assess the spatiotemporal change of the freshwater lens in response to Hurricane Irma in BPK.
3. To compare DC resistivity and EM models and assess the effect of constraining layer parameters (resistivity and Depth)
4. To assess the spatial and temporal changes in the groundwater chemistry and estimate a formation factor in the Southern Mangrove Lakes of ENP.

1.6. Dissertation Organization

This dissertation work is organized into four chapters in a manuscript format. At the end of each chapter, references, tables, and figures are listed. The supplementary material of all the chapters is also listed in the appendix at the end of the dissertation. A summarized highlight of each chapter is presented below.

Chapter 2 covers the geophysical imaging of the impact of Hurricane Irma storm surge and the recovery history of the freshwater lens in BPK using electrical resistivity tomography and well data. I compared ERT images along three profiles ranging between 220 and 280 m length collected in 2011 with post-storm data collected about three to four months (November 2017/January 2018), eight months (May 2018), and fifteen months (December 2018) after Hurricane Irma. The post-storm data documented that the storm surge impacted the freshwater lens with high salinity zones in the upper 2 m of the groundwater. The increase in salinity was most pronounced in the lower elevations of the profiles. The ERT and well data collected 8 and 15 months after Hurricane Irma showed the freshwater lens recovered 40 % and 70 % of the pre-storm condition, respectively. The results suggested that both the impact of storm surge and the freshwater recovery associated with precipitation are most pronounced in low elevation regions where both saline and freshwater can collect at the surface. My study could be a prototype estimation for the low coralline limestone oceanic islands.

Chapter 3 focuses on calibration electromagnetic induction (EMI) conductivities using vertical electrical sounding (VES) measurements, followed by the temporal and spatial variation in apparent conductivities of the subsurface formation and a comparison of low induction approximation and full solution inversion. We conducted a simultaneous EM survey and electrical resistivity tomography (ERT) survey four months (January 2018) and 15 months (December 2018) after Hurricane Irma in BPK, FL. During calibration, inverted VES data were used as input in the electromagnetic forward model to estimate the quadrature component. Then, the observed offset between the calculated and measured quadrature data was corrected using a multiple linear regression model. This multiple linear

regression method is a promising calibration approach, and we extended to a profile line of 2.2 Km long. The spatial and temporal variation of apparent conductivity change between January and December 2018 suggested the impact of the storm surge on the freshwater lens recovery history is influenced by topography. The low induction approximation and full solution inversion showed a consistent estimate of the interface at approximately 3 m on average throughout the profile line. On the basis of my study, we concluded VES at pilot locations can be used to calibrate and verify the accuracy of FDEM measurements.

Chapter 4 focused on geophysical inversion and compared 1-D constrained and unconstrained electrical resistivity and EM inversion methods. A floating Dipole-Dipole electrical resistivity array and EM surveys were conducted between June to August 2019 in the mangrove lakes of ENP to develop techniques for making repeatable measurements of the electrical conductivity (salinity) of the groundwater beneath the lakes. Chapter 4 aims to select an efficient inversion method and estimate a formation factor for the mangrove lake regions of ENP. The resistivity data were inverted to a two and three-layers model and compared four different inversion scenarios, namely free model, constrained water depth, constrained water column resistivity, and constrained water depth and resistivity model. In the free model, both the surface water resistivity and depth were allowed to be free in the inversion. Whereas, for the constrained models, the water layer thickness and resistivity were fixed using the measured data using a calibrated rod and a YSI Probe. We evaluated the inverted data using RMS error, the goodness of fit, and percent error. We concluded the constrained water depth model is an effective inversion approach in the mangrove lakes.

Chapter 5 investigated the spatial and temporal changes in the groundwater chemistry in the Mangrove Lakes of ENP using electrical resistivity and EM methods. The geophysical survey was conducted from 2016 to 2019 in the Mangrove Lakes of ENP. In 2016, in the McCormick Creek system (Seven Palm), the apparent conductivities (salinity) during the dry season demonstrated a general increase in salinity from north to south and reflected a decreased precipitation, southward flow, and the influence of saline water from Florida Bay. Between 2016 to 2017, the apparent conductivities showed a considerable decrease in both the McCormick Creek and the Alligator Creek systems (West Lake). The apparent conductivity change suggests a freshening of the groundwater. In 2019, the groundwater salinity decreased from west to east and from north to south and may reflect the effects of increased flow that result from restoration efforts. In my study, I estimated a formation factor of 10.7 with a standard deviation of 1.8 for the mangrove lake regions of ENP. The formation factor was used to produce a regional map of groundwater salinity. This study showed the floating electrical resistivity array and EM methods can effectively characterize the lake bottom conductivity (salinity) and be used regularly in monitoring the surface water and groundwater salinity.

1.7. References

Anderson, Walter L. 1979. Numerical Integration of Related Hankel Transforms of Orders 0 and 1 by Adaptive Digital Filtering. *Geophysics* 44 (7): 1287-1305.

Archie, G. E. (1942). The electrical resistivity log as an aid in determining some reservoir characteristics. *Transactions of the AIME*, 146(01), 54-62.

Auken, E., and Christiansen, A. V., 2004, Layered and laterally constrained 2D inversion of resistivity data: Geophysics, 69, 752–761. doi:10.1190/1.1759461

Binley, A. 2015. Tools and techniques: electrical methods. G. Schubert (Ed.) (2nd ed.), *Treatise on Geophysics*, 11, Elsevier, Oxford, UK (2015), pp. 233-259. https://doi.org/10.1016-B978-0-444-53802-4.00192-5

Binley, A., and Kemna, A. (2005). DC Resistivity and Induced Polarization Methods, In *Hydrogeophysics*, Springer, 522 pp. 129–156.

Constable, S. C., Parker, R. L., and Constable, C. G. (1987). Occam's inversion: A practical algorithm for generating smooth models from electromagnetic sounding data. *Geophysics*, *52*(3), 289-300.

Cunningham, K. J., Bukry, D., Sato, T., Barron, J. a, Guertin, L. a, Reese, R. S., and Anonymous. (2001). Sequence stratigraphy of a South Florida carbonate ramp and bounding siliciclastics (late Miocene-Pliocene); Geology and hydrology of Lee County, Florida. *Durward H. Boggess Memorial Symposium on Geology and Hydrology of Lee County*, Florida, Fort Myers, FL, United States, Nov. 18-19, 1999, (49), 35.

Day-Lewis, F.D., White, E.A., Johnson, C.D., and Lane Jr., J.W., (2006). Continuous resistivity profiling to delineate submarine groundwater discharge—examples and limitations. *The Leading Edge* 25 (6), 724–728.

Everett, M. E., and Chave, A. D. (2019). On the physical principles underlying electromagnetic induction. *Geophysics*, *84*(5), W21-W32.

Farquharson, C. G., and Oldenburg, D. W. (2004). A comparison of automatic techniques for estimating the regularization parameter in non-linear inverse problems. *Geophysical Journal International*, *156*(3), 411-425.

Fish, J. E., and Stewart, M. T. (1991). Hydrogeology of the surficial aquifer system, Dade County, Florida, *U.S. Geological Survey* Water-Resources Investigation Report 90-4108.

Igor, S. (1993). World fresh water resources. *Water in crisis: a guide to the world's. Oxford University Press, Inc, Oxford*.

Inman, Joseph Robert. 1975. Resistivity Inversion With Ridge Regression. *Geophysics* 40 (5): 798.

Keller, George Vernon, and Frank C. Frischknecht. 1966. Electrical Methods in Geophysical Prospecting. Oxford, Pergamon Press, 527 p.

Koefoed, O. 1979. Resistivity Sounding on an Earth Model Containing Transition Layers with Linear Change of Resistivity with Depth. *Geophysical Prospecting* 27 (4): 862–68.

Kunetz, G. (1966). Principles of direct current-Resistivity prospecting. Gebriider Bomtraege Gebrüder Borntraege, Berlin, pp.103 +xvi.

Loke, M.H., Chambers, J.E., Rucker, D.F., Kuras, O., and Wilkinson,P.B. (2013). Recent developments in the direct-current geoelectrical imaging method, *Journal of Applied Geophysics*. doi:10.1016/j.jappgeo.2013.02.017.

McLachlan, P. J., Chambers, J. E., Uhlemann, S. S., and Binley, A. (2017). Geophysical characterisation of the groundwater–surface water interface. *Advances in water resources* , *109*, 302-319.

McNeill, J. D. 1980. Electromagnetic Terrain Conductivity Measurement at Low Induction Numbers. http://www.geonics.com/pdfs/technicalnotes/tn6.pdf.

Miller, J. A. (1990). Ground Water Atlas of the United States Alabama, Florida, Georgia, and South Carolina HA 730-G. *U.S. Geological Survey*. : http://pubs.usgs.gov/ha/ha730 /ch_g/ G-text4.html HA 730-G.

NSIDC., (2020). Facts about glaciers | National Snow and Ice Data Center. Retrieved 16 June 2020, from https://nsidc.org/cryosphere/glaciers/quickfacts.html

Neal, A., Grasmueck, M., McNeill, D. F., Viggiano, D. A., and Eberli, G. P. (2008). Full-Resolution 3D Radar Stratigraphy of Complex Oolitic Sedimentary Architecture: Miami Limestone, Florida, U.S.A. *Journal of Sedimentary Research*, 78(9), 638–653.

NGWA. (2013). National Groundwater Association. Facts About Global Groundwater Usage. NGWA, Factsheet, 9/2013.

Oldenburg, D. W., and Jones, F. H. M., 2011b, EM1DFM (Inversion for Applied Geophysics): University of British Columbia Geophysical Inversion Facility. www.eos.ubc. ca/ubcgif/iag/

Oristaglio, M. L., and Hohmann, G. W. (1984). Diffusion of electromagnetic fields into a two-dimensional earth: A finite-difference approach. *Geophysics*, *49*(7), 870-894.

Prinos, Scott T., Michael A. Wacker, Kevin J. Cunningham, and David V. Fitterman. 2014. Origins and Delineation of Saltwater Intrusion in the Biscayne Aquifer and Changes in the Distribution of Saltwater in Miami-Dade County, Florida. US Geological Survey, no. 2014-5025. https://doi.org/10.3133/sir20145025.

Sanuade, O. A., Amosun, J. O., Oyeyemi, K. D., Olaojo, A. A., Fagbemigun, T. S., and Faloyo, J. I. (2019, August). Analysis of principles of equivalence and suppression in resistivity sounding technique. In *Journal of Physics: Conference Series* (Vol. 1299, No. 1, p. 012065). IOP Publishing.

Sharma, Shrey, and Gunjan Kumar Verma. 2015. Inversion of Electrical Resistivity Data : A Review. World Academy of Science, Engineering and Technology, International Journal of Environmental, Chemical, Ecological, Geological and Geophysical Engineering 9 (4): 392–98.

Stoyer, C. (2019). IX1D Resistivity, IP, EM Software (Version 3). Retrieved from http://www.interpex.com/ix1dv3/ix1dv3.htm

Tan, X., Mester, A., Zimmermann, E., and VAN DER KRUK, J. (2019). Calibration method for electromagnetic induction measurement systems, and apparatus. *U.S. Patent Application No. 16/310,463*.

UNESCO. (2012). The United Nations World Water Development Report 2: Water in a Changing World. *Global Hydrology and Water Resources,* Routledge. p.121

Wagner, RJ, Boulger, Jr., RW, Oblinger, CJ and Smith, B. (2006). Guidelines and standard procedures for continuous water-quality monitors: station operation, record computation, and data reporting. USGS Techniques and Methods, 1-D3, 96.

Wait, J. R. 1958. Induction by an Oscillating Magnetic Dipole over a Two-Layer Ground. Applied Scientific Research B-7: 73–80.

Yeboah-Forson, A., Comas, X., and Whitman, D. (2014). Integration of electrical resistivity imaging and ground penetrating radar to investigate solution features in the biscayne aquifer. Journal of hydrology, 515:129–138.

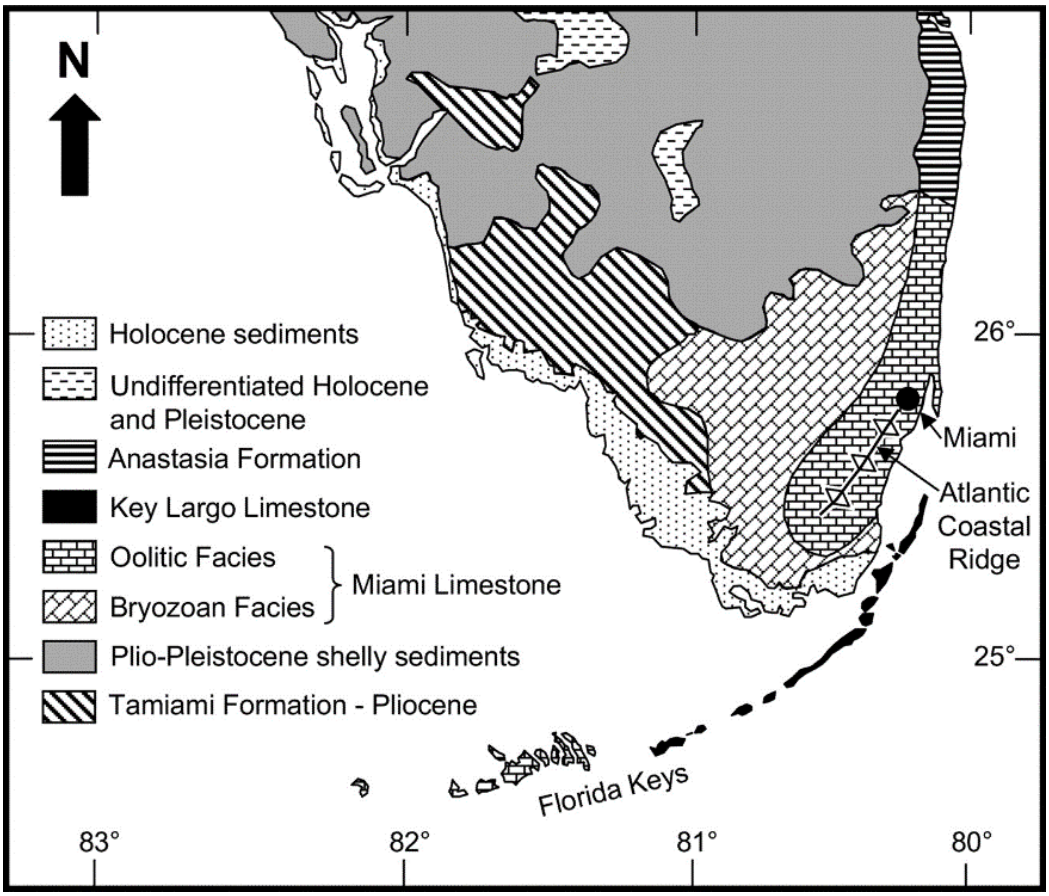

Figure 1.1: The geology of southeastern Florida and the Florida Keys with the subdivision of the Miami Limestone into bryozoan facies and Oolitic facies (Neal et al. 2008).

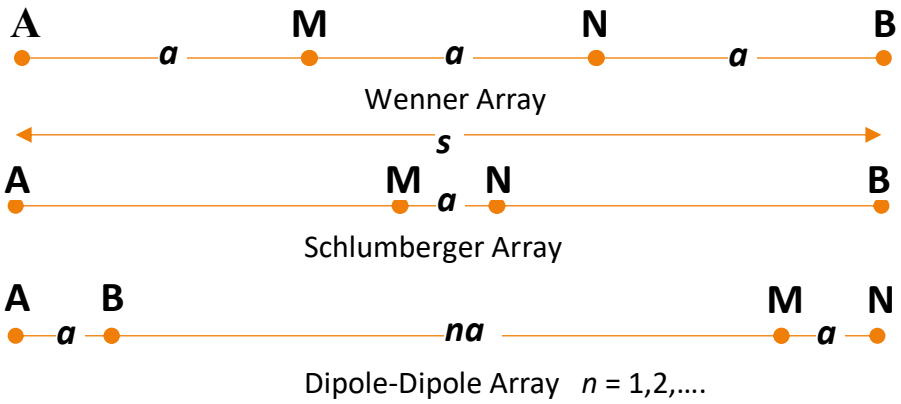

Figure 1.2: Common electrical Arrays. A and B are the current electrodes. M and N are the potential electrodes.

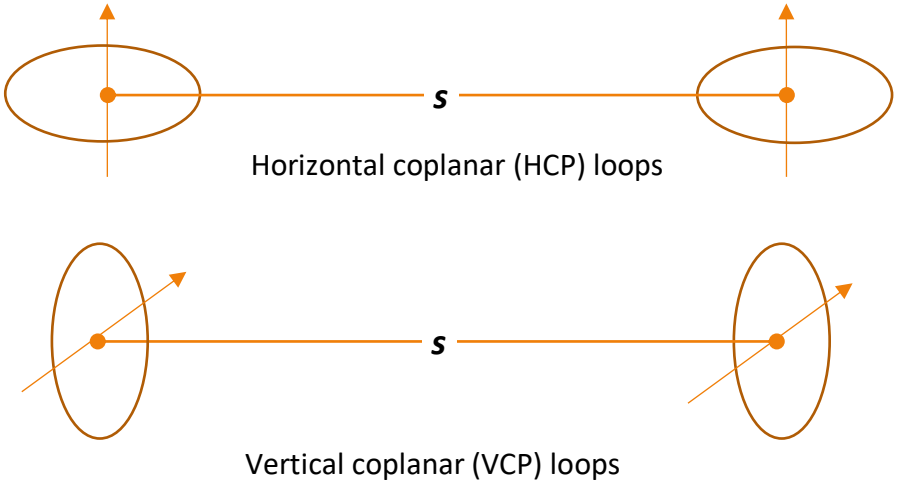

Figure 1.3: Common frequency domain EM geometry. s is the spacing between the transmitter and receiver geometries

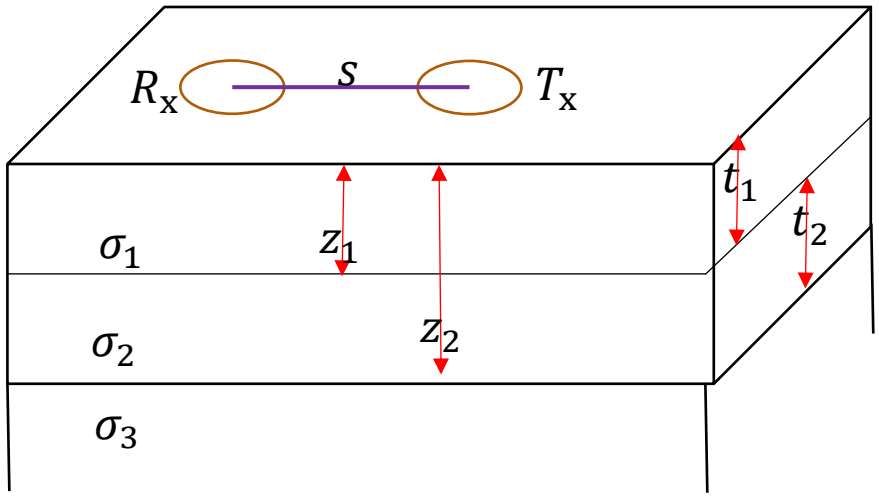

Figure 1.4: Three- Layer model with conductivities σ_n, depth Z_n and thickness t_n, where n is n is the nth layer (after Stewart

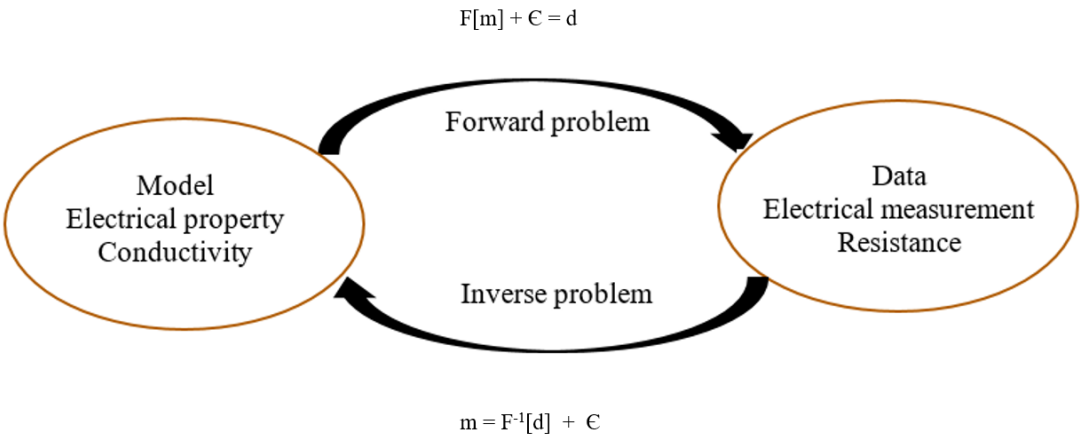

Figure 1.5: Electrical properties and measurement relationship using Inverse and Forward Problem (after Binley and Kemna 2005). The forward operator (F) relates the observed data (d) and model (m) with a certain level of uncertainty/ error (Є).

2. The Effect of Hurricane Irma Storm Surge on the Freshwater Lens in Big Pine Key, Florida using Electrical Resistivity Tomography[1]

Abstract

Animals and plants on low elevation oceanic islands often rely on a thin lens of fresh groundwater and this lens is vulnerable to seawater contamination from storm surge. Documentation of the impact of the storm surge on the freshwater lens and its subsequent recovery is limited. In September 2017, Hurricane Irma made landfall in the Florida Keys as a category 4 storm with storm surge heights in excess of 2 m. We used Electrical Resistivity Tomography (ERT) to investigate the effect of the storm surge on the freshwater lens of Big Pine Key, FL. The study compared ERT images along three profiles ranging between 220 and 280 m length collected in 2011 with post-storm data collected about three to four months (November 2017/January 2018), eight months (May 2018), and fifteen months (December 2018) after Irma. The post-storm data documented that the storm surge impacted the freshwater lens on all three profiles with low resistivity (i.e., high salinity) zones in the upper 2 m of the groundwater. The increase in salinity was most pronounced in the lower elevations of the profiles. The May 2018 (collected immediately after two weeks of intense precipitation) and December 2018 data showed 40 % and 70 % recovery of the freshwater lens, most pronounced in the lower elevation of the profiles. Both the impact of storm surge and the freshwater recovery associated with precipitation are most

[1] Portion of this chapter were published in Kiflai et al.(2019). Kiflai, M.E., Whitman, D., Ogurcak, D.E. et al. The Effect of Hurricane Irma Storm Surge on the Freshwater Lens in Big Pine Key, Florida using Electrical Resistivity Tomography. Estuaries and Coasts 43, 1032–1044 (2020). https://doi.org/10.1007/s12237-019-00666-3

pronounced in low elevation regions where both saline and freshwater can collect at the surface. This could be a prototype example for low limestone (Type III) oceanic islands.

2.1. Introduction

Oceanic islands often contain a freshwater lens that floats on top of the higher density seawater (Figure 2.1; Falkland and Custodio 1991). The freshwater lenses are often the sole sources of water for the inhabitants. Because of their proximity to the ocean, these freshwater aquifers are vulnerable to saltwater intrusion (Morgan and Werner. 2013) and storm surge. In many parts of the world subject to impacts from tropical cyclones, storm surge impacts can be substantial. Moreover, impacts of global climate change, including accelerating sea-level rise (Church and White 2006) and predicted increases in the frequency of strong hurricanes (Bender et al. 2010), will increase vulnerability to hurricane storm surge (Chang et al. 2011; Ross et al. 2009). Storm surge, which is produced by the force of onshore winds, can flood low-lying coastal areas with saline water (Huizer et al. 2017). The impact of the storm surge on the freshwater lens is shown schematically in Figure 2.1. In addition, these events can exacerbate the long term effects of sea-level rise on the freshwater lens (Halley et al. 1997). Moreover, climatic variables such as reduced precipitation and high evapotranspiration affect the recharge rate of the freshwater lens (Ranjan et al. 2006) that can affect the freshwater lens recovery rate.

On September 10, 2017, Hurricane Irma made landfall in the Florida Keys as a category 4 storm. In the Florida Keys, the landfall wind speed was estimated at 59 m/s (115 kt) with a minimum pressure of 931 mb (Cangialosi et al. 2018). Storm surge heights in the Lower Keys were in excess of 2 m (Cangialosi et al. 2018; Xian et al. 2018). The islands

in the Lower Keys generally have a maximum elevation of 3 m making the freshwater lens on these islands especially vulnerable to salinization from storm surge events.

Prior to Hurricane Irma, two storm surge events have impacted the Florida Keys over the past 20 years. On September 25, 1998, Hurricane Georges made landfall at category 2 strength and produced a storm surge of 1.5 to 1.8 m in the Lower Keys (Pasch et al. 2001). The impact of storm surge in the Lower Keys caused salinity in the groundwater to increase more than 15 PSU[2] for several months (Lopez et al. 2003). Seven years later, Hurricane Wilma made landfall on October 24, 2005, at category 1 with a storm surge of 1.8 to 2.7 m on the Lower Keys (Pasch et al. 2006). The impact of the storm surge followed by the dry season led to high mortality of pine trees in the pine forests of Big Pine Key (BPK) and Sugarloaf Key (Ross et al. 2019).

In the Florida Keys, hurricane events frequently occur with a mean return period of 5 years (Keim et al. 2018), but our understanding of the impact of storm surge on the freshwater lens is limited. Hence, it is of interest to evaluate and monitor how long the freshwater lens stays salinized. On BPK, precipitation is the primary source of freshwater recharge for the groundwater. Accordingly, a coupled effect of the decline in the amount of precipitation and high evapotranspiration may retard the freshwater lens recovery rate. On BPK, several federally listed animal and plant species are dependent on freshwater availability (Ross et al. 2009). Hence, a rapid assessment of the freshwater lens is an integral part of evaluating the impact of hurricanes on the freshwater resource necessary for the survival of plant and animal species.

[2] The salinity increase was reported in ppt (Lopez et al. 2003)

The impact of storm surge on coastal aquifers and oceanic islands depends on the coastal topography, the mean sea level, the dynamics of the weather system, and the direction of the storm track (Yang et al. 2015). The recovery of the freshwater lens is a function of the recharge rate, vadose zone thickness, hydraulic conductivity, and geological heterogeneity of the aquifer (Holding and Allen 2015). Many studies have addressed the impact of storm surge and recovery of freshwater on the main coastal aquifers and oceanic islands using numerical modeling (Huizer et al. 2017; Holding and Allen 2015; Yang et al. 2015; Chui and Terry 2012). However, few studies focused on using in-situ measurements (Terry and Falkland 2010; Van Biersel et al. 2007). Estimates of freshwater lens recovery durations using numerical modeling range from 1 to 20 years in different hydrogeological settings (Holding and Allen 2015; Yang et al. 2015). Studies on Pukapuka Atoll in the Northern Cook Islands (South Pacific Ocean; Terry et al. 2010) and the Lake Pontchartrain coastal aquifers of Louisiana, USA (Van Biersel et al. 2007), using in-situ measurements showed recovery durations of almost one year. However, the freshwater lens may take more than a year to recover if the surge event is followed by a dry period (Bailey et al. 2009; Chui and Terry 2012). In general, the recovery rate in oceanic islands and coastal aquifers depends on a combination of climatic and geological factors.

According to Robins and Lawrence (2000), oceanic islands are classified into six categories on the basis of geology, climate, freshwater lens morphology, and water balance. Big Pine Key is part of the low coralline limestone (Type III) found in many Caribbean and Pacific Bermuda islands. Therefore, the current research is conducted in an effort to understand the impact and recovery rate of the low coralline limestone (Type III) oceanic islands.

In our study, we use Electrical Resistivity Tomography (ERT), a geophysical technique for imaging sub-surface formations using electrical current measurements made at the surface, to measure electrical resistivity (Binley and Kemna 2005; Huizer et al. 2017). Current is injected between two electrodes while the voltage is simultaneously measured between two other electrodes. Then, from Ohm's law, the apparent resistivity of the subsurface formation can be calculated. In general, as the electrode spacing increases, progressively greater depths are imaged. Modern multi-electrode systems allow rapid resistivity measurements at a variety of electrode spacings and locations. These measurements are then inverted to produce an image of the subsurface resistivity distribution beneath a profile. The resistivity models are converted to pore fluid resistivity by applying an electrical formation factor and finally converted to salinity models for each time period.

Because resistivity is often dependent on formation porosity and pore fluid salinity, ERT is a powerful tool to characterize spatial and temporal changes in aquifers (Binley and Kemna 2005). Electrical Resistivity Tomography methods have been widely used in monitoring the dynamics of salt water intrusion (De Franco et al. 2009; Goebel et al. 2017), tidal disturbance (Tucker 2013; Ogurcak 2015; Huizer et al. 2017), and subsurface contamination (Kemna et al. 2002; Simyrdanis et al. 2018; Caterina et al. 2017; Rosales et al. 2012). Huizer et al. (2017) investigated the impact of tides and storm surges on coastal groundwater on the Dutch Coast and simulated the salinity change in the coastal aquifer. Other studies conducted by Kemna et al. (2002) assessed the usefulness of ERT in imaging and characterizing solute transport in heterogeneous aquifers.

In the current study, we investigate the effect of the Hurricane Irma storm surge on the freshwater lens of Big Pine Key, FL, the largest island in the Lower Keys, using ERT measurements on three profile lines that span coastal to upland habitat gradients. We compare ERT imaging results of baseline data collected 6 years before Irma (November 2011) with data collected about 3, 4, 8, and 15 months (November 2017; January 2018; May 2018; and December 2018) after Irma. In addition, we compared average Well data recorded 6 years and 6 months before Irma (May 2011- April 2012; March 2017) and 2 weeks, 3, 8, and 15 months (September 2017; November 2018; May 2018 and December 2018) after Irma. Particular attention is given to the initial impact of the storm surge and the subsequent recovery of the freshwater lens.

2.2. Geological Setting

The Florida Keys are an island chain that stretches for 240 km along the southern end of the Florida peninsula (Figure 2.2). The Keys are divided into the Upper Keys extending from Soldier Key to Vaca Key and the Lower Keys extending from BPK to Key West. Big Pine Key is the largest island in the Lower Keys with an average length of about 10 km and a width of 3 km (Figure 2.2). The northern half is occupied by the Key Deer National Wildlife Refuge and the southern part is suburban residential. Potable water for domestic and commercial use is not obtained from the freshwater lens, but rather is transported to the Keys via aqueduct. The freshwater lenses are the sole sources of water for the animal and plant species in BPK. The lower Florida Keys have diverse species communities such as pine Rocklands, hardwood hammocks, and supratidal scrub. Pine Rocklands are found at the interior of the islands at higher elevation followed by the

hardwood hammocks. Near the shoreline, the supratidal scrub and mangrove forest are the dominant species communities (Ross et al. 1992).

The Lower Keys have a humid subtropical climate with a wet season from June to October and a dry season from November to May. The mean annual precipitation is 102.2 cm. The cumulative precipitation recorded at BPK between January 2011 to December 2018, showed large precipitation events in October 2011, September 2017 and May 2018 (Figure 2.3). The variation between steep (wet season) and gentle (dry season) slopes of the cumulative precipitation reflect these seasonal changes. The minimum and the maximum monthly temperature are 20^{o} C and 29^{o} C in January and August (NOAA NCDC 2018).

The geology of the BPK consists of the Miami formation and the Key Largo Limestone. The Miami formation (limestone) occurs in the southern part of Florida and the southernmost Keys. This limestone was formed in the Pleistocene (Fish and Stewart 1991). The Miami formation consists of oolitic and bryozoan facies (Neal et al. 2008) but in the Lower Keys, the oolitic facies predominates. The oolite facies is composed of white to gray, poorly to moderately consolidated sand and ooids, while the bryozoan facies consists of fossiliferous limestone. The Key Largo Limestone occurs in the lower and upper keys. It is composed of white to light gray, moderately to well indurated, very porous, coralline limestone (Scott 2001). The Key Largo Limestone underlies the Miami Formation in BPK and there is sharp contact between the two units on the southeastern part of BPK. In BPK, the upper hydrostratigraphic unit, Miami Formation, has a hydraulic conductivity of 100-140 m/day. The lower unit Key Largo Limestone has a hydraulic conductivity of 1200-1600 m/day (Langevin et al. 1998).

Hanson (1980) mapped the freshwater lens boundary on BPK from the contour line of 500 mg/L of chloride concentration observed from shallow wells of 1.5m depth. In that study, the mapped freshwater lens boundary was considerably wider on the north and tapered toward the south. In addition, the size of the freshwater lens varied in response to seasonal recharge. Stewart (1988) investigated the freshwater-saltwater interface with Electromagnetic (EM) methods and estimated its depth ranging from 4 to 8 m along the profile lines. The author suggested the permeable Key Largo Limestone unit truncates the low part of the freshwater lens. Similarly, Wightman (1990) delineated the lateral extent of the freshwater lens in BPK using EM methods (Figure 2.2). The author concluded the freshwater lens expands and contracts laterally as a result of seasonal recharge but showed limited vertical movement. A study conducted by Tucker (2013) using ERT and groundwater modeling suggests tidal fluctuations can affect the freshwater lens near the shoreline, but the effect is limited inland. A study conducted in 2011 - 2012 by Ogurcak (2015) investigated the relationship of precipitation, evapotranspiration, and changes in groundwater salinity using ERT survey and groundwater samples. The author concluded that change in groundwater salinity was an important variable in the classification of forest dynamics.

2.3. Method

2.3.1. Experimental Setup

Electrical Resistivity Tomography surveys were conducted on three profile lines. Profiles B1 and B2 cross the freshwater lens boundary defined by Wightman (1990), whereas B3 is outside the freshwater lens (Figure 2). The ERT data were collected using a

28 electrode, Advanced Geosciences Inc (AGI) Super Sting R1 IP resistivity imaging system. Stainless steel electrodes were placed at 2 m spacing in a Wenner array configuration that resulted in current electrode spacings ranging from 6 to 54 m. Electrodes were wetted with a saltwater solution to minimize contact resistance. For such spacings, the maximum depth of imaging is generally less than 10 m. Each 28-electrode array was rolled along each line to produce profiles ranging in length from 222 m to 278 m.

A series of shallow (~1 m deep) monitoring wells were installed along the ERT profiles in 2010. Depth to the water table, temperature, specific conductivity (the reciprocal of resistivity), and salinity were measured with a YSI probe at each of these wells at monthly intervals between May 2011 and April 2012 (Ogurcak 2015; Ogurcak and Price 2018). These wells were resampled in March 2017 (6 months before Irma), September 27, 2017 (17 days post-Irma), and during the ERT data collection in November 2017, May 2018 and December 2018. In general, the elevation of the water table at these wells varied little both spatially and temporally, ranging between -0.2 to 0.2 m NAVD88.

The pre-Irma ERT data used as a baseline for this study were collected in November 2011 (Tucker 2013; Ogurcak 2015). Previous work documented the seasonal ERT changes between the dry (May 2011) and wet (November 2011) seasons. The authors found that the freshwater and saltwater interface moved downward vertically at most by 1 m. However, no appreciable lateral expansion of the freshwater lens was observed. During this time, a heavy non-tropical precipitation event was recorded in October 2011 (Figure 2.3), and the freshwater recharge associated with heavy precipitation is reflected in the November 2011 measurements. Between November 2011 and September 2017, the cumulative precipitation data show only the normal variations between wet and dry seasons

(Figure 2.3). Most importantly, there was no storm surge event in the Florida Keys that could potentially deposit saline water on top of the freshwater lens (Ross et al. 2019). Hence, the ERT data collected on November 2011 is an effective baseline to compare the pre and post-Hurricane Irma changes.

Post-storm data were collected during November 29-30, 2017 (80 days post-Irma). As a consequence of instrument failure, the November data for profile B1 was unusable, and data for this profile were reacquired on January 04, 2018. The ERT data were collected again during May 29-31, 2018. During the May 2018 survey, standing water from heavy rainfall prevented deployment on the entire B1 profile, and the ERT survey covered only the first 194 m. The electrode positions on the profiles were precisely located relative to the wells in November 2011, and these same electrode positions were used for the later surveys.

2.3.2. Data Analysis

The ERT data were inverted with an open-source R2 v3.3 inversion program (Binley 2019). Inversion of ERT data is nonunique such that an infinite number of models can fit the data with a certain level of uncertainty. The inverse solution in R2 is obtained by minimizing an objective function that combines a weighted least square and an Occam-type, regularized optimization (Constable et al. 1984). The Occam inversion solution fits the measurement with the smoothest possible model, and therefore, the inverted models generally do not show sharp changes.

The models were parameterized on a regular quadrilateral mesh with a horizontal node spacing of 0.50 m and a variable vertical node spacing of 0.2 m near the surface,

which increased by a factor of 1.1 to a maximum depth of 9.3 m. Patches of two adjacent horizontal nodes were lumped together that reduced the effective horizontal resolution to 1 m. Additional model nodes were included at the edges and beneath the model to avoid edge effects in the forward calculations. The modeling software R2 allows the inclusion of surface topography that was extracted from 1 m^2 spatial resolution LiDAR data along each profile. The 2011 data were inverted using a uniform starting model of 100 Ω-m, but for the Nov 2017/Jan 2018 data and the May and December 2018 data the ERT data were inverted using a difference inversion algorithm that inverts the difference between the before and after observations and utilizes the previous inversion results as a starting model (LaBrecque and Yang 2001; Tucker 2013). The difference inversion reduces noise from the inversion procedure and converges fast.

Depth of investigation (DOI) analysis was performed to quantify the depth below which the physical properties are not constrained by the data (Oldenburg and Li 1999). The DOI compares the inversion results calculated relative to different reference models and calculates an index from their normalized difference. The DOI index ranges between 0 and 1, where 0 indicates the model is well constrained by the data, and 1 indicates a poorly constrained model. Oldenburg and Li (1999) recommended a threshold DOI index of 0.1 or 0.2. In the current study, 50 and 10 Ω-m reference models were used to calculate the DOI index.

In nonconductive rocks, the bulk electrical resistivity is largely the result of electrolytic conduction in the pore fluids and depends on several parameters such as porosity, the degree of saturation, cementation, and pore fluid resistivity. Archie (1942)

proposed a relationship between the pore fluid resistivity, ρ_w, and the bulk resistivity of the fluid-saturated formation, ρ_b,

$$\rho_b = F\rho_w \quad (2.1)$$

where F is the formation factor. By assuming a formation factor, these measurements can be used to infer the electrical resistivity of the pore fluids. Tucker (2013) estimated a formation factor of 9.5 for BPK, using regression of the pore water resistivity collected in the shallow wells along the profiles and the bulk resistivity at coincident locations and depths on the ERT profiles. However, the estimated formation factor may only be appropriate for the upper 5 m of the section corresponding to the Miami formation and may not be appropriate to the underlying Key Largo Limestone. The estimated formation factor may limit the applicability of the results in the deeper parts of the section. Finally, the pore water resistivity was converted to salinity using the empirical equations given by (Wagner et al. 2006).

2.4. Results

2.4.1. Well Data

Profile B1 extended eastward from the western shoreline of the island. On profile B1, the salinity decreased from around 6 PSU in the most nearshore well to 1-2 PSU farther inland at all sampling dates (Figure 2.4a). The pre and post-Irma salinities were similar at all three wells, with the exception of the average 2011 and 2012 measurement at 36 m that was 1 PSU higher than the other measurements. The only post-storm increases in salinity were seen at the 105 m well (< 0.5 PSU increase).

Profile B2 was located in the interior of the island. Pre storm (average of 2011 and 2012) salinities were low (< 2.5 PSU) at all three wells along the profile (Figure 2.4b). Post-storm, the salinity in the well at 22 m along the profile did not change, but in the wells at 190 m and 278 m, the salinity increased by 6.5 and 22.5 PSU, respectively. These increases were observed at wells situated on low elevation positions of the profile (Figure 2.4b). In general, the salinity in the 190 m and 278 m wells decreased at the later sampling dates. For example, at the well located at 278 m, the salinity decreased from September 2017 to November 2017 by 16 PSU and from November 2017 to May 2018 by 4 PSU. Furthermore, the salinity decreased from May to December 2018 by 2.9 and 0.6 PSU.

Profile B3 extends southward from a low elevation supratidal zone into the higher elevation Pine Rockland. In general, the salinity decreased from north to south on all sampling dates, decreasing from 15-20 PSU in the north to 3 PSU in the south (Figure 2.4c). Post-storm (September 27, 2017), salinities in the wells situated at low elevation locations on the profile (18 and 62 m) increased by 1 and 2 PSU respectively. The wells located at 104 and 134 m exhibited eight PSU post storms increase. By May 2018, the salinity in these two wells decreased two PSU and continued to decrease by 3.4 and 2.4 PSU by December 2018. Salinities in the most distal well on the profile (192 m, Figure 2.4c) exhibited no change pre and post-storm surge.

2.4.2. ERT Profiles

Inversion results of the ERT profiles are presented in Figure 2.5 – 2.10. In general, a resistivity greater than 200 Ω·m corresponds to the unsaturated zone, between 200 and 50 Ω·m corresponds to freshwater saturated rock, between 50 and 15 Ω·m to poor -

intermediate quality freshwater, between 15 and 4.5 Ω·m to brackish water, and less than 4.5 Ω·m to saline groundwater (Zohdy et al. 1993; Nowroozi et al. 1999). To assist interpretation of the profiles, contours of 3 PSU and 10 PSU are used to illustrate the approximate boundaries of the fresh, brackish, and saline groundwater. The DOI index contour at 0.2 is shown as a dashed line to limit over interpretation of the deeper parts of the inverted profiles (Figure 2.5-2.10). Regions of the model below the DOI contour are not well constrained by the data.

I. ERT Profile B1

ERT profile B1 is situated near the western shoreline of the island and crosses the lateral boundary of the freshwater lens defined by Wightman (1990; Figure 2.2). In November 2011, the ERT image showed a gradual change of resistivity (and salinity) with a depth that represents the freshwater lens, brackish transition zone, and saltwater (Figure 2.5b). The freshwater lens is characterized by wedge-shaped region corresponding to resistivity values ranging from 30 to 170 Ω·m that thickens from ~2 m at 35 m on the profile to 5 m at the end of the profile. Below this zone, the resistivity gradually decreases to values of 4 Ω·m.

The January 2018 data show that in portions of the upper 2 m of the profile, the resistivity decreased to less than 10 Ω·m (Figure 2.5c). This decrease is most pronounced east of 135 m in the lower elevation section of the profile. In the center of the profile, the base of the freshwater lens, as indicated by the 3 PSU salinity contour, appears to be depressed downward by around 3 m (Figure 2.5c). In May 2018, the resistivity increased to greater than 10 Ω·m in the top 2 m of the section (Figure 2.5d). These increases were most pronounced between 35 - 85 and 135 - 190 m. In December 2018, in the top 2 m,

between 35 m to 222 m, the resistivity increased on average to 26 Ω·m in the top 2m (Figure 2.5e). The base of the freshwater lens indicated by the 3 PSU contour remained similar to that observed for the January 2018 data (Figure 2.5c).

The B1 ERT data indicate a general increase in salinity in the upper 2 m of the section between November 2011 and January 2018 (Figure 2.6b). In lower elevations of the profile, between 0 to 25 m and at distances greater than 130 m on the profile, the salinity increased by 2 to 10 PSU. The increase was largest east of 190 m. In the higher elevation section, between 25 and 130 m, the salinity increase was smaller, increasing at most by 4 PSU. Below 2 m depth, there was a minimal variation over time. Between January 2018 and May 2018, salinity in the upper 2 m of the section decreased by up to 4 PSU (Figure 2.6c). These decreases were greatest at distances less than 80 m and greater than 130 m. Small increases in salinity relative to November 2017 were observed at depths greater than 2 m. Between December 2018 (post-storm) to November 2011 (pre-storm), the salinity in the upper 2 m of the section increased by up to 4 PSU (Figure 2.6d). These changes were increased gradually from West to East of the Profile line.

II. ERT Profile B2

ERT profile B2 is situated in the center of the island and crosses the eastern lateral boundary of the previously mapped freshwater lens by Wightman (1990; Figure 2.2). In November 2011, a high resistivity zone with values ranging from 30 and 500 Ω·m corresponding to the unsaturated zone and the freshwater lens was relatively constant in thickness and extended to 6 m depth (Figure 2.7b). Minor variations within this zone likely correspond to variations in the rock and not the pore fluids. Below 6 m depth, throughout

the profile, resistivities decrease reaching values as low as 4 Ω·m. However, these depths lie below the DOI 0.2 contour and are not well constrained.

In November 2017, the resistivity values in the upper 1 m of the profile decreased to less than 15 Ω·m, indicating the emplacement of saline or brackish water near the surface (Figure 2.7c). This salinity inversion was most pronounced on the lower elevation portions of the profile between 170 m and 278 m where the resistivity decreased in places to less than 1 Ω·m. By May 2018, resistivities in this near-surface layer had increased slightly (Figure 2.7d). As with the resistivity decrease observed in November 2017, this increase in resistivity occurred in the lower elevation sections of the profile between 170 m to 278 m. By December 2018, in the upper 2 m depth, the resistivity increased on average to 31 Ω·m between 0 m to 180 m, whereas between 180 m and 278, the resistivity at most places is less than 15 Ω·m (Figure 2.7e).

The change in salinity observed between November 2011 and November 2017 in the upper 1 m of profile B2 is similar to that observed for profile B1. A significant increase was observed between the 170 m and 278 m, where the salinity increased from 3 to 10 PSU (Figure 2.8b). Below 2 m depth, the change in the salinity was minimal, whereas below 5 m depth, from 0 to 55 m and 125 to 278 m, the salinity increased by 3 - 10 PSU. Six months later (May 2018) the salinity decreased by up to 6 PSU in the upper 1 m of the section (Figure 2.8c). Between December 2018 to November 2011, the change in the salinity increased by up to 2 PSU, in the upper 2m depth from 0 to 110 m, whereas, in the lower elevation region, from 110m to 250m, the change in the salinity was minimal. Below 2 m depth, the change in salinity was not significant (Figure 2.8d).

III. ERT Profile B3

ERT profile B3 extends southward from a mangrove scrubland and is situated outside the freshwater lens defined by Wightman (1990; Figure 2.1). The resistivity on this profile was the lowest of all the three transects and increased from north to south along the profile reflecting an inland salinity decrease in the groundwater. In November 2011, low resistivity ranging from 2 to 5 Ω·m was situated in the upper 2 m of the section between 0 and 90 m (Figure 2.9b). A wedge shaped brackish lens consisting of resistivity between 5 and 20 Ω·m and defined by the 10 PSU salinity contour extended southward from 40 m on the profile. The resistivity was highest in a 2.5 m thick zone that extended southward from 90 m on the profile. The resistivity in this zone ranged from 20 to 37 Ω·m, which corresponds to the freshwater lens defined by the 3 PSU contour. Below 5 m depth, the resistivity was in general less than 3 Ω·m.

The resistivity change from November 2011 (pre-storm) to November 2017 (post-storm) was mainly restricted to the upper 2.5 m of the profile. Both the near-surface low resistivity zone and the seaward point of the brackish lens represented by the 10 PSU contour moved inland to the south by approximately 20 m. At the same depth, between 160 to 250 m, the freshwater lens represented by the 3 PSU contour decreased substantially, leaving only minimal freshwater pockets (Figure 2.9c). By May 2018, the near-surface low resistivity zone retreated northward by about 3 m (Figure 2.9d). The general size of the brackish lens remained the same but the freshwater pockets increased slightly in size. By December 2018, there was no significant change observed along the profile line (Figure 2.9e).

Similar to B1 and B2 ERT profiles, the change of salinity observed in B3 between November 2011 and 2017 is more pronounced on the top 2 m depth (Figure 2.10 b). In the top 2 m depth, throughout the profile, the salinity change increased by up to 4 PSU. Between 90 to 105 m, the salinity change increased in the range of 4 to 10 PSU. Below 2 m depth, throughout the profile, the salinity increased between 0 and 2 PSU. From November 2017 to May 2018, in the top 2 m, throughout the profile, the salinity change decreased by up to 6 PSU. Below 2 m depth, the salinity change was minimal and increased by up to 2 PSU (Figure 2.10c). Between December 2018 to November 2011, in the upper 2 m depth, the salinity change increased by up 3 PSU. Below 2 m depth, the change in the salinity observed was minimal (Figure 2.10d).

2.5. Discussion

2.5.1. The Impact of the storm surge on the freshwater lens

The well and ERT data collected about three to four months (November 2017/January 2018) after the storm showed the deposition of saline water on top of the freshwater lens. The post-Irma resistivity data indicate low resistivity/high salinity zones in the upper 2 m depth corresponding to saline water emplaced on top of the freshwater lens by the storm surge. This deposition of saline water on top of the freshwater lens defined by the 3 PSU contour line is observed in the lower elevation sections of the profiles. This low resistivity/ high salinity is clearly visible east of 130 m of profile B1 (Figure 2.5c), throughout profile B2 (Figure 2.7c), and between 160 to 250 m in B3 (Figure 2.9c). Therefore, these results demonstrate that the impact on the freshwater lens is influenced by topography.

Hurricane Irma approached the Florida Keys from the south and made landfall on Cudjoe Key, 15 km to the west of BPK (Cangialosi et al. 2018; Figure 2.2). The storm placed BPK in the strong right-front quadrant of the hurricane with southeasterly winds at landfall. These southeasterly winds produced maximum storm surge heights of up to 2.4 m NAVD88 on the south and eastern shores of the island (USGS 2017; Cangialosi et al. 2018). This pattern is reflected by both the ERT and well measurements. The Well data collected on September 27, 2017, showed an abrupt increase in salinity at most wells along profile B2 in the center and profile B3 on the southern side of the island (Figure 2.4b and 2.4c), whereas little change was observed along profile B1 on the western side of the island (Figure 2.4a). On ERT profile B1, the greatest increase in salinity occurred in low lying portions on the eastern end of the profile (Figure 2.6a and 2.6b), whereas on profiles B2 and B3 the salinity increase occurred throughout each profile (Figure 2.8b and 2.10b). This suggests that the highest storm surge flooded the island from the east, confirmed by independent observations. Our field observations of debris indicate that the impact of the storm surge was less along the western margin of the island (Ross et al. 2019) and damage to buildings on the island was greatest on the eastern side (Xian et al. 2018). Therefore, these results suggest that the impact on the freshwater lens was more pronounced on the eastern side of the island.

The impact of the storm surge on the freshwater lens is most pronounced at lower elevations. In the upper 2 m, the salinity increased significantly between 4 and 10 PSU on the western and eastern ends of profile B1 (Figure 2.6b), east of 130 m on profile B2 (Figure 2.8b), and between 0 to 110 m on profile B3 (Figure 2.10b). This pattern suggests that the topography of oceanic islands plays a crucial role in the fate of storm surge.

Depending on the topography of the oceanic islands, storm surge flooding either infiltrates into the ground or runs off as overland flow that either flows to the coast or settles in the depressions. Through time, the accumulated saline water in the depressions either evaporates or infiltrates to the ground, where the infiltrated portion leads to significant saltwater deposition in the lower topography.

The ERT results throughout profile B1 (Figure 2.5c) and in the lower elevation of profile B2 (Figure 2.7c) showed the base of the freshwater lens, as indicated by the 3 PSU contour, depressed downward after the storm surge. The freshwater lens is approximately 5 m thick and increases inland along profiles B1 and B2 (Figure 2.5 and 2.7). After Irma, the higher density saline water emplaced by the storm surge depressed the freshwater lens along these profiles. This higher density saline water on top of less dense freshwater has an unstable configuration and tends to penetrate through the freshwater lens. In combination with freshwater recharge, this stratification may be overturned (Villholth et al. 2008; Terry and Falkland 2010).

Prior to Irma, profile B3 had only a 2.5 m thick freshwater lens south of 160 m (Figure 2.9b). The storm surge from Irma largely destroyed this freshwater lens leaving only minimal freshwater pockets (Figure 2.9c). This is in contrast to profiles B1 and B2 that had pre-storm lenses approximately 5 m thick that were overridden and depressed by saline water but not destroyed. This suggests that thin freshwater lenses are susceptible to being completely destroyed by a storm surge.

The storm surge deposition of saline water above the freshwater lens has a tremendous effect on the ecological structure (Ogurcak 2015). The accumulated saline water infiltrating through the unsaturated zone and into the saturated zone results in increased mortality of

the freshwater dependent species (Ross et al. 2019). For example, in the pine forests, a fresh water-dependent species in BPK showed a significant reduction in the lower elevation areas and persisted only in the higher elevation sites (Ross et al. 2019). This phenomenon has a cascading effect on the overall ecosystem dynamics. The impact of the storm surge inundation on the ecosystem can be more severe, especially when multiple storm surge events impacted the same site repeatedly (Anderson and Lauer 2008).

2.5.2. The Recovery history of the freshwater lens

The well and ERT data collected eight months (May 2018) and fifteen months (December 2018) after the storm showed limited recovery of the lens despite intense precipitation. The cumulative precipitation recorded at BPK showed large precipitation events in September 2017 and May 2018 (Figure 2.3). During the Irma event in September 2017, over 36 cm of precipitation was recorded. Since this occurred coincident with the storm surge event, its input likely contributed little to the recovery of the lens. During a two week period of intense precipitation in May 2018, over 42 cm of precipitation was recorded. This heavy rainfall occurred during the sub-tropical storm Alberto (25- 31 May 2018; Berg 2018). The May 2018 event occurred at the end of the climatological dry season and less than 20 cm of precipitation occurred between these two events. Between June to December 2018, the cumulative precipitation recorded was 65 cm and contributed to the recovery of the lens. A single large precipitation event can have a large impact on the recharge of small islands (Ogurcak and Price. 2018). As a result of this, the salinity in the wells and ERT data collected eight and fifteen months after the storm revealed 40 % and 70 % recovery. The Well data along profiles B2 and B3 clearly showed the decrease of

salinity by May and December 2018. These decrements in salinity suggest recovery of the freshwater lens due to precipitation.

Similar to the post-storm impact, the freshwater lens recovery is more pronounced at the lower elevations. In May 2018, the ERT image along profile B1 showed some recovery along the lower elevations and was most pronounced east of 130 m, where the salinity decreased to less than 3 PSU (Figure 2.5d). The resistivity along profile B2 showed some recovery along the lower elevation sections, where the salinity greater than 10 PSU is less apparent (Figure 2.7d). Furthermore, along profile B3, the thin freshwater lens that largely disappeared after Irma started to recover south of 180 m (Figure 2.9d). The salinity change after Irma, between May and January 2018 along profile B1 and between May 2018 and November 2017 along profile B2 and B3, showed a decrease of salinity in the top 2 m. These decreases in salinity are pronounced more in the lower elevations, east of 130 m on profile B1 (Figure 2.6c), east of 180 m on profile B2 (Figure 2.8c), and north of 110 m on profile B3 (Figure 2.10c). In December 2018, the ERT image along Profile B1 displayed recovery east of 220 m (Figure 2.5e). The resistivity along profile B2 increased to greater than 10 Ω·m in several locations. This is demonstrated throughout the profile line by decrease in the number of rounded shapes, greater than 3 PSU (Figure 2.7e). This suggests that the freshwater recovery due to precipitation is most pronounced in low elevation regions.

In a study conducted in the Pukapuka Atoll in the Northern Cook Islands, the freshwater lens required 11 months to recover after a tropical cyclone. However, a saltwater plume remained at depth for 26 months (Terry et al. 2010). Similarly, in Lake Pontchartrain in southeastern Louisiana after Hurricanes Katrina and Rita, the chloride concentration in

the wells required 10 months to recover (Van Biersel et al. 2007). In the lower Keys, after Hurricane Georges, the salinity increased more than 15 PSU and did not improve for several months after the storm (Lopez et al. 2003). Our results indicate that eight and fifteen months after the storm, the salinity is on average 5 PSU (60%) and 2 PSU (30%) higher than the pre-storm conditions. Precipitation received during the 2019 wet season (May-November) likely contributed to continued recovery of the lens.

2.6. Conclusions

In this study, we investigated the effect of the Hurricane Irma storm surge on the freshwater lens of Big Pine Key, FL using Electrical Resistivity Tomography (ERT) on three profiles of 222 m, 250 m, and 278 m length. We compared ERT imaging results of baseline data collected 6 years before Irma (November 2011) with data collected about three to four months (November 2017/January 2018) and eight months (May 2018) and fifteen months (December 2018) after the storm. For the November 2017/January 2018 data, all profiles showed low resistivity/high salinity zones in the upper 2 m, suggested the deposition of the saline water on the top of the freshwater lens. This increase in salinity is most pronounced in the low elevation portions of the profiles. Hurricane Irma made landfall on the southern direction of BPK and the impact of the storm surge is more pronounced on the low-lying eastern side of the island.

The May 2018 data were collected at the end of the climatological dry season, but were collected immediately after 2 weeks of intense precipitation. This freshwater recharge showed some limited recovery of the freshwater lens. This recovery is most pronounced in the lower elevation portions of the profiles, where standing water was observed during data

collection. Similarly, in December 2018, the freshwater recovered due to the precipitation received during the wet season (May-November) of 2018. Yet, the freshwater lens is not recovered fully. This suggests that both the impact of storm surge and the freshwater recovery due to precipitation are most pronounced in low elevation regions where both saline and freshwater can collect at the surface.

2.7. References

Anderson Jr, W. P., and R. M. Lauer. 2008. The role of overwash in the evolution of mixing zone morphology within barrier islands. *Hydrogeology journal* 16(8): 1483-1495.

Archie, G. E. 1942. The electrical resistivity log as an aid in determining some reservoir characteristics. *Transactions of the AIME* 146(01): 54-62.

Bailey, R. T., J. W. Jenson, and A. E. Olsen. 2009. Numerical modeling of atoll island hydrogeology. *Groundwater* 47(2): 184-196.

Bender, M. A., T. R. Knutson, R. E. Tuleya, J. J. Sirutis, G.A. Vecchi, S. T. Garner, and I. M. Held. 2010. Modeled impact of anthropogenic warming on the frequency of intense Atlantic hurricanes. *Science* 327: 454-458.

Berg, R. 2018. Tropical storm Alberto (25 – 31 May 2018), *Tropical Cyclone Reports*, National Hurricane Center, https://www.nhc.noaa.gov/data/tcr/AL012018_Alberto.pdf

Binley, A. 2019. R2 (Version 3.3). *Lancaster University archive*. www.es.lancs.ac.uk/people/amb-/Freeware/R2/R2.htm.

Binley A., and A. Kemna. 2005. DC Resistivity and Induced Polarization Methods. In *Hydrogeophysics. Water Science and Technology Library*, eds. *Y.* Rubin and S.S. Hubbard, 129–156. Dordrecht: Springer.

Cangialosi, J. P., A. S. Latto, and R. Berg. 2018. Hurricane Irma (30 August - 12 September 2017). *Tropical Cyclone Reports*, National Hurricane Center, https://www.nhc.noaa.gov/data/-tcr/AL112017_Irma.pdf.

Carrière, S. D., K. Chalikakis, C. Danquigny, and L. Torres-Rondon. 2017. Using resistivity or logarithm of resistivity to calculate depth of investigation index to assess reliability of electrical resistivity tomography. *Geophysics 82*(5): EN93-EN98.

Caterina, D., A. F Orozco, and F. Nguyen. 2017. Long-term ERT monitoring of biogeochemical changes of an aged hydrocarbon contamination. *Journal of contaminant hydrology* 201: 19-29.

Chang, S. W., T. P. Clement, M. J. Simpson, and K. K. Lee. 2011. Does sea-level rise have an impact on saltwater intrusion? *Advances in Water Resources* 34(10): 1283–1291.

Chui, T. F. M., and J. P. Terry. 2012. Modeling fresh water lens damage and recovery on atolls after storm-wave washover. *Groundwater* 50(3): 412-420.

Church, J. A., and N. J. White. 2006. A 20th century acceleration in global sea-level rise. *Geophysical research letters 33*(1).

Constable, S. C., R. L. Parker, and C. G. Constable. 1987. Occam's inversion: A practical algorithm for generating smooth models from electromagnetic sounding data. *Geophysics 52*(3): 289-300.

De Franco, R., G. Biella, L. Tosi, P. Teatini, A. Lozej, B. Chiozzotto, and V. Bassan. 2009. Monitoring the saltwater intrusion by time lapse electrical resistivity tomography: The Chioggia test site (Venice Lagoon, Italy). *Journal of Applied Geophysics* 69(3-4): 117-130.

Falkland, A., and E. Custodio. 1991. Conditions for freshwater occurrence in small islands. In *Hydrology and Water Resources of Small Islands:* A practical guide: A contribution to the international hydrological programme, IHP-III, Project 4.6, eds. A. Falkland, E. Custodio, A. Diaz Arenas, and L. Simler, 27–43. Paris: UNESCO.

Fish, J. E., and M.T. Stewart. 1991. Hydrogeology of the surficial aquifer system, Dade County, Florida. *U.S. Geological Survey Water-Resources Investigations Report* 90-4108. doi: 10.3133/wri904108.

Goebel, M., A. Pidlisecky, and R. Knight. 2017. Resistivity imaging reveals complex pattern of saltwater intrusion along Monterey coast. *Journal of Hydrology* 551: 746-755.

Halley, R. B., H. L. Vacher, and E.A. Shinn. 1997. Geology and hydrogeology of the Florida Keys. In *Geology and hydrogeology of carbonate islands*, eds. H. L. Vacher, and T. M. Quinn, 217-248. Amsterdam: Elsevier.

Hanson, C. E. 1980. Freshwater resources of Big Pine Key, Florida. *U.S. Geological Survey Open-File Report* 80-447. doi: 10.3133/ofr80447

Holding, S., and D. M. Allen. 2015. Wave overwash impact on small islands: Generalised observations of freshwater lens response and recovery for multiple hydrogeological settings. *Journal of Hydrology* 529: 1324-1335.

Horel, J., M. Splitt, L. Dunn, J. Pechmann, B. White, C. Ciliberti, ... and J. Burks. 2002. Mesowest: Cooperative mesonets in the western United States. *Bulletin of the American Meteorological Society 83*(2): 211-226.

Huizer, S., M. C. Karaoulis, G. H. P. Oude Essink, and M. F. P. Bierkens. 2017. Monitoring and simulation of salinity changes in response to tide and storm surges in a sandy coastal aquifer system. *Water Resources Research* 53(8): 6487–6509.

Keim, B. D., R. A. Muller, and G.W. Stone. 2007. Spatiotemporal patterns and return periods of tropical storm and hurricane strikes from Texas to Maine. *Journal of climate* 20(14): 3498-3509.

Kemna, A., J. Vanderborght, B. Kulessa, and H. Vereecken. 2002. Imaging and characterisation of subsurface solute transport using electrical resistivity tomography (ERT) and equivalent transport models. *Journal of Hydrology* 267(3-4): 125-146.

LaBrecque, D. J., and X. Yang. 2001. Difference inversion of ERT data: A fast inversion method for 3-D in situ monitoring. *Journal of Environmental and Engineering Geophysics* 6(2): 83-89.

Langevin, C. D., M. T. Stewart, and C. M. Beaudoin. 1998. Effects of sea water canals on fresh water resources: An example from Big Pine Key, Florida. *Ground Water* 36(3): 503–513.

Lopez, R. R., N. J. Silvy, R. F. Labisky, and P. A. Frank. 2003. Hurricane impacts on Key deer in the Florida Keys. *The Journal of wildlife management* 67(2): 280-288.

Morgan, L. K., and A. D. Werner. 2014. Seawater intrusion vulnerability indicators for freshwater lenses in strip islands. *Journal of hydrology 508*: 322-327.

Neal, A., M. Grasmueck, D. F. McNeill, D. A. Viggiano, and G. P. Eberli. 2008. Full-resolution 3D radar stratigraphy of complex oolitic sedimentary architecture: Miami Limestone, Florida, U.S.A. *Journal of Sedimentary Research* 78(9): 638–653.

NOAA, NCDC. 2018. NOAA National Centers for Environmental Information (NCEI). https://www.ncdc.noaa.gov/.

Nowroozi, A. A., S. B. Horroceos, and P. Henderson. 1999. Saltwater intrusion into the freshwater aquifer in the eastern shore of Virginia: a reconnaissance electrical resistivity survey. *Journal of Applied Geophysics* 42(1): 1-22.

Ogurcak, D. E. 2015. The effect of disturbance and freshwater availability on lower Florida Keys' coastal forest dynamics. *FIU Electronic Theses and Dissertations*. 2288. http://digitalcommons.fiu.edu/etd/2288

Ogurcak, D. E., and R. Price. 2018. Groundwater geochemistry fluctuations along a fresh-saltwater gradient on the carbonate islands of the lower Florida Keys. *Chemical Geology*. doi: 10.1016/j.chemgeo.2018.09.032

Oldenburg, D. W., and Y. Li. 1999. Estimating depth of investigation in dc resistivity and IP surveys. *Geophysics 64*(2): 403-416.

Pasch, R. J., L. A. Avila, and J. L. Guiney, J. 2001. Atlantic hurricane season of 1998. *Monthly Weather Review 129*(12): 3085-3123.

Pasch, R. J., E. S. Blake, H. D. Cobb III, and D. P. Roberts. 2006. Hurricane Wilma (15 – 25 October 2005). *Tropical cyclone report*: National Hurricane Center. https://www.nhc.noaa.gov/data/tcr/AL252005_Wilma.pdf.

Ranjan, P., S. Kazama, and M. Sawamoto. 2006. Effects of climate change on coastal fresh groundwater resources. *Global Environmental Change* 16(4): 388-399.

Robins, N. S., and A. R. Lawrence. 2000. Some hydrogeological peculiar to various types of problems small islands. *Water and Environment Journal 14*(5): 341-346.

Rosales, R., P. Martínez-Pagan, A. Faz, and J. Moreno-Cornejo. 2012. Environmental monitoring using electrical resistivity tomography (ERT) in the subsoil of three former petrol stations in SE of Spain. *Water, Air and Soil Pollution* 223(7): 3757-3773.

Ross, M. S., J. J. O'Brien, and L. J. Flynn. 1992. Ecological site classification of Florida Keys terrestrial habitats. *Biotropica* 24(4): 488-502.

Ross, M. S., J. J. O'Brien, R. G. Ford, K. Zhang, and A. Morkill. 2009. Disturbance and the rising tide: the challenge of biodiversity management on low-island ecosystems. *Frontiers in Ecology and the Environment* 7(9): 471-478.

Ross, M. S, D. E. Ogurcak, S. Stoffella, J. P. Sah, J. Hernandez, and H. E. Willoughby. 2019. Hurricanes, storm surge, and Pine forest decline on a low limestone Island. *Estuaries and Coasts*. doi: 10.1007/s12237-019-00624-z

Saha, A. K., S. Saha, J. Sadle, J. Jiang, M. S. Ross, R.M. Price,... and K. S. Wendelberger. 2011. Sea level rise and South Florida coastal forests. *Climatic Change 107*(1-2): 81-108.

Scott T. M. 2001. Text to accompany the geologic map of Florida. *Florida Geological Survey Open File Report* 80.

Simyrdanis, K., N. Papadopoulos, P. Soupios, S. Kirkou, and P. Tsourlos. 2018. Characterization and monitoring of subsurface contamination from olive oil mills' waste waters using electrical resistivity tomography. *Science of The Total Environment* 637: 991-1003.

Stewart, M. 1988. Electromagnetic mapping of fresh-water lenses on small oceanic islands. *Groundwater* 26(2): 187-191.

Terry, J. P., and A. C. Falkland. 2010. Responses of atoll freshwater lenses to storm-surge overwash in the Northern Cook islands. *Hydrogeology Journal* 18(3): 749-759.

Tucker, N. M. 2013. Analyzing tidal fluctuations in the Big Pine Key freshwater lens with time-lapse resistivity. *FIU Electronic Theses and Dissertations*. Paper 947. http://digitalcommons.fiu.edu/etd/947

USGS 2017. USGS measures the impacts of Hurricane Irma. *U.S. Geological Survey*. https://www.usgs.gov/news/usgs-measures-impacts-hurricane-irma.

Van Biersel, T. P., D. A. Carlson, and L. R. Milner. 2007. Impact of hurricanes storm surges on the groundwater resources. *Environmental geology 53*(4): 813-826.

Villholth, K. G., P. Amerasinghe, and P. Jeyakumar. 2008. Tsunami impacts on shallow groundwater and associated water supplies on the east coast of Sri Lanka. In *Groundwater for sustainable development: problems, perspectives and challenges*, eds. P. Bhattacharya, A. L. Ramanathan, A. B. Mukherjee, J. Bundschuh, D. Chandrasekharam, A. K. Keshari, 211-222. London: Taylor and Francis Publications.

Wagner, R. J., R. W. Boulger Jr, C. J. Oblinger, and B. Smith. 2006. Guidelines and standard procedures for continuous water-quality monitors: station operation, record computation, and data reporting: Techniques and Methods. 1-D3. *U.S. Geological Survey*. doi:10.3133/tm1D3.

Wightman, M. J. 1990. Geophysical analysis and Dupuit-Ghyben-Herzberg modeling of fresh-water lenses on Big Pine Key, Florida. *M.S Thesis, University of South Florida*, Tampa FL, USA.

Xian, S., K. Feng, N. Lin, R. Marsooli, D. Chavas, J. Chen, and A. Hatzikyriakou. 2018. Brief communication: Rapid assessment of damaged residential buildings in the Florida Keys after Hurricane Irma, *Nat. Hazards Earth Syst. Sci*.18: 2041–2045.

Yang, J., T. Graf, and T. Ptak. 2015. Sea level rise and storm surge effects in a coastal heterogeneous aquifer: a 2D modelling study in northern Germany. *Grundwasser 20*(1): 39-51.

Zohdy, A. A. R., P. M. Martin, and R. J. Bisdorf. 1993. A study of seawater intrusion using direct-current soundings in the southeastern part of the Oxnard Plain, California. *U.S. Geological Survey Open-File Report* 93-524. doi: 10.3133/ofr93524

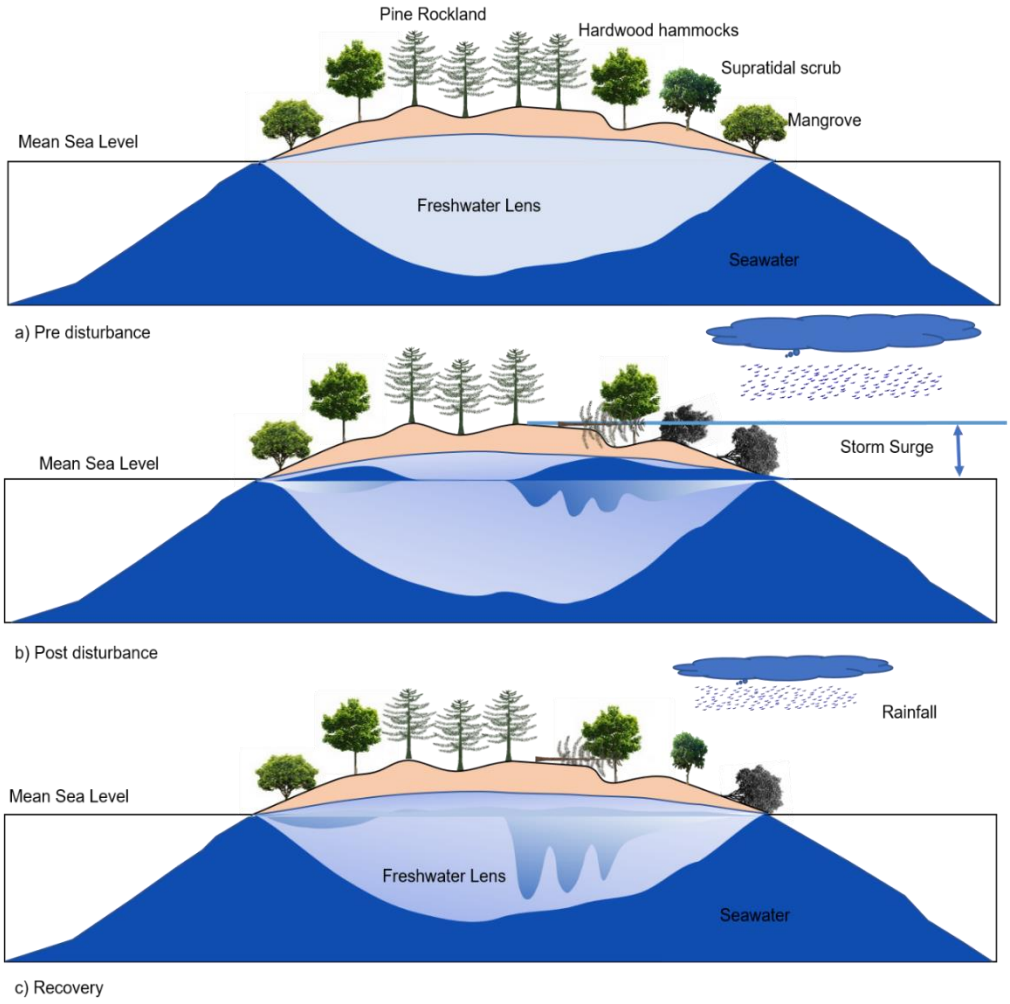

Figure 2.1: Conceptual model of the effect of storm surge inundation on oceanic islands and coastlines. (a) Pre disturbance condition. (b) Post disturbance condition showing the impact of the storm surge on the freshwater lens, where saline water is deposited on the top of the freshwater lens, and forest communities are impacted. (c) Recovery, where the freshwater salinity adjusted to pre-disturbance conditions and forest communities are restored (after Saha et al. 2011).

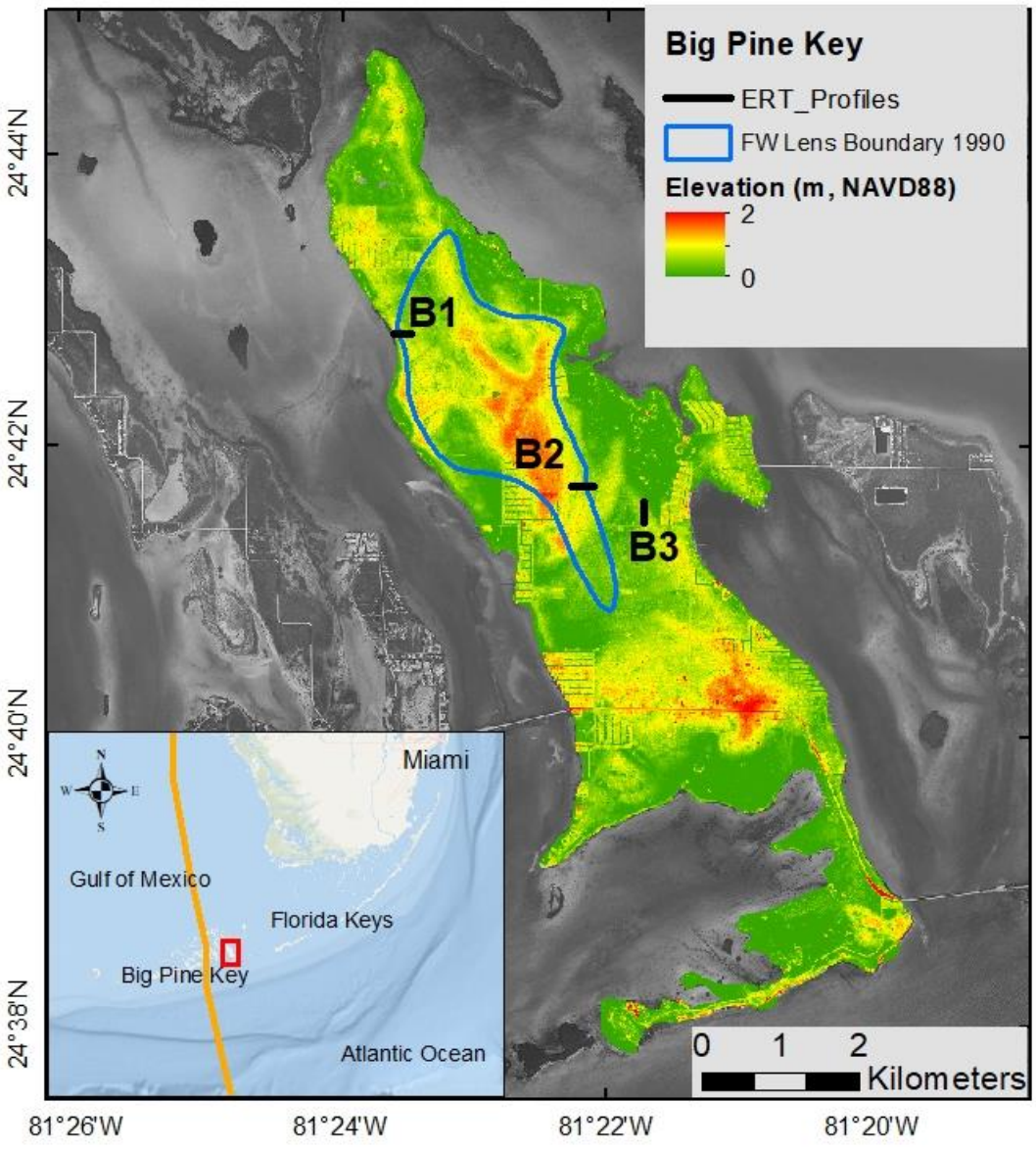

Figure 2.2: Location of the study area. Locations on BPK showing the Hurricane Irma track, the ERT profiles, and elevation (LIDAR data of 1 m2 resolution) in m. The contour line defines the freshwater lens boundary mapped by Wightman, (1990).

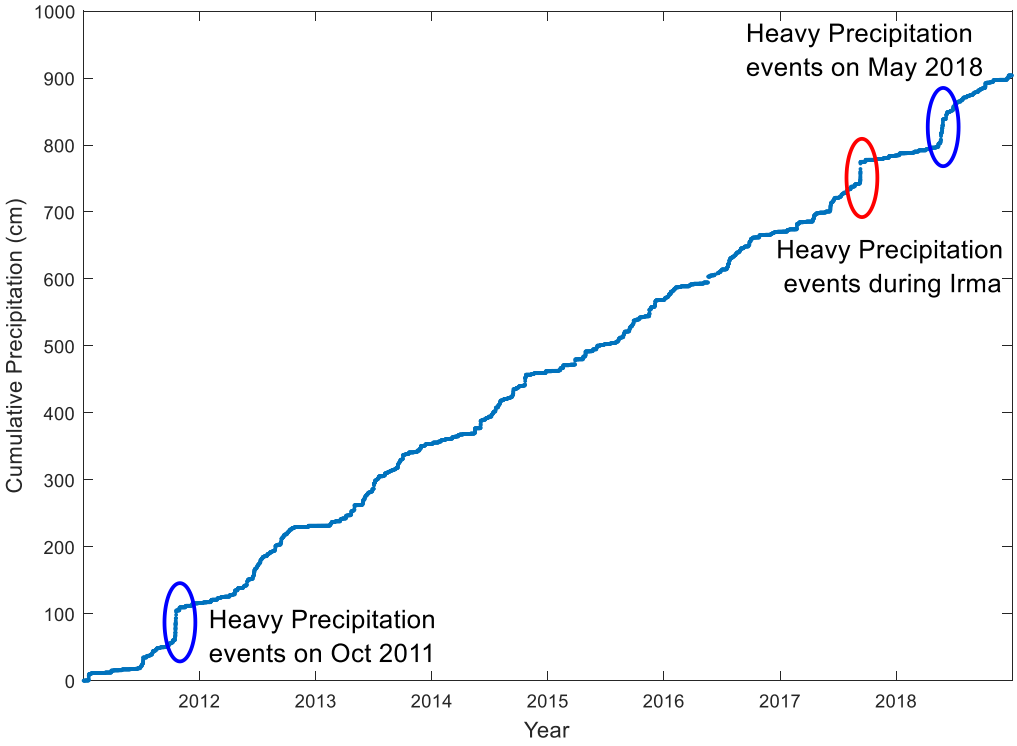

Figure 2.3: Cumulative precipitation at the National Key Deer Refuge, Big Pine Key, FL, US station (TS607) from Jan 1, 2011 to Dec 31, 2018. The cumulative rainfall data is from https://mesowest.utah.edu (Horel et al. 2002). The blue ellipses indicate large non-tropical (Oct 2011) and sub-tropical (May 2018) precipitation events and the red ellipse corresponds to precipitation from Hurricane Irma.

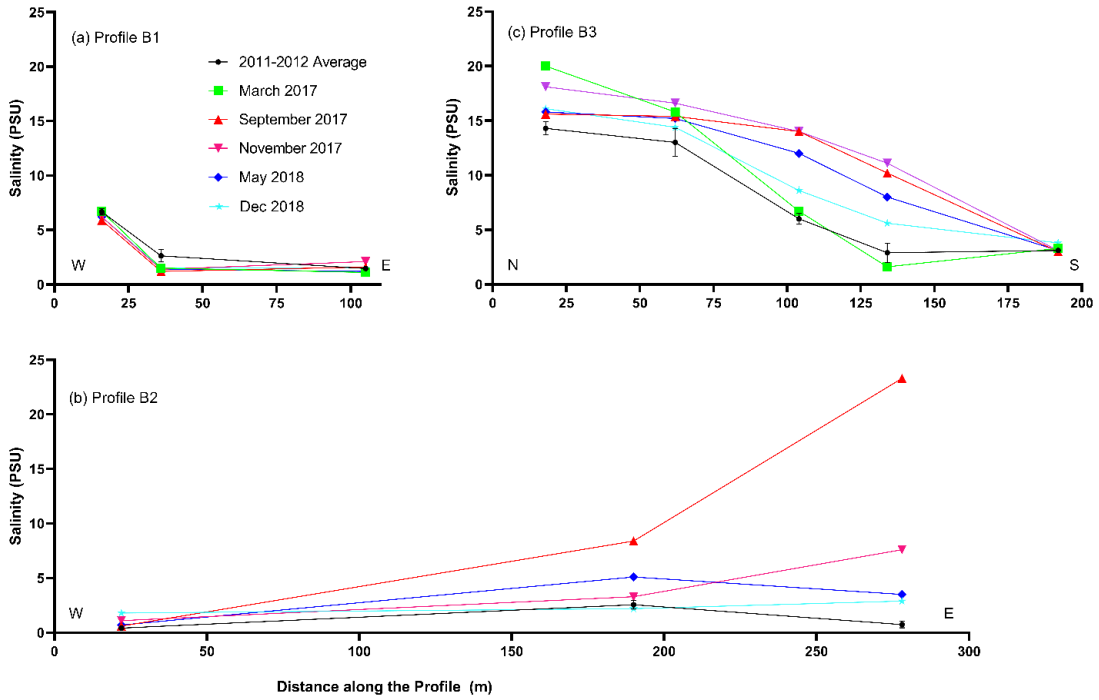

Figure 2.4:Salinity recorded in the monitoring wells adjacent to the ERT profiles. a) Profile B1; b) Profile B2; c) Profile B3. Horizontal locations are relative to the start of each ERT profile (Figure 2.2).

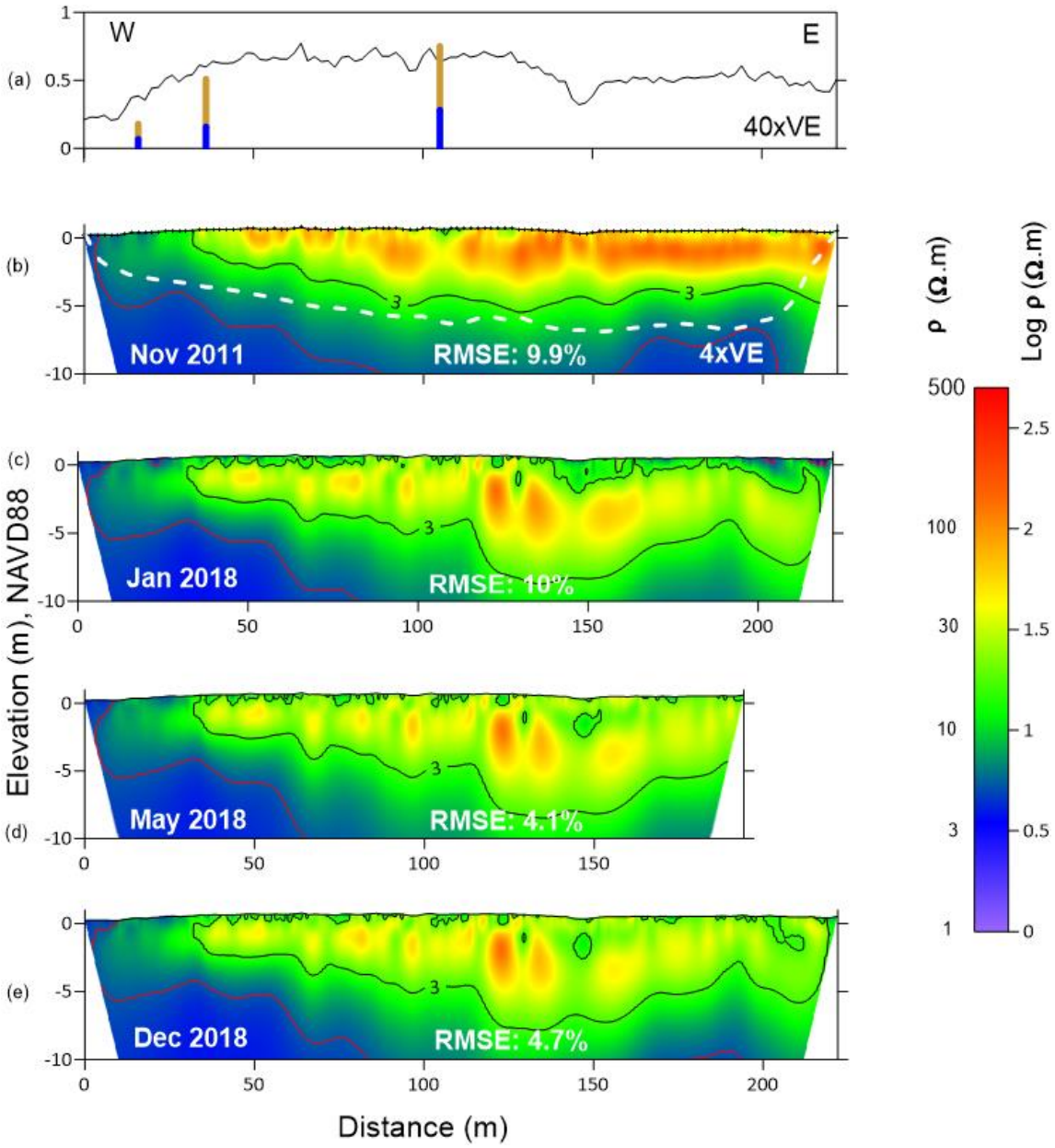

Figure 2.5: ERT resistivity models on profile B1. a. Topography. The gold and blue lines indicate the unsaturated and saturated zone in the wells; b. November 2011; c. January 2018; d. May 2018; e. December 2018. The black and red contour line represents a salinity of 3 and 10 PSU. The 0.2 DOI index is shown as a dashed line. The location of the profiles is shown in Figure 2.2. Elevations are relative to NAVD88.

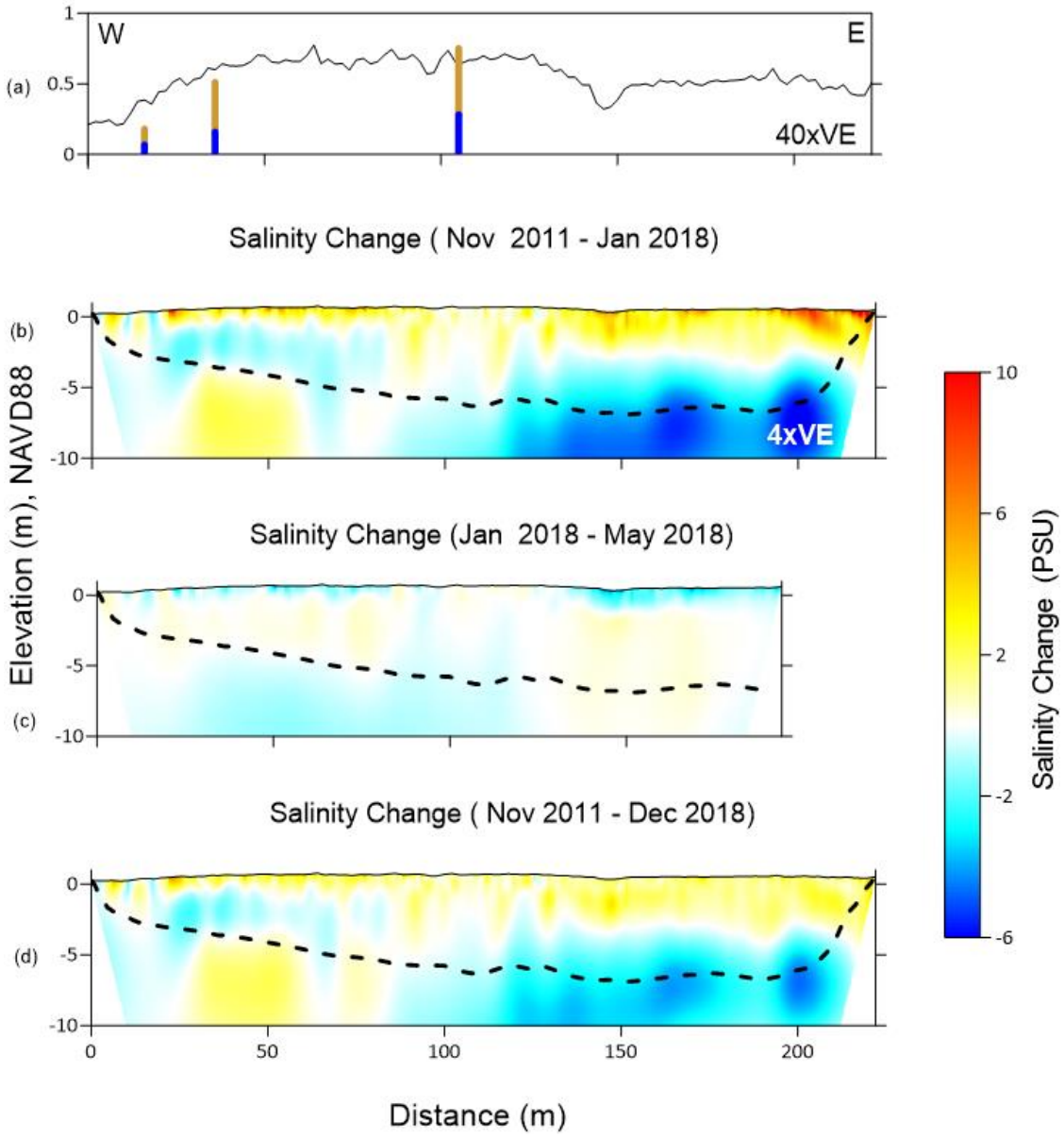

Figure 2.6: Salinity change on profile B1. a. Topography. The gold and blue lines indicate the unsaturated and saturated zone in the wells. Salinity change difference (b) between January 2018 and November 2011; (c). between May 2018 and January 2018 and (d) between December 2018 and November 2011. The 0.2 DOI index is shown as a dashed line. Elevations are relative to NAVD88.

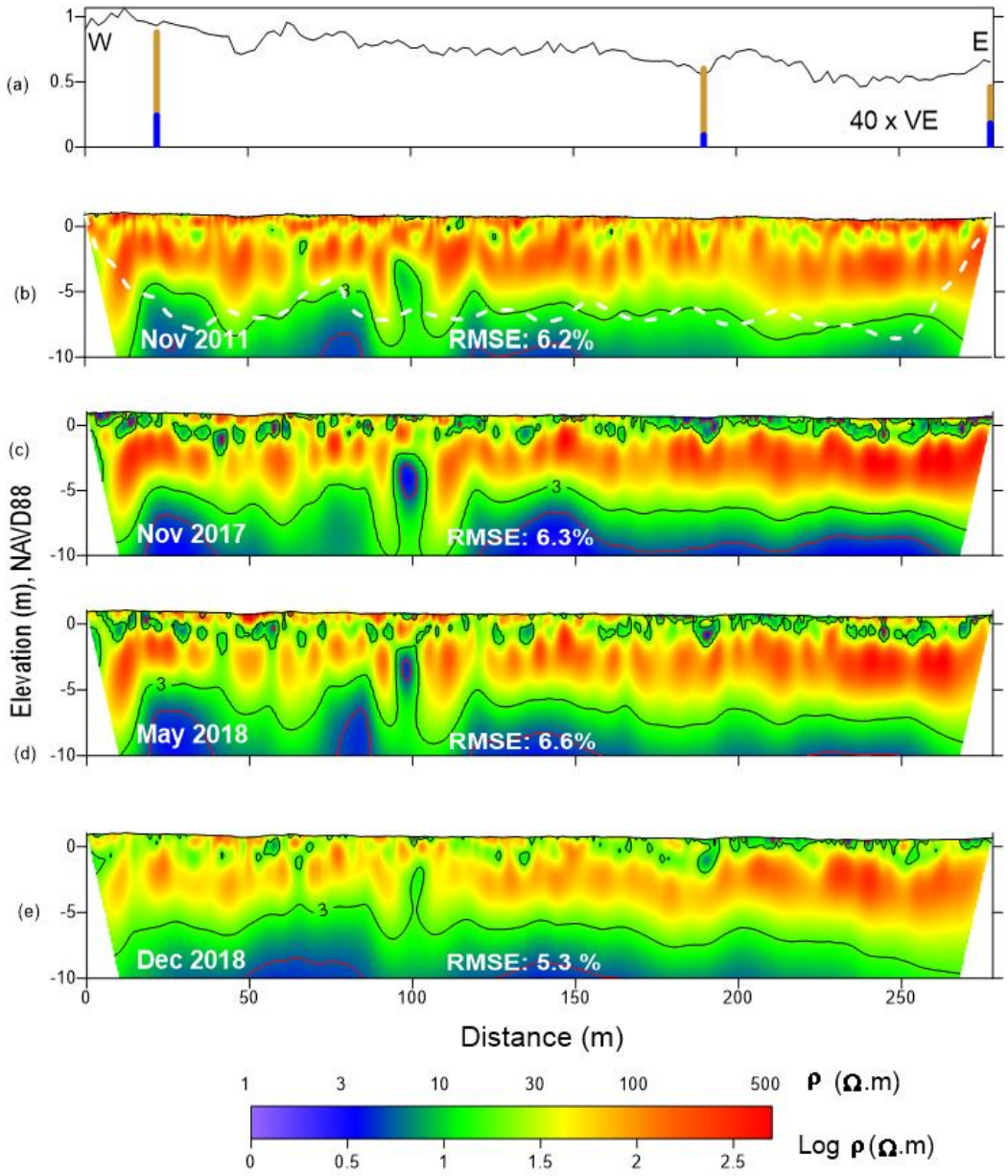

Figure 2.7: ERT resistivity models on profile B2. a. Topography. The gold and blue lines indicate the unsaturated and saturated zone in the wells; b. November 2011; c. November 2017; d. May 2018; e. December 2018. The black and red contour line represents a salinity of 3 and 10 PSU. The 0.2 DOI index is shown as a dashed line. Elevations are relative to NAVD88.

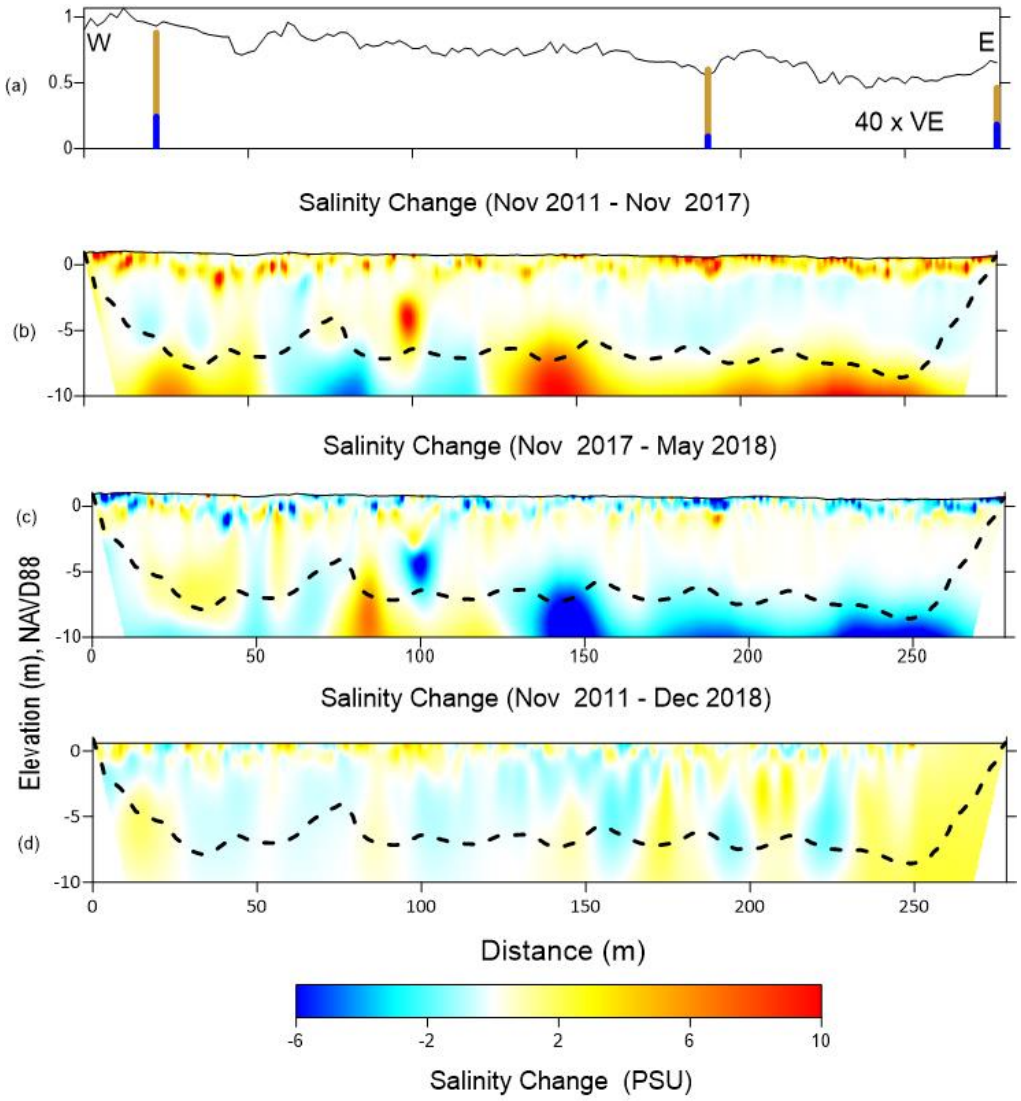

Figure 2.8: Salinity change on profile B2. a. Topography. The gold and blue lines indicate the unsaturated and saturated zone in the wells. Salinity change difference (b) between November 2017 and November 2011; (c). between May 2018 and November 2017 and (d). between December 2018 and November 2011. The 0.2 DOI index is shown as a dashed line. The black and red contour line represents a salinity of 3 and 10 PSU. Elevations are relative to NAVD88.

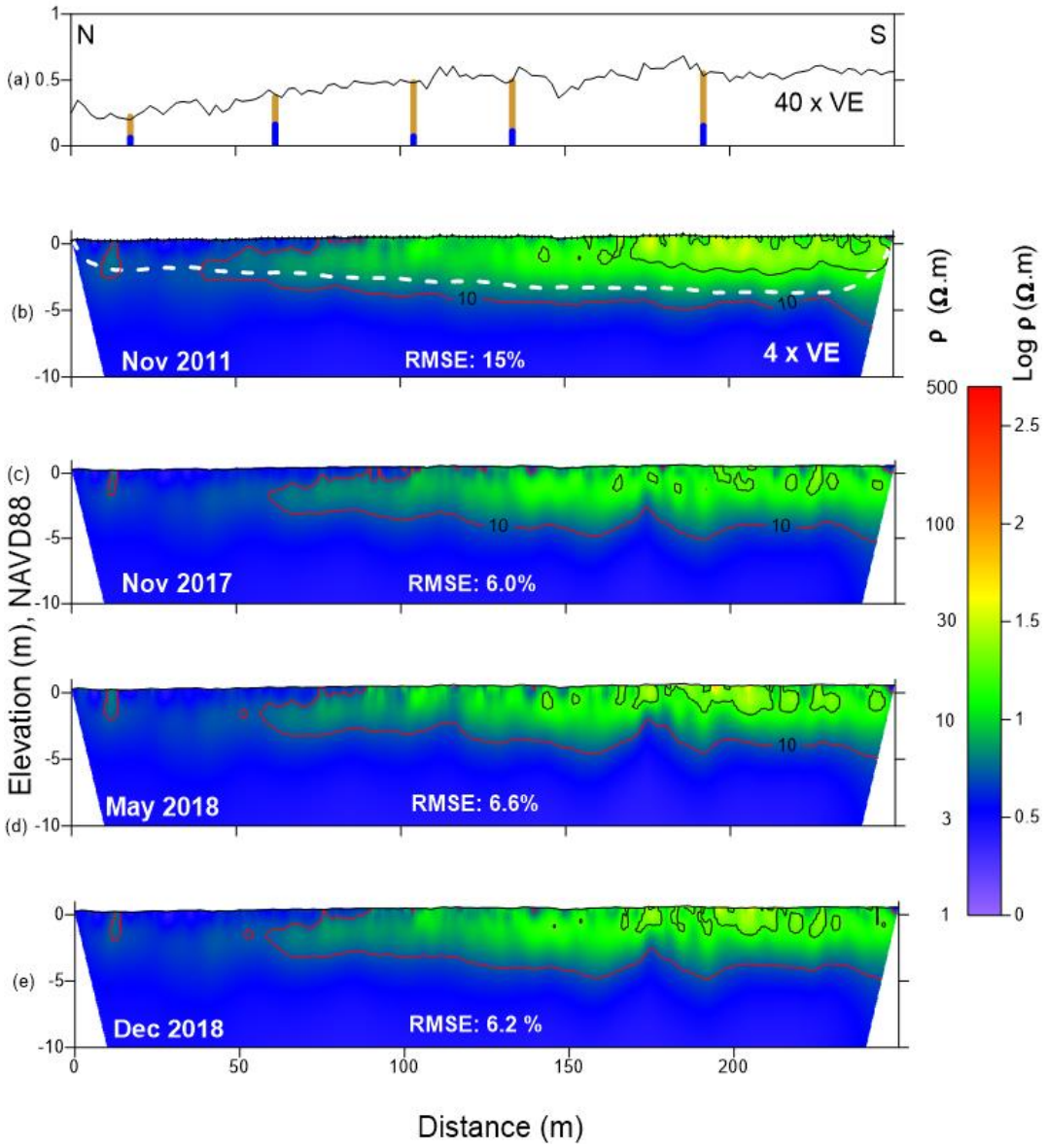

Figure 2.9: ERT resistivity models on profile B3. a. Topography. The gold and blue lines indicate the unsaturated and saturated zone in the wells; b. November 2011; c. November 2017; d. May 2018; e. December 2018. The black and red contour line represents a salinity of 3 and 10 PSU. The 0.2 DOI index is shown as a dashed line. The location of the profiles is shown in Figure 2.2. Elevations are relative to NAVD88.

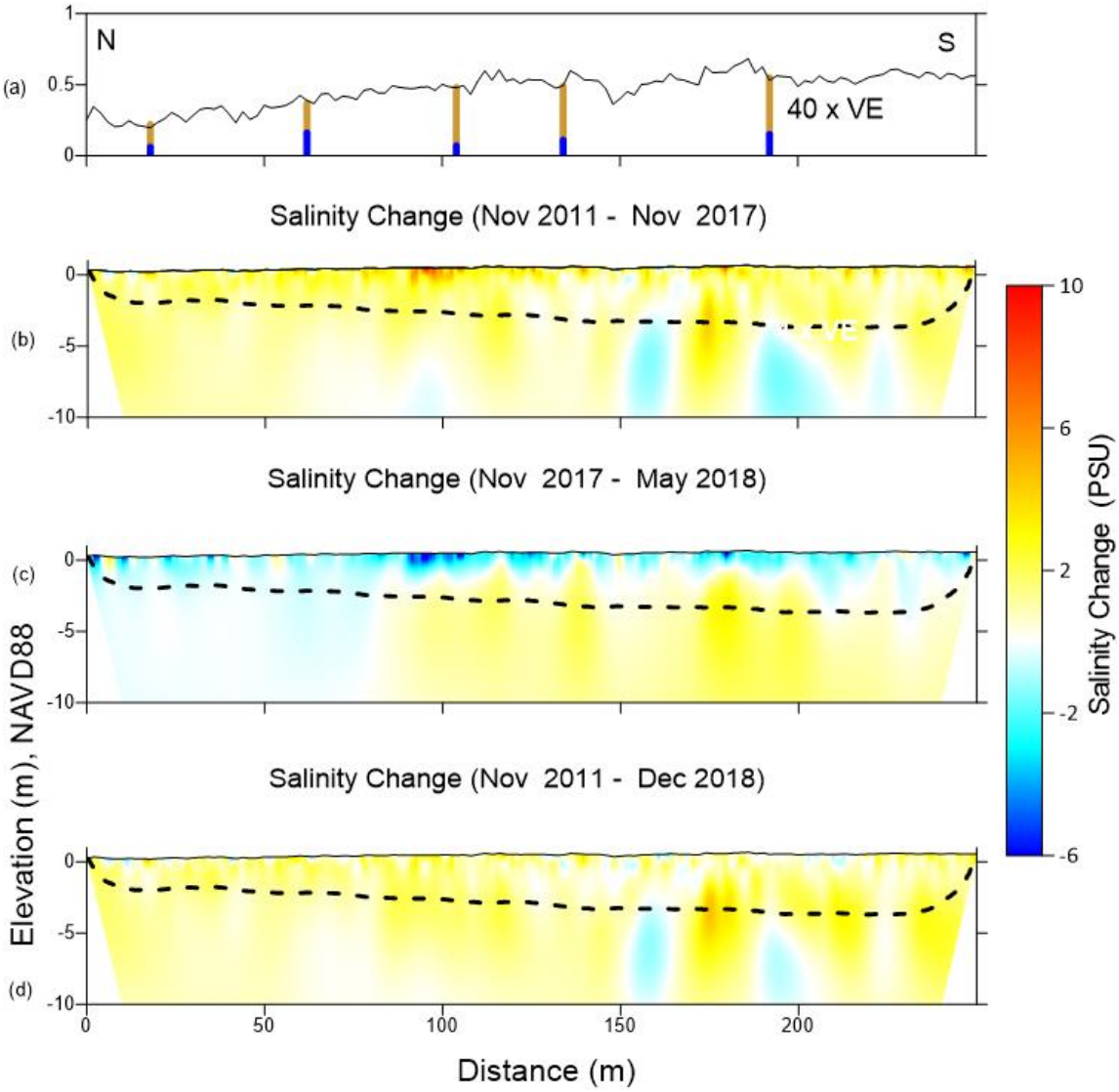

Figure 2.10: Salinity change on profile B3. a. Topography. The gold and blue lines indicate the unsaturated and saturated zone in the wells. Salinity change difference (b) between November 2017 and November 2011; (c). between May 2018 and November 2017 and (d) between December 2018 and November 2011. The 0.2 DOI index is shown as a dashed line. The location of the profiles is shown in Figure 2.2. Elevations are relative to NAVD88.

3. Geophysical Mapping of Freshwater Lens in Big Pine Key, Florida: Electromagnetic Induction Calibration and Application

Abstract

Electrical resistivity and electromagnetic methods are rapid and noninvasive geophysical techniques for measuring groundwater properties and characterizing the spatial and temporal variability of subsurface formations. However, to quantitatively interpret the EM data, the systematic error due to calibration problems and random error must be accounted for consideration. We conducted coincident EM and electrical resistivity tomography surveys in January and December 2018 on Big Pine Key, FL. In this study, we used vertical electrical sounding data extracted from an ERT measurement to calibrate the EM data. The inverted VES were used as input in the electromagnetic forward model to estimate the quadrature response component. Then, the observed offset between the calculated and observed quadrature data was corrected using a multiple linear regression model. Finally, the calibrated quadrature data were converted to apparent electrical conductivity and used to assess the temporal and spatial variation and inverted as a 2-layer model using the full solution and the low induction approximation.

The EM data showed that the observed quadrature value was underestimated compared to the calculated value in all frequencies. Hence, we derived a multiple linear regression model and gave a good agreement between the calculated and calibrated quadrature data. The predictive power of the multiple linear regression assessed using the Nash-Sutcliffe efficiency and the R^2 value 0.93 indicates the accuracy of the model. We used the multiple linear equations and calibrate the EM dataset that extended to 2.2 Km profile line. The

apparent electrical conductivity change, between January to December 2018, decreased in the lower elevation of the profile line and suggested the freshwater lens recovery due to precipitation. Besides, the 2-layer inverted data using the full solution and low induction approximation gives a reasonable fit, and the depth of the freshwater interface increased by December 2018 and suggests the recovery of the freshwater lens. Based on this study, we concluded the VES at pilot locations can be used for calibration purposes and verification of the accuracy of EM measurements.

3.1. Introduction

The frequency-domain electromagnetic (FDEM) method is a non-invasive geophysical technique that provides continuous spatial information about the subsurface. The FDEM method can provide an effective mechanism to map the salinity of the subsurface formation by measuring the electrical conductivity. The FDEM method has been widely used in groundwater (Fitterman and Deszcz-Pan 1998), agriculture (Minsley et al. 2012), mineral exploration (Farquharson et al. 2013), archaeological prospecting (Bongiovanni et al. 2008) and contaminant studies (Al-Fouaan et al. 2004). FDEM allows a rapid survey (Moghadas and Vrugt 2019), and it is comparatively inexpensive compared to other geophysical methods (Murray et al. 2005). FDEM methods are portable and do not require contact with the ground, which makes the electromagnetic (EM) survey efficient to use. It is possible to record detailed information even in areas where accessibility is a major concern.

The FDEM has a major disadvantage because measurements recorded in different conditions and time may show a static shift. Lavoué et al. (2010) performed three repeated

measurements using EMP 400 at 15 KHz on the same site after a 15-minute interval and showed an offset on the apparent electrical conductivity measurements. Thus, EM methods have a limitation in obtaining absolute electrical conductivity values due to calibration problems (Lavoué et al. 2010). For EM instruments, factory calibration is performed, which is valid for the device defined set up and settings (Tan et al. 2019). For example, the Profiler EMP 400 instrument is calibrated at the GSSI factory by suspending it well above the ground and zeroing the field values. In addition, before data acquisition, field calibration is performed on-site. This field calibration procedure removes any electromagnetic effects of the operator and other equipment in the surrounding area. However, once the measurement set up implemented in different conditions, the calibration is not sufficient anymore (Tan et al. 2019). Hence, calibration of the EM data is required to obtain absolute electrical conductivity values that can relate to the physical properties of the earth.

Electrical resistivity can produce a high-resolution image of the shallow subsurface formation and has been widely used in hydrogeology and environmental studies (Froese et al. 2002). This method has an advantage because resistivity measurements are repeatable (Spragg et al. 2017) and the non-uniqueness of the resistivity method is less and when compared with EM methods. The limitation of electrical resistivity is the number of manpower required to perform the fieldwork and survey time. Hence, an integrated approach of electrical resistivity and EM methods can produce the best result (Lavoué et al. 2010).

Different studies have proposed various approaches to overcome data and calibration errors of EM instruments (Deszcz-Pan et al. 1998; Fitterman and Deszcz-Pan

1998; Abraham et al. 2006; Brodie and Sambridge 2006; Lavoué et al. 2010; Minsley 2012). Deszcz-Pan et al. (1998) calibrated helicopter electromagnetic data based on resistivity-depth information obtained from time-domain sounding and borehole measurements and determined a correction factor before the inversion. Deszcz-Pan et al. 1998 applied amplitude and phase adjustment to find a zero-primary reference level between the receiver (Rx) and transmitter (Tx). A ferrite rod placed parallel to the plane of the coil produces a minor response and changing the orientation of the ferrite rod perpendicular to the plane of the coil produces a negative inphase signal. Besides, a conductor of known dimension, inductance, and a number of turns placed between Rx-Tx produces a specified amplitude deflection on the inphase and quadrature components. Therefore, a phase and gain correction factors are required for adjustment. Another EM calibration study conducted by (Lavoué et al. 2010) implemented a linear regression calibration approach using an electrical conductivity value derived from the electrical resistivity tomography (ERT) model and EM measurements. The authors used the electrical conductivity from the ERT model as input in the electromagnetic forward model that predicts the apparent electrical conductivity measured with EM instrument. Minsley (2012) combined the approach of Deszcz-Pan et al. (1998) and Lavoué et al. (2010) to account for the systematic error in ground applied a calibration procedure by making the FDEM data consistent with the forward response of dc resistivity model in a least-square sense.

This study utilizes coincident EM and ERT surveys on Big Pine Key, FL, to provide calibration and correction to EM survey data. We adopt a similar EM calibration procedure used by Lavoué et al. (2010) and Minsley et al. (2012) and apply a multiple linear

regression model between the observed and calculated models. The inverted vertical electrical sounding (VES) data are used as input to the electromagnetic forward model to estimate the calculated quadrature response. The calculated quadrature from the VES and measured EM data showed a linear correlation, but the measured EM data showed an offset from the calculated quadrature response. This observed offset between the calculated and measured quadrature data is corrected using a multiple linear regression model. Then the general equation obtained was applied to calibrate the EM data of 2.2 Km throughout the profile line. After that, the calibrated quadrature data were converted to apparent electrical conductivity and used to assess the temporal and spatial variation. Finally, the calibrated quadrature data inverted as a 2-layer model using the full solution and the low induction approximation.

This paper aims to improve the previous EM calibration approaches using VES data and investigates the effect of the Hurricane Irma storm surge[3] and recovery history on the freshwater lens along West to East of the profile line of 2.2 Km length. The first section of the paper focuses on the calibration of the EM data using VES measurements and followed by the temporal and spatial variation in conductivity of the subsurface formation with data collected four months (January 2018) and 15 months (December 2018) after Hurricane Irma. Finally, a comparison between the full inversion solution and LIN approximation is presented.

[3] The details of Hurricane Irma are mentioned in Chapter Two in detail.

3.2. Previous Geophysical Surveys

On Big Pine Key, the freshwater lens boundary was mapped based on the contour line of 500 mg/L of chloride concentration from shallow observation wells of 1.5 m depth below the water table (Hanson 1980). In the study, the freshwater lens boundary was considerably wider on the north and tapered toward the south. The author mapped the lateral expansion and contraction of the freshwater lens in response to seasonal recharge. Stewart (1988) conducted an EM survey using Geonics EM-34 and estimated the thickness of the freshwater lens ranging from 4 to 8 m along the profile line. The author developed a 3-layer modeling approach using the low induction approximation and assumed the water table is close to the surface, and the unsaturated and freshwater saturated zones have low bulk conductivities. The author suggested the thickness of the freshwater lens can be obtained as a three-layer solution, where the 1st layer represents the unsaturated zone, and its thickness is assumed to be the elevation of the land above the sea level. The 2nd layer represents the freshwater saturated, and the 3rd layer represents the saltwater saturated of an infinite thickness. Furthermore, this three-layer solution can be reduced to a two-layer solution if the elevation is minimal. The author also suggests the depth of the interface was sensitive to the conductivity of the saltwater used.

Wightman (2010) suggested a 2-layer model is valid in BPK as the conductivities of the first two layers are very similar. The author also suggested EM methods may underestimate the depth of the saltwater interface if a substantial intermediate brackish layer is present. Wightman (1990) delineated the thickness of the freshwater lens and concluded that freshwater lens geometry was dynamic with seasonal variation in precipitation during the dry and wet season in 1987. A similar seasonal variation study

between the dry and wet season in 2009/2010 was not significant due to irregular rainfall patterns before and after the survey periods. The author concluded the highly transmissive Key Largo Limestone controls the depth of the lens.

3.3. Data and Methods of Analysis

3.3.1. Data Collection

A series of EM surveys were conducted using a GSSI Profiler EMP-400 multi-frequency EM conductivity meter integrated with a GPS receiver on Big Pine Key. The EM survey covers 2.2 Km and extended from West to East on the island (Figure 3.1). The instrument was calibrated at the GSSI factory by suspending it well above the ground and zeroing the field values. Before the data acquisition, a field calibration was performed on-site. This field calibration procedure removes any electromagnetic effects of the operator and other equipment in the surrounding area.

The Profiler has a fixed coil spacing of 1.219 m and simultaneously records data at three frequencies in the range of 1 to 16 KHz. In frequency domain EM methods, the data of interest is in the in-phase (real) and out-of-phase (imaginary) components. During the survey, the EM instrument was suspended with the low carry handle 0.10 m above the ground. The EM data were recorded in Vertical and Horizontal dipole orientations using frequencies of 2, 6, and 15 KHz at a 0.2-second interval in January 2018 and 2, 8, and 15 KHz at a 0.5-second interval in May and December 2018. The Vertical dipole has a deeper depth of investigation and used in the analysis. The January 2018 data were collected at a higher sampling rate (0.2 seconds) and then subsampled to 0.5-second. In the analysis, the EM samples that correspond spatially with December 2018 data were used. In January

2018, at 2 KHz frequency, all the recorded inphase values were negative, and at 6 KHz frequency, a few measurements were negative. As a result of this, during data collection, different frequencies were used in May and December 2018 survey. In addition, only the quadrature components were used in the analysis to infer the electrical conductivity of the subsurface. The EM data collected in May 2018 is not used in this study due to poor data quality. Besides, noisy data 250 m long at the center of the profile associated with the power cables interference were removed.

A coincident ERT survey of 220 m long was conducted along the EM transect on the western shoreline of the island in January, May, and December 2018 (Kiflai et al. 2019; Chapter 2). The ERT surveys were collected with an AGI Super Sting R1/IP meter using a 2 m electrode spacing in a roll along Wenner Array configuration. In the roll along survey, the electrodes disconnected in the middle after each measurements and reconnected back in the front. In November 2011, the ERT image showed a gradual change of resistivity (and salinity) with a depth that represents the freshwater lens, brackish transition zone, and saltwater (Figure 3.2b). After Hurricane Irma, the ERT image indicated low resistivity/high salinity zones in the upper 2 m depth corresponding to saline water emplaced on top of the freshwater lens by the storm surge (Figure 3.2c-e). This deposition of saline water on top of the freshwater lens defined by the 3 PSU contour line is observed in the lower elevation sections of the profiles (Kiflai et al. 2019). This low resistivity/ high salinity is clearly visible east of 130 m of profile. For further details, please refer to chapter 2 of this dissertation.

3.3.2. Data Analysis

I. EM Calibration

In a Vertical Electrical Sounding (VES), apparent resistivity measurements are made at a single location by systematically expanding electrode spacings. When the electrode spacing increases, the depth of penetration increases. VES data were extracted from the ERT profile line at seven distinct positions on the transect, 27, 55, 83, 111, 139, 167, and 195 meters from the western end of the profile of January and December 2018 ERT data (Figure 3.3). The data were extracted at 2, 6, 10, 14, and 18 m electrode spacing. These extraction locations were selected to provide the greatest number of data and the maximum effective depth of penetration from each roll along measurements. The VES data extracted from the ERT survey were inverted to 1-D sounding models using IX1DV3 software (http://www.interpex.com/ix1dv3/ix1dv3.htm) and used for EM calibration purposes. The EM calibration approach and modeling technique are illustrated in the flow chart in Figure 3.4.

In this study, the data were inverted using Occam's inversion (Stoyer 2019; Constable et al. 1984) and used four layers over an infinite half-space, and the layer thickness increased progressively from 0.5 to 2 m. The Occam's inversion is a smooth model that depends weekly on the starting value and avoids the problem in the selection of the starting model (Chang-Chun et al. 2019). The Occam's inversion constrained the vertical smoothness and the data fitting and produced a smooth model (Constable et al. 1984) subjected to the constraint used (Stoyer 2019).

The VES model shown in Figure 3.5 is one of the VES examples extracted from the ERT data. In January and December 2018, the VES sounding model showed low resistivity less than 10 Ω·m in the upper 2 m. The resistivity increased with depth to about 50 Ω·m in the middle layer. Then, the resistivity decreased to less than 10 Ω·m at the bottom layer. Generally, the December 2018 VES resistivity is higher than January 2018 VES resistivity. For further details of all the VES sounding models, see the appendix 3A. The Occam's inversion from all the sounding curves has a reasonable fit to the data. We used these VES results to calculate the quadrature response component in the EM forward model and used it for calibration purposes.

The EM quadrature response was calculated from the inverted VES Occam's inversion model. The quadrature response was determined from the VES forward model by considering the spacing (1.21 m), frequencies (2, 6/8, and 15 KHz) and orientation (vertical dipole) of the EM instrument. Then, we compared the calculated quadrature value obtained from the forward model of the VES model with the observed EM data.

In all frequencies, the observed quadrature data was underestimated compared to the calculated quadrature data in January and December 2018 (Figure 3.6). The calculated quadrature values are consistently greater than the dashed line (1:1) and suggested that a shifting factor is required to calibrate the observed quadrature data. In the regression lines, the slope varies from 1.08 to 1.33, and the intercept varies from 75.3 at 2 KHz to 1643 at 15 KHz. In all scatter plots, the observed and calculated quadrature data showed a strong linear correlation, and the regression lines are statistically significant with R^2 value that ranges from 0.78 to 0.90 (Figure 3.6 and Table 3.1). The statistical analysis of the regression lines is summarized in table 3.1.

The observed and calculated quadrature data have a strong positive correlation. The Shapiro-Wilk normality test of the observed quadrature (w= 0.75, p=0.001) and the calculated quadrature (w = 0.88011, p=0.001) suggests the observed and calculated quadrature are not normally distributed. As the data are not normally distributed, a Spearman correlation coefficient was calculated between the observed and calculated quadrature (ρ=0.83, p= 0.001) indicates a strong positive correlation.

The regression lines of January and December 2018, are similar at the same frequencies (Figure 3.6a, 3.6c). The quadrature data increases monotonically with an increase in frequencies, and also, there is a systematic increase in intercept with increasing frequency. In addition, there is a positive linear correlation between the intercept and frequency (R=0.98, p= 0.001) (Figure 3.7a) and a weaker negative correlation (R = -0.64, p = 0.17) between slope and frequency (Figure 3.7b). This linear correlation showed the intercept has a significant correlation with frequency. Hence, we explored a multiple linear regression to examine the influence of frequency and observed quadrature data as the value increases monotonically.

In this study, we used multiple linear regression to predict a general calibration equation using the observed quadrature data and frequency in R software. In the multiple linear regression; we aim at explaining the relationship between the explanatory variables (observed quadrature and frequency) and the response variable (calculated quadrature) by fitting a multiple linear regression. Based on the regression analysis, we developed a calibration equation based on the estimated parameters (Table 3.2), and the generalized equation obtained is:

$$EM_{Calb} = 1.14 * EM_{Obsv} + 0.11 * Freqeuncy - 140.3 \quad (3.1)$$

where EM_{Calb}, EM_{Obsv}, and frequency represent EM calibrated data (ppm), EM observed data (ppm), and frequency (Hz), respectively.

The model accuracy and significance were assessed using Nash-Sutcliffe efficiency (NSE), residual error, and ANOVA statistical analysis. We used the NSE model to evaluate the predictive power of the calibrated model with respect to the calculated data. The NSE indicates how well the plot of observed versus simulated data fits the 1:1 line (Nash and Sutcliffe, 1970). In the NSE model, the R^2 value of 1 indicates a perfect fit between the observed and simulated model and less than or equal to zero indicate a poor fit. The multiple linear regression has a high correlation coefficient (r = 0.93, p= 2.2 ^{-16})), and the calibrated and calculated quadrature data have NSE R^2 value of 0.9396 and indicates that it has a high predictive capability.

The analysis of variance (ANOVA) is a standard statistical technique commonly used to determine the significance of the explanatory variables on the response variable. According to ANOVA statistical analysis, both the observed quadrature data and frequency are highly statically significant (R2= 0.93, p= 2.2 ^ {-16}) (Table 3.3). The values of the F-statistic and Pr (>F) of the EM observed and frequency shows that adding the frequency parameter provided a better model. Consequently, the multiple regressions model appears to be satisfactory for calibrating the data.

The performance of the obtained regression models is assessed using the residuals against fitted values analysis. The residuals vs. fitted values in R is a diagnostic plot, which is useful for assessing the quality whether or not the chosen model equation is appropriate (Baty et al. 2015; Kozak and Piepho 2017). The residual vs. fitted values tell how well the

model fits the data and should be random, normally distributed around a horizontal line. In the residuals vs. fitted values, the red line shows the average trend in residuals (Ekstrøm 2014). In the linear regression, the residuals vs. fitted values analysis (Figure 3.8a), the red line showed a relatively distinct trend in the distribution of points. Whereas, in the multiple linear regression, the red line is relatively flat (Figure 3.8b) and showed an improvement from the linear regression model and suggested a good fit.

We used the calibration equation obtained from the multiple linear regression (equation 3.1) and plotted the EM observed quadrature, VES calculated quadrature, and calibrated quadrature (Figure 3.9). The calibrated quadrature is similar to the calculated quadrature and indicates a high predictive power of the calibration equation, which substantially improves the model. As a result of this, we applied the multiple linear calibration equation for the January and December 2018 EM dataset that extended 2.2 km along the EM profile line.

II. Modeling

Apparent conductivity was calculated using the general equation given by (Keller and Frischknecht 1966; McNeill 1980; equation 1.10) for a homogeneous half-space model for the corrected dataset. The apparent conductivity is directly related to the properties of the subsurface formation. Hence, the calculated apparent conductivity is used to assess the spatial and temporal change between January and December 2018. In addition, this apparent conductivity is used as an input in modeling the EM data using the low induction number approximation.

The calibrated data were modeled as a two-layer using the low induction number (LIN approximation (equation 1.11). During inversion, the resistivity (conductivity) of the

freshwater and saltwater saturated formation were used to constrain the resistivity of the two-layer model. Fixed constraining values were extracted from the November 2011 ERT data using the contour line of 3 PSU as a sharp interface indicator. The average conductivity of the freshwater (less than 3 PSU) and saltwater (greater than 3 PSU) were extracted to correspond freshwater and saltwater saturated formation (Figure 3.2b). An average resistivity (conductivity) value of 40 Ω·m (25 mS/m) and 6 Ω·m (166.6 mS/m) were extracted that represents the freshwater and saltwater saturated formations. The November 2011 ERT data was used as it is a simple model and represents the freshwater lens geometry before Hurricane Irma disturbance. Stewart (1988), adjusted the interface depth by varying the conductivity of the saltwater saturated formation from the VES solution until the thickness of the EM data matches with VES solution and water quality data.

In the LIN approximation, we adopted a similar assumption made by Stewart (1988) for a horizontal dipole. In this study, we applied a similar approach for a 2-layer vertical dipole. We estimated the depth of the interface using the LIN approximation as a 2-layer model. For a 2-layer model of conductivities σ_1 and σ_2 and dimensionless depths (z) (the ratio of depth to coil spacing), the apparent conductivity (σ_a) is:

$$\sigma_a = \sigma_1[1 - R(z)] + \sigma_2 R(z) \tag{3.2}$$

where R is the cumulative response function for each layer,

$$R(z) = \frac{1}{\sqrt{4z^2 + 1}} \tag{3.3}$$

(Mc Neill, 1980). Solving equation (2) for $R(z)$.

$$\sigma_a - \sigma_1(1) = \sigma_1 R(z) + \sigma_2 R(\mathrm{z}) \tag{3.4}$$

$$R(z) = \frac{\sigma_2 - \sigma_1}{\sigma_a - \sigma_1} \tag{3.5}$$

We know $R(z) = 1/\sqrt{4z^2 + 1}$,

$$\frac{\sigma_2 - \sigma_1}{\sigma_a - \sigma_1} = 1/\sqrt{4z^2 + 1} \tag{3.6}$$

Substituting, squaring and rearranging both sides

$$\mathrm{z} = \frac{1}{2}\sqrt{\left(\frac{\sigma_2 - \sigma_1}{\sigma_a - \sigma_1}\right)^2 - 1}\,, \tag{3.7}$$

where Z is the depth below land surface to the interface.

The induction number (D) is the ratio of the coil spacing (s) to skin depth(δ) = $1/\sqrt{\pi\mu_0\sigma f}$. This approximation is valid when the conductivities are sufficiently low that the operational constraints of the induction number (D<<1) are respected (McNeill 1980). McNeill (1980) recommends the LIN approximation should be used where $\sigma \leq 100$ mS/m. We summarized in Table 3.4, the induction number (D) of the EMP 400 profiler on a range of conductivity (resistivity) values. The LIN approximation is more reasonable in the lower frequency range (2 KHz). However, the low-frequency range of the EMP 400 profiler is sensitive to noise. Hence, we used the data at 6 KHz and 8 KHz for the LIN approximation and compared it with the full solution inversion.

The calibrated data were inverted in IX1D V3 as a 2-layer model using the full solution (equation 1.14). In the full solution, the inphase value in some measurements was negative and exceptionally higher than the quadrature value at 15 KHz in January 2018. Hence, in the full solution inversion, the inphase values were masked and the data were inverted using the quadrature component. Due to the inherent non-unique model and highly dependent on the starting initial model, the models were incapable of resolving the layers.

As a result of this, the resistivity of the freshwater and saltwater were fixed using the data extracted from the ERT image ($\rho_1 = 40$ Ω·m and $\rho_2 = 6$ Ω·m) and the models were inverted only to estimate the interface depth.

3.4. Results

3.4.1. Seasonal Change in Apparent Conductivity

The EM data showed a temporal and spatial variation in apparent conductivity between January to December 2018. On average, the apparent conductivity decreased between January to December 2018 by 27 mS/m and 20 mS/m at 2 KHz and 15 KHz, respectively. In the profile line from West to East, a significant decrease greater than 30 mS/m occurred between 200-250 m, 450-500 m, 550-600m, 675- 725 m, 1300- 1550 m, and 1700-1900 m at 2 and 15 KHz (Figure 3.10b, 3.10c). These changes are most pronounced in the lower elevation regions, less than 1 m elevations. In contrast, the apparent conductivity change was not significant, where the elevation is higher than 1 m. The apparent conductivity change was minimal along the Western and Eastern margin of the island (Figure 3.10b, 3.10c).

3.4.2. EM Inverted Models

The calibrated EM data was inverted as a 2-layer model using the LIN approximation and full solution by constraining the conductivity of the layers. Both results showed a consistent estimate of the freshwater and saltwater interface throughout the profile line (Figure 3.11a and 3.11b). In January 2018, the depth of the interface was estimated on average at a depth of 2.5 m from the land surface and became thinner towards the margins of the island (Figure 3.11a). The shallow estimated interface depth corresponds to the lower

elevation region and clearly visible at around 500 m, 1440 m-1500 m, and 1800 m and occurred when the apparent conductivities are greater than 70 mS/m. Despite the consistent estimate of the freshwater and saltwater interface, the LIN produces shallower interface depths than the full solution at certain localities, when the apparent conductivities are greater than 150 mS/m. The LIN approximation is less applicable when the apparent conductivities are greater than 100 mS/m In contrast, in the full solution below 5 m depth, specific models have poor goodness of fit and showed a sharp spike in the interface.

In December 2018, the interface depth was estimated on average at a depth of 3.5 m from the land surface (Figure 3.11b). Similar to January 2018, the shallow interface depth observed at around 500 m, 1400-1500 m, and 1800 m and corresponds to low elevation regions. The LIN approximation estimated deeper interface depth compared to the full solution throughout the profile line. Besides, in the LIN approximation, there are many notable spikes and deviated from the full solution.

Between December to January 2018, the seasonal change in the thickness of the freshwater lens increased on average by 1 m and is most pronounced on the lower elevation regions (Figure 3.12). Most of the change observed between 100 m – 300 m, 400 m – 600 m, 700 m- 800 m, and 1200 m – 1900m. However, the shape of the interface remains the same in December and January 2018. The interface depth variation was minimal along the Western and Eastern margin of the island.

3.5. Discussion

The linear regression trend between the observed and calibrated data is a promising calibration approach. A strong linear correlation noticed between the observed and

calculated quadrature data with R^2 value that ranges between 0.74 to 0.93. The spearman correlation coefficient confirmed the strong positive correlation between the observed and calculated quadrature. In all frequencies, the observed quadrature data was underestimated compared to the calculated quadrature data (Figure 3.6) and suggested a correction factor is required to calibrate the observed quadrature data.

The derived multiple linear equations gave a good agreement between the calculated and calibrated data. In the multiple linear regression, according to the ANOVA statistical analysis, both the observed quadrature data and frequencies are statistically significant (R^2 = 0.93, p= 2.2 ^ {-16}) (Table 3.3). The performance of the multiple linear equations assessed using the Nash-Sutcliffe efficiency (NSE) and the R^2 value 0.93, indicated the accuracy of the predictive power of the multiple linear equations. Moreover, in the residual vs. fitted value analysis, the multiple linear regression model showed an improvement from linear regression (Figure 3.8). As a result of this, the derived multiple linear regression equation was applied for the dataset that extended to 2.2 Km profile line. Minsley (2012) observed that the calibration parameters may drift over time and suggested re-assessment of the system calibration throughout the profile line. Based on the results from this study, VES at pilot locations can be used for calibration purposes and verification of the accuracy of EM measurements.

In January 2018, the VES showed the deposition of saline water (high conductivity/low resistivity) on top of the freshwater lens (Figure 3.5a). Most of the VES models are a typical example of K types electrical resistivity curve, where the resistivity rises to a maximum and then decreases. This curve demonstrates that the intermediate layer has a higher

resistivity than the top and bottom layers (i.e., R1<R2>R3) (Figure 3.5a). The low resistivity in the upper 2 m depth suggests the deposition of saline water on top of the freshwater lens. In December 2018, the VES showed a decrease of salinity in the top 2 m. The VES has a K types electrical resistivity curve and inclination towards Q type electrical resistivity curve layers (i.e., R1>R2>R3) (Figure 3.5b). The inclination towards the Q type indicates the resistivity in the upper 2 m depth increased compared to January 2018 sounding curves and suggested the recovery of the freshwater lens.

The EM apparent conductivity change between January to December 2018 showed a significant decrease in conductivity and most pronounced in the lower elevations region of the profile line (Figure 3.10). The apparent conductivity decreased between 200 to 250 m, 450 to 500 m, 550 to 600m, 675 to 725, 1300 to 1550, and 1700 to 1900 m. These changes are most pronounced in the lower elevation region of the profile line (Figure 3.10). This change after a year revealed the recovery of the freshwater lens due to intense precipitation and related to the cumulative rainfall recorded in 2018 and especially to the large precipitation event recorded in May 2018 (Figure 2.6). This result suggests the impact on the freshwater lens and recovery is influenced by topography. The apparent conductivity change was minimal along the Western and Eastern margin of the island and indicated the region was saline pre and post-storm condition. Furthermore, the apparent conductivity change was minimal in the higher elevation regions and may suggest the area is not yet recovered fully from the impact of the storm.

The LIN approximation and full solution showed a consistent estimate of the freshwater and saltwater interface throughout the profile line (Figure 3.11). In general, the freshwater lens depth estimated at 2.5 m in January 2018 and 3.5 m in December 2018 from the land

surface. This result suggests the freshwater lens recovery. The full solution and the LIN approximation gives a consistent result throughout the profile line. Generally, the LIN estimated shallow depth compared to the full solution, and the full solution has spikes at certain localities when the model has poor goodness of fit. Even though both the models are similar, the LIN approximation depends on several assumptions. Hence, we select the full solution to compare the seasonal change.

Between January to December 2018, on average, the interface depth increased by 1 m. This recovery in the thickness of the aquifer occurred mostly in the lower topographic relief between higher elevation regions (Figure 3.12). Slope plays an important role and caused the drainage accumulated in the low topographic relief. The collected water in the low relief features potentially has higher residence time and an opportunity to infiltrate to the ground. As a result of this, the infiltration rate increases in low relief features. Khan et al. (2016) suggested a micro-relief increased the surface area for infiltration and resulted in an increase in the infiltration rate. The infiltration rate generally depends on geomorphology, soil hydraulic properties, rainfall, and evapotranspiration. This result indicates the contribution of slope in the recovery of the low relief features.

The LIN approximation and full solution underestimated the depth of the interface in the low elevation regions, where the conductivity was high. The high conductivity value on this region represents the deposition of the saline water on top of the freshwater (Kiflai et al. 2019; Ross et al. 2019). Wightman (2010) suggested the EM methods may underestimate the depth of the interface if a substantial brackish layer is present. The ERT result (Chapter 2) along the profile line B1 and B2 indicated a substantial brackish layer.

Therefore, the results obtained using the LIN approximation and the full solution is a simplified hydrological condition.

The temporal and spatial resistivity variation on BPK demonstrated from the ERT result (Chapter 2), and the VES result (Figure 3.5) showed the complex hydrological condition. In addition, the short coil spacing (1.219 m) of the EMP 400 profiler may have a limitation to capture in-depth information of the subsurface formation. Besides, the interface depth compared using 6 KHz and 8 KHz may have different penetration depths. Therefore, the 2-layer results obtained using the LIN approximation and the full solution is a simplified result and may not represent in detail the current condition of the aquifer. Some limitations of this study could be, the VES was assumed as an exact model, even though there is an error associated during measurement and inversion. The error in the VES data could mislead the calibration approach and result. Secondly, the subsurface formation lateral variation was assumed a homogenous and may underfit or overfit the models.

3.6. Conclusions

In this study, we used VES, and EM data collected four months (January 2018) and 15 months (December 2018) after Hurricane Irma to assess the impact of the storm surge and recovery history of the freshwater lens and investigated a calibration of EMI conductivities based on VES measurements. During calibration, the inverted VES data were used as input in the electromagnetic forward model to estimate the quadrature response component. Then, the observed offset between the calculated and measured quadrature data was corrected using a multiple linear regression model. The derived multiple linear models gave a good agreement between the calculated and calibrated data and indicated a promising

calibration approach. Thus, VES at pilot locations can be used to calibrate and verify the accuracy of FDEM measurements.

In January 2018, the VES showed the low resistivity (high conductivity) on the upper 2 m depth and suggested the deposition of saline water on top of the freshwater lens. The apparent conductivity change, between January to December 2018, showed a significant decrease in conductivity and, most pronounced in the lower elevations region, suggest the recovery of the freshwater lens. The LIN approximation and full solution showed a consistent estimate of the freshwater and saltwater interface and estimated at 2.5 m in January 2018 and 3.5 m in December 2018 from the land surface. Therefore, both the impact of the storm surge and recovery due to precipitation is most pronounced in the lower elevations portion of the island, and the rate of recovery increased most in the low relief features.

3.7. References

AGIUSA. (2019). SuperStingTM Wi-Fi. Agiusa.com. https://www.agiusa.com/supersting-wifi

Abraham, Jared D., Maria Deszcz-Pan, David V. Fitterman, and Bethany L. Burton. 2006. Use of a Handheld Broadband EM Induction System for Deriving Resistivity Depth Images. Symposium on the Application of Geophysics to Engineering and Environmental Problems 2006. https://doi.org/10.4133/1.2923642.

Al-Fouzan, Fouzan, William Harbert, Robert Dilmore, Richard Hammack, James Sams, Garret Veloski, and Terry Ackman. 2004. Methods for Removing Signal Noise from Helicopter Electromagnetic Survey Data. Mine Water and the Environment. https://doi.org/10.1007/s 10230-004-0033-3.

Baty, F., Ritz, C., Charles, S., Brutsche, M., Flandrois, J. P., and Delignette-Muller, M. L. (2015). A toolbox for nonlinear regression in R: the package nlstools. *Journal of Statistical Software*, *66*(5), 1-21.

Binley, A. (2019a). R2 (Version 3.3). {Lancaster University Faculty of Science Technology}. http://www.es.lancs.ac.uk/people/amb/Freeware/R2/R2.htm

Bongiovanni, M., Bonomo, N., de la Vega, M., Martino, L. and Osella, A.,2008. Rapid evaluation of multifrequency EMI data to characterize buried structures at a historical Jesuit Mission in Argentina, *J.appl. Geophys.*,64(1–2), 37–46.

Brodie, Ross, and Malcolm Sambridge. 2006. A Holistic Approach to Inversion of Frequency-Domain Airborne EM Data. GEOPHYSICS. https://doi.org/10.1190/1.2356112.

Chang-Chun, Y., Xiu-Yan, R., Yun-He, L., Yan-Fu, Q., Chang-Kai, Q., and Jing, C. (2015). Review on airborne electromagnetic inverse theory and applications. *Geophysics, 80*(4), W17-W31.

Childers, Daniel L., Evelyn Gaiser, and Laura A. Ogden. 2019. The Coastal Everglades: The Dynamics of Social-Ecological Transformation in the South Florida Landscape. Oxford University Press.

Constable, S. C., Parker, R. L., and Constable, C. G. (1987). Occam's inversion: A practical algorithm for generating smooth models from electromagnetic sounding data. *Geophysics,* 52(3), 289–300.

Ekstrøm, C. T. (2014). Teaching instant experience with graphical model validation techniques. *Teaching Statistics, 36*(1), 23-26.

Farquharson, C. G. 2000. Background for Program 'EM1DFM.' University of British Columbia Geophysical Inversion Facility, Vancouver, British Columbia, Canada, 20p.

Fitterman, David V. 1998. Sources of Calibration Errors in Helicopter EM Data. Exploration Geophysics. https://doi.org/10.1071/eg998065.

Fitterman, D. V., and Deszcz-Pan, M. (1998). Helicopter EM mapping of saltwater intrusion in Everglades National Park, Florida. Exploration Geophysics, 29(2), 240–243.

GSSI. (n.d.). Profiler EMP-400. Geophysical.com. Retrieved July 30, 2019, from https://www.-geophysical.com/products/profiler-emp-400

Hanson, C. E. (1980). Freshwater resources of Big Pine Key, Florida (No. 80-447). U.S. Geological Survey,. https://doi.org/10.3133/ofr80447

Inman, J. R., 1975, Resistivity inversion with ridge regression: Geophysics, 40, pp. 798-817.

Keller, G. V., and Frischknecht, F. C. (1966). Electrical methods in geophysical prospecting, by G.V.Keller and F.C. Frischknecht. Oxford, New York, Pergamon Press.

Khan, M. N., Gong, Y., Hu, T., Lal, R., Zheng, J., Justine, M. F., ... and Zhang, H. (2016). Effect of slope, rainfall intensity and mulch on erosion and infiltration under simulated rain on purple soil of south-western Sichuan province, China. Water, 8(11), 528.

Kiflai, Michael Eyob, Dean Whitman, Danielle E. Ogurcak, and Michael Ross. 2019. The Effect of Hurricane Irma Storm Surge on the Freshwater Lens in Big Pine Key, Florida Using Electrical Resistivity Tomography. Estuaries and Coasts. https://doi.org/10.1007/s12237-019-00666-3.

Kozak, M., and Piepho, H. P. (2018). What's normal anyway? Residual plots are more telling than significance tests when checking ANOVA assumptions. Journal of Agronomy and Crop Science, 204(1), 86-98.

LaBrecque, D. J., and Yang, X. (2001). Difference Inversion of ERT Data: a Fast Inversion Method for 3-D In Situ Monitoring. Journal of Environmental and Engineering Geophysics, 6(2), 83–89.

Lavoué, F., van der Krak, J., Rings, J., André, F., Moghadas, D., Huisman, J. A., Lambot, S., Weiherrnüller, L., Vanderborght, J., and Vereecken, H. (2010). Electromagnetic induction calibration using apparent electrical conductivity modelling based on electrical resistivity tomography. Near Surface Geophysics, 8(6), 553–561.

McNeill, J. D. (1980). Electromagnetic Terrain Conductivity Measurement at Low Induction Numbers. http://www.geonics.com/pdfs/technicalnotes/tn6.pdf

Minsley, Burke J., Bruce D. Smith, Richard Hammack, James I. Sams, and Garret Veloski. 2012. Calibration and Filtering Strategies for Frequency Domain Electromagnetic Data. Symposium on the Application of Geophysics to Engineering and Environmental Problems 2010. https://doi.org/10.4133/1.3445431.

Moghadas, D., and Vrugt, J. A. (2019). The Influence of Geostatistical Prior Modeling on the Solution of DCT-Based Bayesian Inversion: A Case Study from Chicken Creek Catchment. In Remote Sensing (Vol. 11, Issue 13, p. 1549). https://doi.org/10.3390/rs 11131549

Murray, C. J., Last, G. V., and Truex, M. J. (2005). Review of Geophysical Techniques to Define the Spatial Distribution of Subsurface Properties or Contaminants. Contract , August, 1–40.

NOAA.(2020). Tides and Currents Datum. Retrieved 22 March 2020, from https://tidesandcurrents/noaa.gov/datums.html?id=8723970&name=Vaca%20Key, %20 Florida%20Bay&state=FL

Ogurcak, D. E. (2015). The Effect of Disturbance and Freshwater Availability on Lower Florida Keys Coastal Forest Dynamics [Florida International Univeristy]. https://doi.org/10.25148/etd.-FIDC000187

Oldenburg, D. W., and F. H. M. Jones. 2011. EM1DFM (Inversion for Applied Geophysics): University of British Columbia Geophysical Inversion Facility.

Ross, M. S., Ogurcak, D. E., Stoffella, S., Sah, J. P., Hernandez, J., & Willoughby, H. E. (2019). Hurricanes, storm surge, and Pine forest decline on a low limestone Island. Estuaries and Coasts, 1-13.

Spragg, R., Villani, C., Snyder, K., Bentz, D., Bullard, J. W., & Weiss, J. (2013). Factors that influence electrical resistivity measurements in cementitious systems. Transportation research record, 2342(1), 90-98.

Stewart, M. (1988). Electromagnetic Mapping of Fresh-Water Lenses on Small Oceanic Islands. Ground Water, 26(2), 187–191.

Stoyer, C. (2019). IX1D Resistivity, IP, EM Software (Version 3) [Computer software]. http://www.interpex.com/ix1dv3/ix1dv3.htm

Stoyer, C. H. (2010, January). Equivalence analysis of DC and EM data for layered models using the resolution matrix. In Symposium on the Application of Geophysics to Engineering and Environmental Problems 2010 (pp. 173-182). Society of Exploration Geophysicists.

Tan, X., Mester, A., von Hebel, C., Zimmermann, E., Vereecken, H., van Waasen, S., and van der Kruk, J. (2019). Simultaneous calibration and inversion algorithm for multiconfiguration electromagnetic induction data acquired at multiple elevations Calibration inversion for rigid-boom EMI. Geophysics, 84(1), EN1-EN14.

Tucker, N. M. (2013). Analyzing tidal fluctuations in the Big Pine Key freshwater lens with time-lapse resistivity [Florida International Univeristy]. https://doi.org/10.25148 /etd.FI13080512

Wightman, M. J. (1990). Geophysical analysis and Dupuit-Ghyben-Herzberg modeling of freshwater lenses on Big Pine Key, Florida (S. Kruse (Ed.)) [M.S Thesis]. University of South Florida.

Wightman, M. J. 2010. Geophysical and hydrogeological study of freshwater lenses on Big Pine Key, FL. 1423. GeoView, Inc.

Table 3. 1: Statistical analysis of the linear regression model of the EM observed and calculated data

	Estimate	Std. Error	RSE	R Square	F Statistic	DF	T value	Pr(>|t|)[1]4	
(Intercept)	129	50.5	57.6	0.87	34.57	5	2.56	0.05096	.
Slope Dec 2 KHz	1.2	0.2					5.88	0.00202	**
(Intercept)	75.3	100	100	0.79	19.43	5	0.75	0.48678	
Slope Jan 2 KHz	1.33	0.3					4.41	0.00697	**
(Intercept)	580	135	177	0.9	47.81	5	4.31	0.00768	**
Slope Dec 8 KHz	1.27	0.18					6.92	0.00097	***
(Intercept)	289	264	270	0.79	18.69	5	1.09	0.32385	
Slope Jan 6 KHz	1.21	0.28					4.32	0.00755	**
(Intercept)	1348	220	350	0.88	36.71	5	6.13	0.00168	**
Slope Dec 15 KHz	1.21	0.2					6.06	0.00177	**
(Intercept)	1643	406	604	0.78	18.48	5	4.05	0.00982	**
Slope Jan 15 KHz	1.08	0.25					4.3	0.00772	**

Notes: DF= Degree of freedom, and RSE= residual standard error.

[4] Signif. codes: 0 ‘***’ 0.001 ‘**’ 0.01 ‘*’ 0.05 ‘.’ 0.1 ‘ ’ 1

Table 3.2: Statistical parameters of the multiple linear regression

```
Call:
lm(formula = EM-Calculated ~ EM-Observed + Frequency)

Residuals:
```

Min	1Q	Median	3Q	Max
-892.79	-80.81	28.12	-113.42	840.83

Coefficients:

Source	Estimate	Std. Error	t value	Pr(>|t|)
(Intercept)	-140.3	84.06	1.669	0.103
EM-Observed	1.140	0.08444	13.498	2.79e-16 ***
Frequency	0.1065	0.009902	10.754	3.14e-13 ***

```
---
Signif.codes: 0 '***' 0.001 '**' 0.01 '*' 0.05 '.' 0.1 ' ' 1

Residual standard error: 296.3 on 39 degrees of freedom

Multiple R-squared:  0.9397, Adjusted R-squared:  0.9367

F-statistic: 304.1 on 2 and 39 DF, p-value: < 2.2e-16
```

Table 3. 3: Analysis of Variance Table

Source	Degrees of Freedom	Sum of Squares	Mean Square	F Ratio	Pr(>F) [5]
EM Observed	1	43255448	43255448	492.58	< 2.2e-16 ***
Frequency	1	10155550	10155550	115.65	3.139e-13 ***
Residuals	39	3424769	87815		

[5] Signif. codes: 0 '***' 0.001 '**' 0.01 '*' 0.05 '.' 0.1 ' ' 1

Table 3.4: A table of induction numbers, D for frequencies between 1 and 16 KHz for EMP 400 Profiler. The shaded rows represent the frequencies used during the EM survey

Resistivity (Ωm)	**100**	**10**	**1**	**0.5**
Conductivity (mS/m)	**10**	**100**	**1000**	**2000**
F (KHz)	D	D	D	D
1	0.008	0.024	0.076	0.108
2	**0.011**	**0.034**	**0.108**	**0.152**
3	0.013	0.042	0.132	0.186
4	0.015	0.048	0.152	0.215
5	0.017	0.054	0.170	0.241
6	**0.019**	**0.059**	**0.186**	**0.264**
7	0.020	0.064	0.201	0.285
8	**0.022**	**0.068**	**0.215**	**0.304**
9	0.023	0.072	0.228	0.323
10	0.024	0.076	0.241	0.340
11	0.025	0.080	0.252	0.357
12	0.026	0.083	0.264	0.373
13	0.027	0.087	0.274	0.388
14	0.028	0.090	0.285	0.403
15	**0.029**	**0.093**	**0.295**	**0.417**
16	0.030	0.096	0.304	0.430

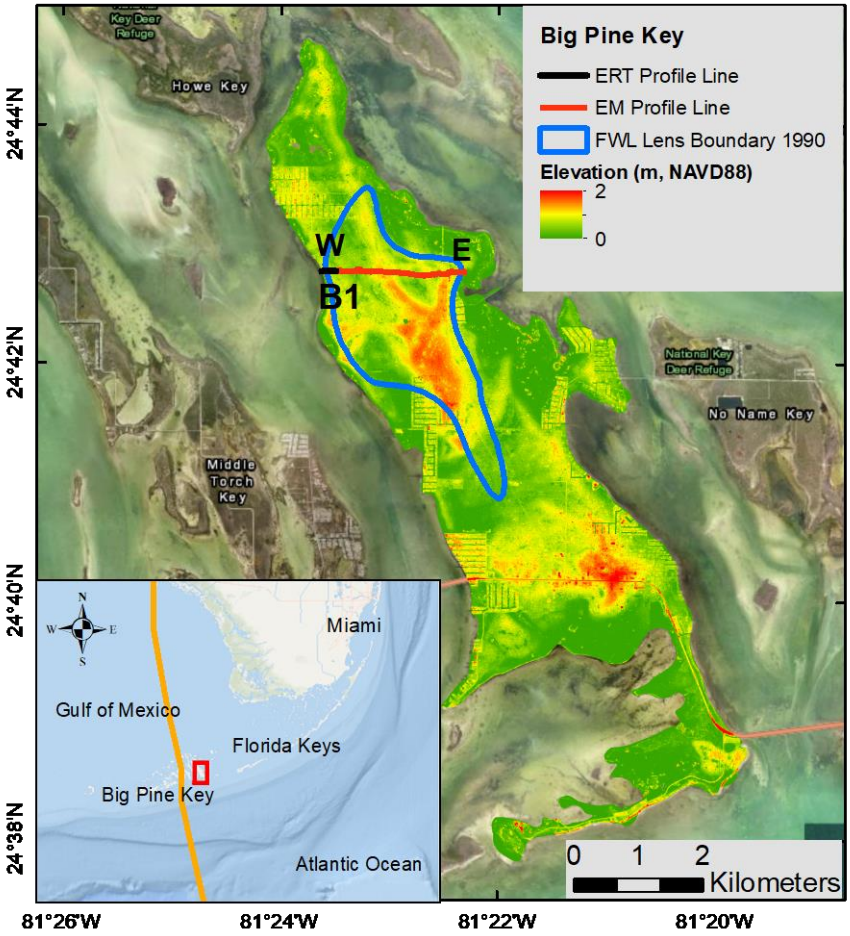

Figure 3.1: Topographic map of Big Pine Key showing the location of the boundary of the freshwater lens (Wightman, 1990), EM, and ERT profile line. Inset map shows the track of Hurricane Irma

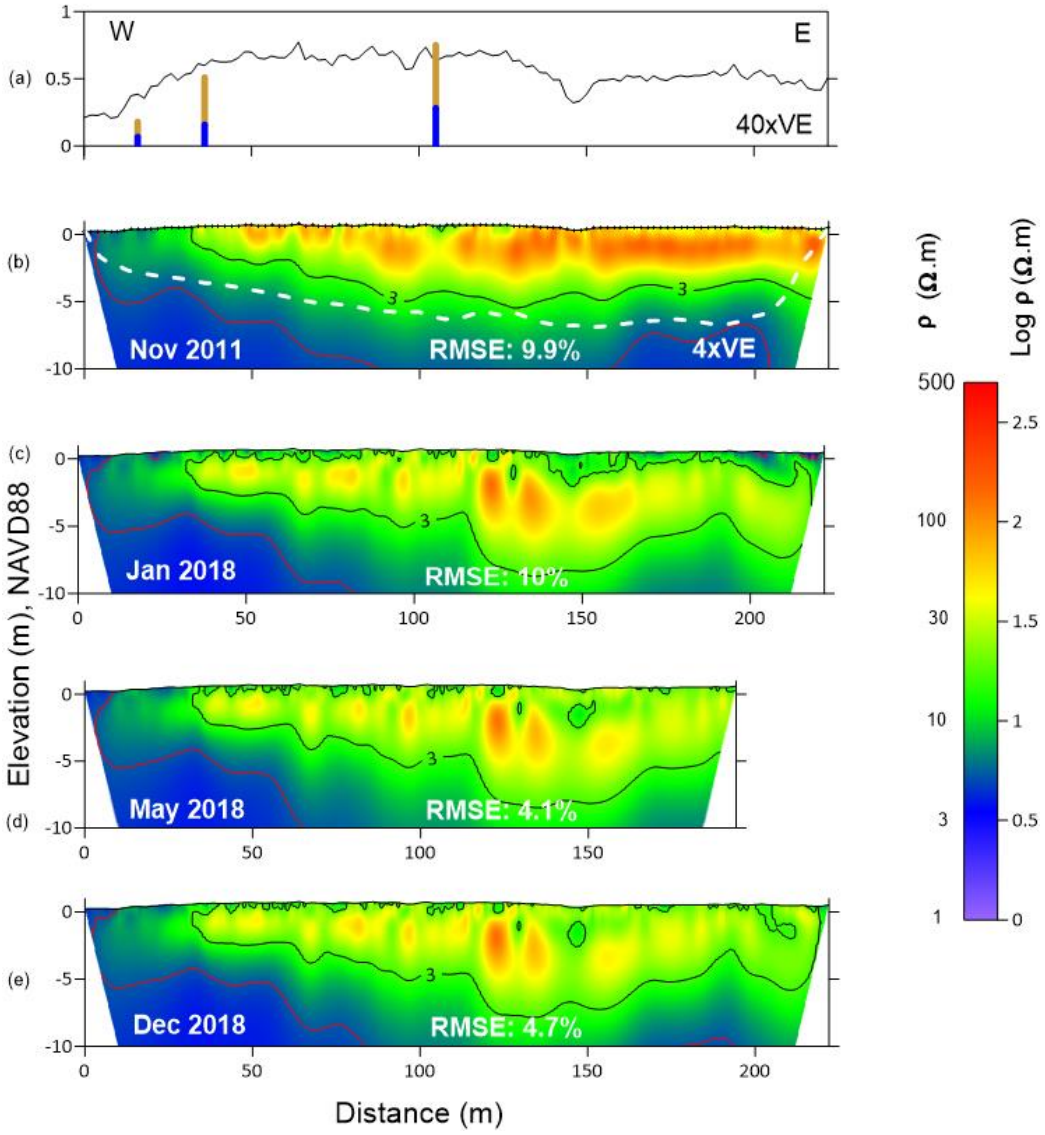

Figure 3.2: ERT resistivity models on profile B1. a. Topography. The gold and blue lines indicate the unsaturated and saturated zone in the wells; b. November 2011; c. January 2018; d. May 2018; e. December 2018. The black and red contour line represents a salinity of 3 and 10 PSU. The 0.2 DOI index is shown as a dashed line. The location of the profiles is shown in Figure 2.2. Elevations are relative to NAVD88.

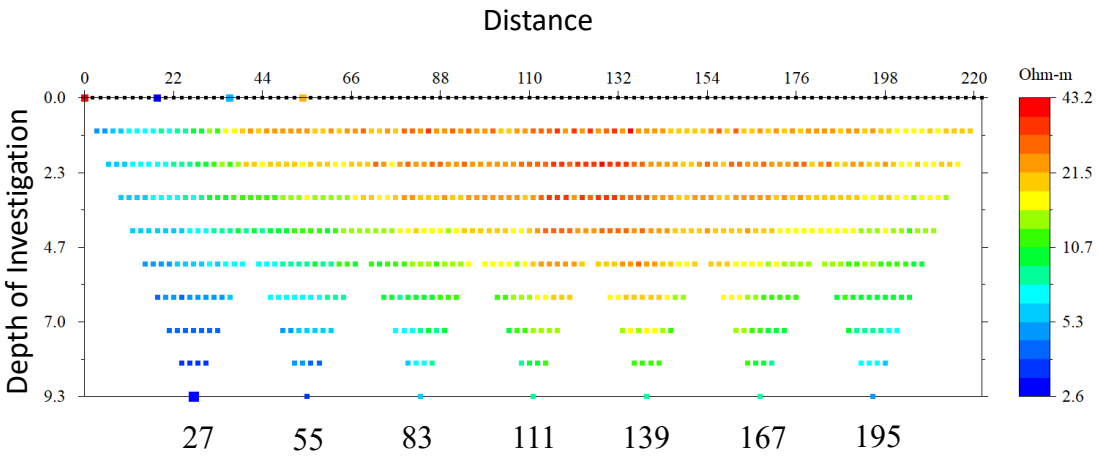

Figure 3.3: Measured Apparent Resistivity Pseudosection with an electrode spacing of 2 m. The VES sounding was extracted at 27, 55, 83, 111, 139, 167, and 195 m at electrode spacing of 2, 6, 10, 14 and 18 m

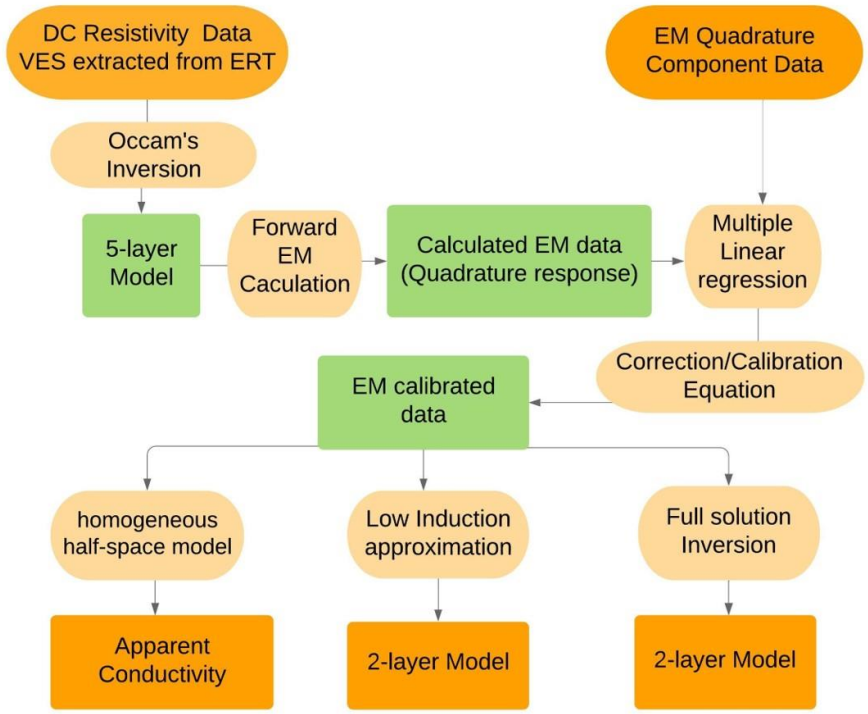

Figure 3.4: Flow chart of EM data calibration using VES data, modeling and interpretation approach

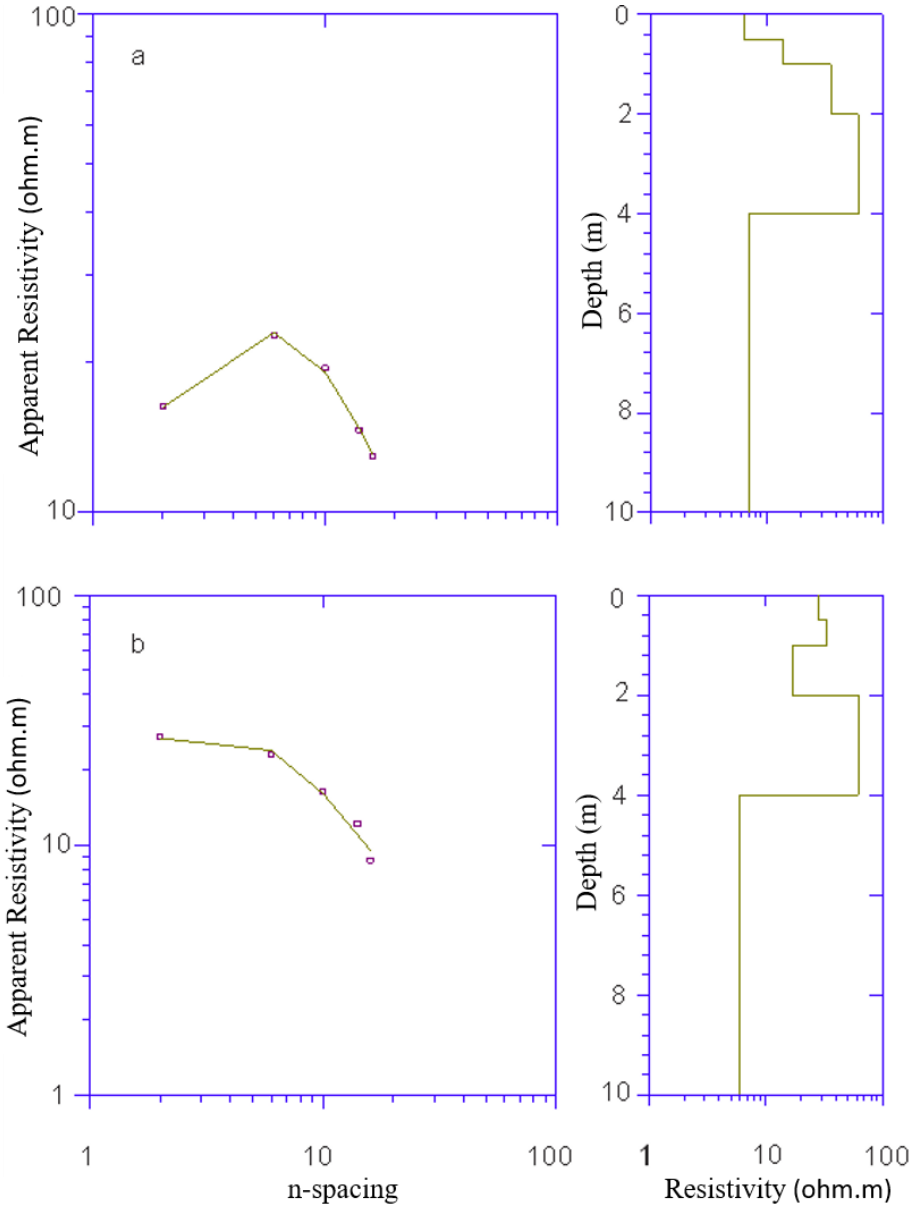

Figure 3.5: Vertical Sounding Curve along the profile line B1 at 195 m from the ERT starting point in figure 3.3 (a) January 2018: The Occam's Inverted model has a characteristic of K-Type curves. (b) December 2018: The Occam's Inverted model inclines Q-Type.

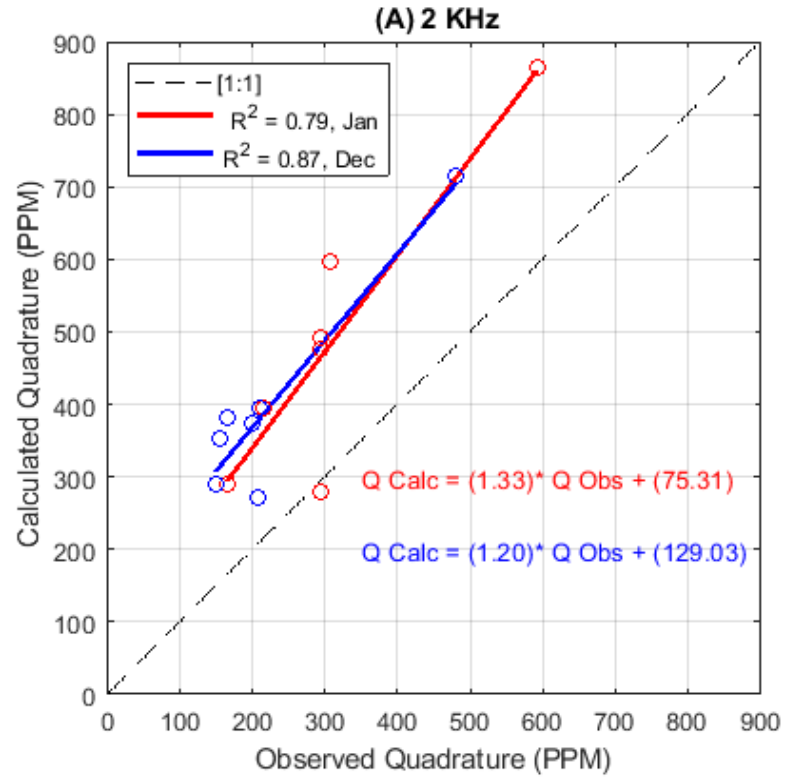
(A) 2 KHz
[1:1]
R2 = 0.79, Jan
R2 = 0.87, Dec
Q Calc = (1.33)* Q Obs + (75.31)
Q Calc = (1.20)* Q Obs + (129.03)
Calculated Quadrature (PPM)
Observed Quadrature (PPM)
0
100
200
300
400
500
600
700
800
900

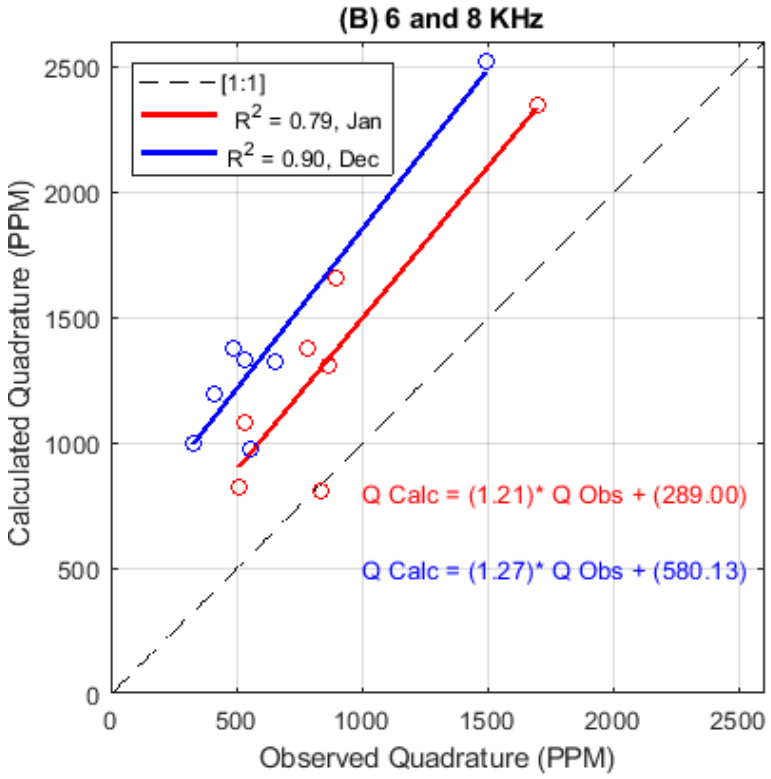
(B) 6 and 8 KHz
[1:1]
R2 = 0.79, Jan
R2 = 0.90, Dec
Q Calc = (1.21)* Q Obs + (289.00)
Q Calc = (1.27)* Q Obs + (580.13)
Calculated Quadrature (PPM)
Observed Quadrature (PPM)
0
500
1000
1500
2000
2500

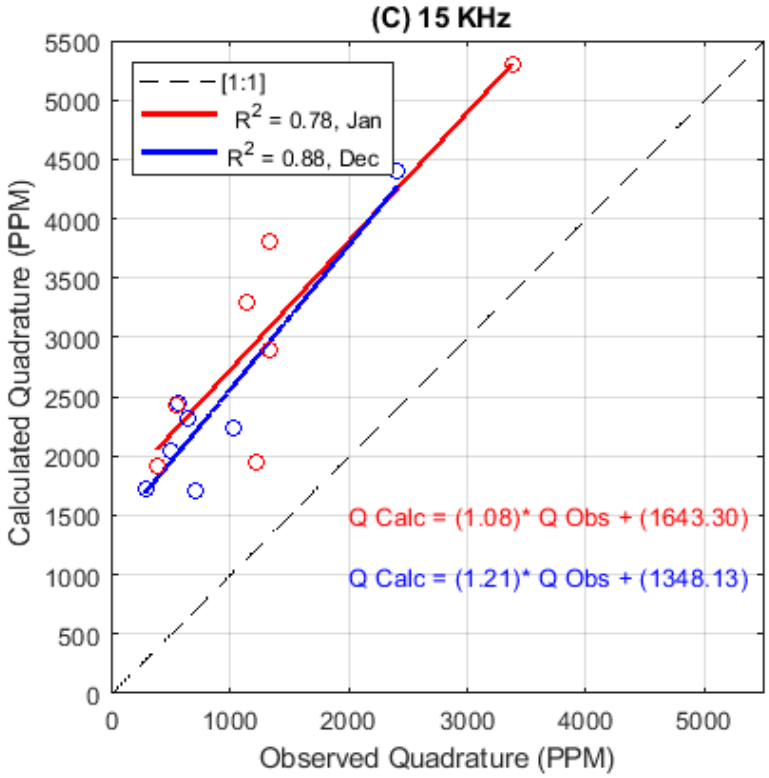

Figure 3.6: Linear regression model between observed and calculated quadrature. The red and blue regression line represents January 2018 and December 2018 data at (a) 2 KHz, (b) 6 and 8 KHz, and (c) 15 KHz.

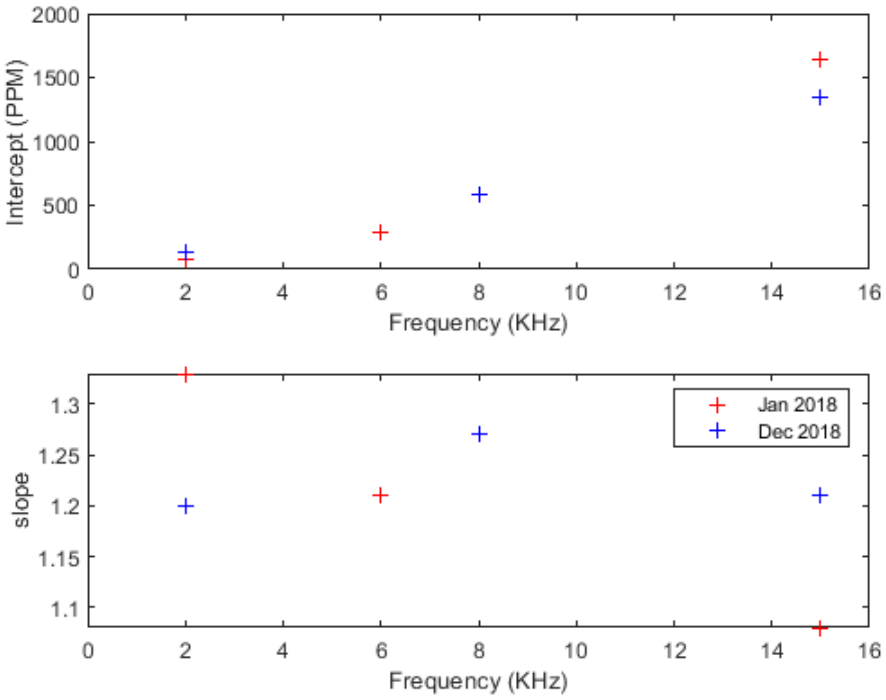

Figure 3.7: Relationship of slope and intercept of January and December 2018 regression lines with frequency.

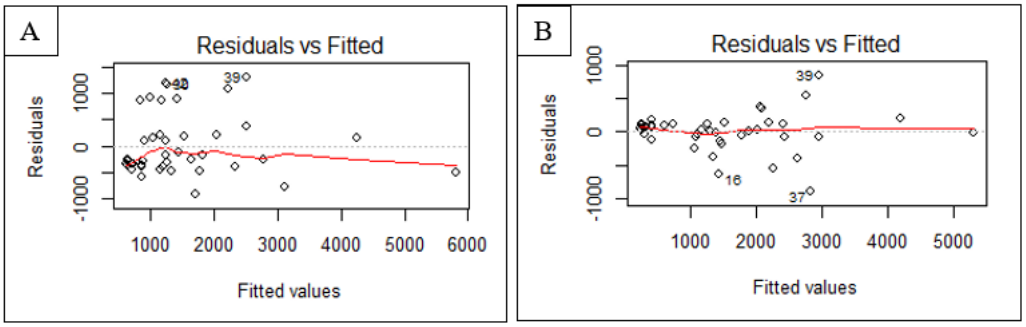

Figure 3.8: Plot of residual vs. fitted value (A) linear regression (B) multiple linear regression. On the x-axis are observed quadrature and on the y-axis are the model residual.

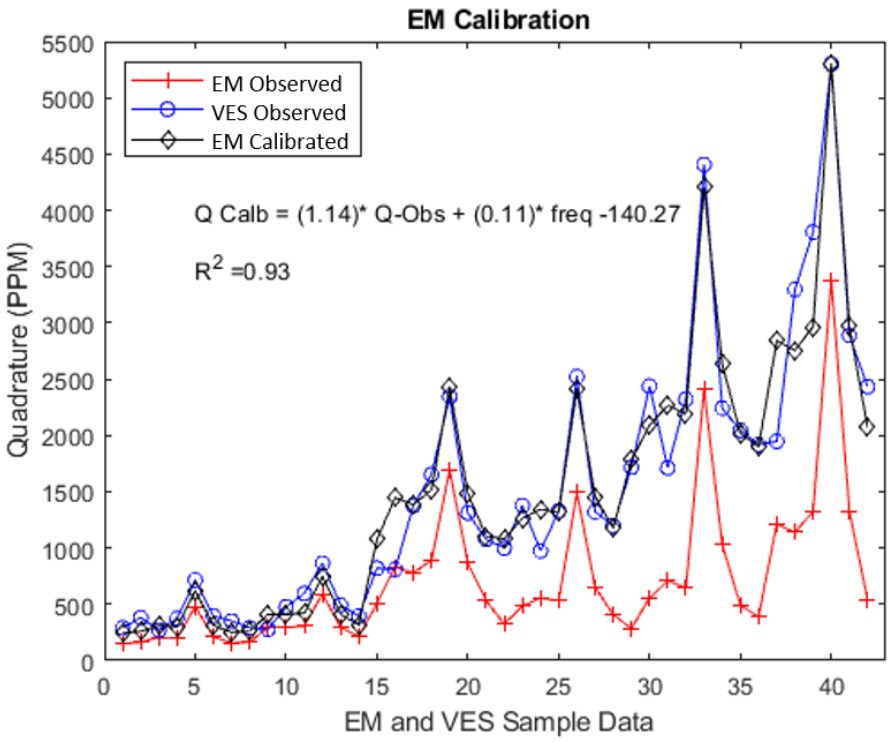

Figure 3.9: Multiple Linear regression prediction power. The EM observed were measured using the EMP 400 Profiler, the VES observed were calculated from the VES forward model, and the EM Calibrated were calculated using the multiple linear regression equation

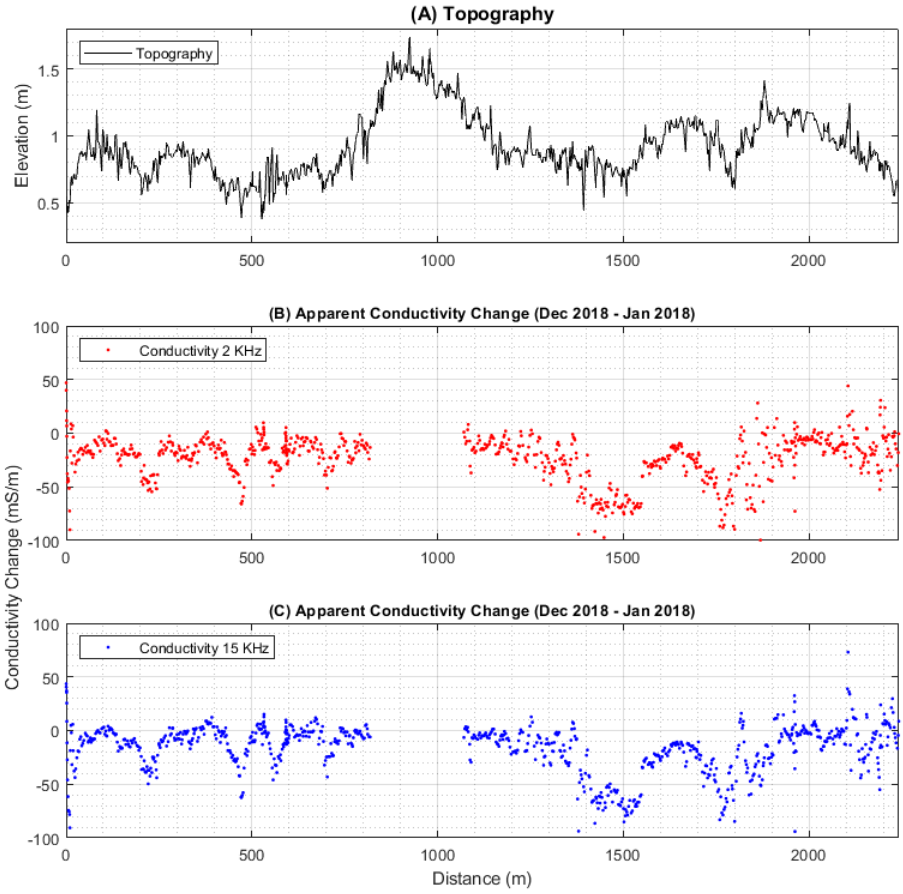

Figure 3.10: Calibrated apparent electrical conductivity change data along the EM profile line (a) topography (b) conductivity change at 2 KHz and (c) conductivity change at 15 KHz.

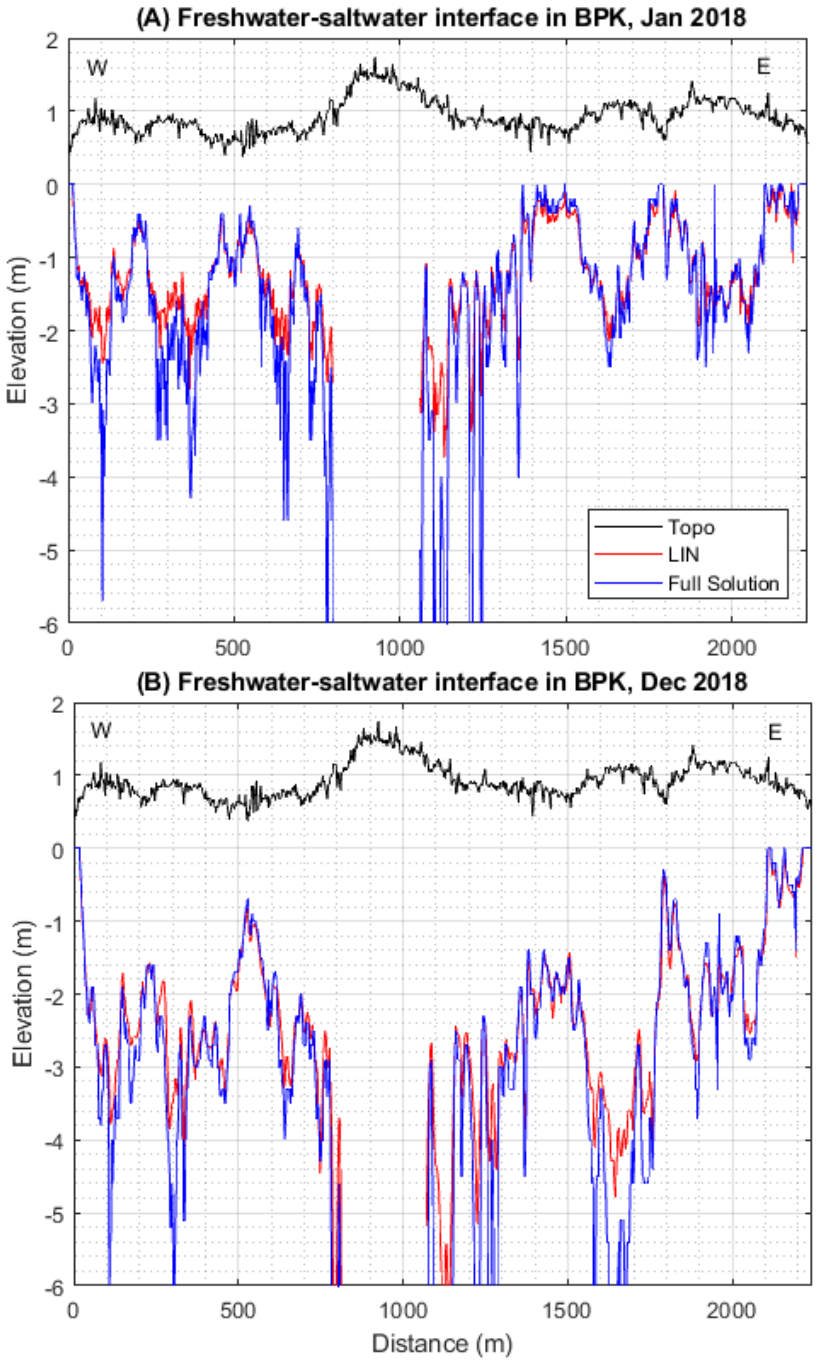

Figure 3.11: Freshwater-saltwater interface in BPK along the EM profile line (A) January 2018 and (B) December 2018.

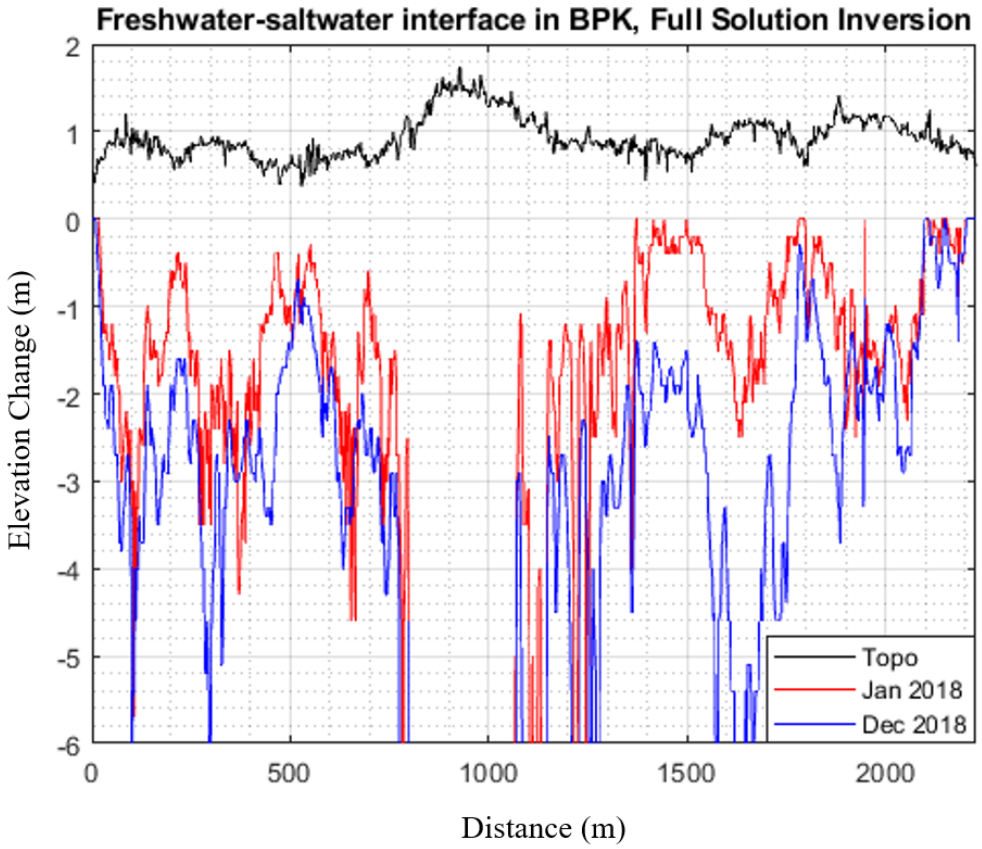

Figure 3.12: Seasonal change of freshwater and saltwater interface in BPK in January and December 2018, using the full solution inversion.

4. Geophysical Characterization of Salinity in the Shallow Water Estuarine Lakes of the Southern Everglades: A Case Study of Methods and Modeling Approaches

Abstract

Inverse modeling helps to recover information about the subsurface physical properties and the inherent non-uniqueness of the inverse solution can be reduced by adding additional constraining parameters. This paper aims to select an efficient inversion method of 1-D constrained and unconstrained electrical resistivity and electromagnetic inversion methods and compare the accuracy and consistency of the two geophysical methods. A floating electrical resistivity array and electromagnetic surveys were conducted between June to August 2019 in the Mangrove Lakes of Everglades National Park, Florida, to develop techniques for making repeatable measurements of the electrical conductivity (salinity) of the groundwater. The resistivity data were inverted to 2 and 3-layers models, and the EM data were inverted to a 2-layer model and compared four different inversion scenarios, namely free model, constrained water depth, constrained water column resistivity, and constrained water depth and resistivity model. In the free model, both the surface water resistivity and depth were allowed to be unconstrained in the inversion, whereas, for the constrained models, the water layer thickness and resistivity were fixed using the measured data using a calibrated rod and a YSI Probe.

The models were evaluated based on the goodness of fit, RMS error, percent error of the parameters, constraint of parameters, and similarity with Occam's inversion. Based on these criteria, the constrained water depth model was selected as the best model to invert the resistivity and EM data. In addition, the Dipole-dipole array provided a greater depth

penetration and better resolution than the Schlumberger array. In the study area, a comparison of the constrained water depth 2-layer and 3-layer resistivity and EM models suggested, a 2-layer model is valid in West Lake and Seven Palm system, and a 3-layer model is recommended in the Mrazek Pond due to the presence of clay materials beneath the pond. Furthermore, the goodness of fit in the models and low RMS error alone may not explain the underlain geology in detail. Therefore, an integrated approach of using EM, resistivity, and other geological information is necessary to characterize the subsurface formation accurately.

4.1. Introduction

The Mangrove Lakes are interconnected set of shallow (~ 1 m), brackish lake and creek systems on the southern margin of the Everglades National Park (ENP) adjacent to Florida Bay. This system has experienced significant changes in water quality over the past century as a result of reduced freshwater flows in the Everglades. Moreover, the highly permeable limestone aquifers bounded by ocean and brackish bays make the coastal aquifers of south Florida highly susceptible to saltwater intrusion. Thus, the reduced freshwater flow and saltwater intrusion lead to a cascading collapse of the marine and estuarine ecosystem (Park et al 2016).

The extent of saltwater intrusion in coastal aquifers can be estimated by direct salinity measurements in observation wells and geophysical measurements. Freshwater and saltwater interaction in coastal aquifers using geophysical methods have been studied extensively, however, only limited studies have been conducted in estuaries (Acworth et al. 2003; Mansoor et al. 2003; Shalem et al. 2015). Mansoor et al. (2006) used an EM31

terrain-conductivity meter to characterize shallow water wetlands contaminated by leachates from adjacent landfills and/or salt water ingress from a partial tidal connection in Kearny Marsh, New Jersey. The authors used a 1-D laterally constrained inversion 2-layer model, where the surface water conductivity and depth were fixed from the surface water quality probe measurements and inverted only for the sediment conductivity.

Geophysical methods have been used and applied to solve hydrogeological and environmental problems. In different environmental settings (water or land), the choice of Electromagnetic (EM) modeling approach depends on the type of instrument used, coil orientation, and geological setting. Similarly, in the electrical resistivity method, it depends on electrical array configuration, sensitivity to the target of interest, signal-to-noise ratio, depth of investigation, lateral data coverage (Sharma and Verma 2015), and geological setting. An integrated approach of electrical resistivity and electromagnetic is advisable to establish layer thicknesses and resistivity models. However, a different combination of resistivity and thickness of the subsurface layer can produce the same or similar result known as a principle of equivalence (Koefoed 1969). This means the difference can't be seen in the sounding curves. Furthermore, the suppression principle (hidden layer problem) suggests when an intercalated layer that has an intermediate resistivity sandwiched between two conducting beds would produce no effect on the resistivity curves unless it is very thick if the products of their thicknesses and resistivities are the same (Kunetz 1966; Sanuade et al. 2019). Generally, the intercalated layer is detected if its thickness is greater than its depth, and its resistivity differs from the cover layer (Knödel et al. 2007). Therefore, to reduce this such ambiguity, and the inherent non-uniqueness of the inverse solution, adding additional constraining parameters are required.

Different studies have been conducted using a constrained inversion model of electrical resistivity and EM methods. Constrained inversion methods were applied on a layered and laterally constrained 2-D inversion of DC resistivity (Auken and Christiansen 2004), continuous resistivity profiling (CRP) (Day-Lewis et al. 2006; Auken et al. 2005), time-domain EM data (Vignolo et al. 2015) and mutually constrained Inversion (MCI) of electrical and electromagnetic data (Auken et al. 2001; Christiansen et al. 2007). Day-Lewis (2006) mentioned incorporating constraints on the water-column resistivity and thickness enhances the resolution and accuracy of CRP. The model resolution improves when the number of unknowns is reduced. In addition, the author suggested that the accuracy of the constraining parameters is critical because a small error applied in constraining the parameters led to significant errors in the result. Dell'Aversana (2005) used water depth constrained inversion in marine controlled-source EM data and suggested constrained inversion allows to resolve complicated models with multiple resistivity layers, and also in shallow water conditions.

In this study, coincident vertical electrical and electromagnetic soundings were conducted in the summer of 2019 in the Mangrove Lakes of ENP, Florida, to evaluate geophysical techniques for characterizing the electrical conductivity and salinity of the groundwater. These data were modeled with a range of approaches to determine the best methods to constrain the inverse models with ancillary water depth and electrical conductivity measurements. In addition, the ability of these techniques to differentiate between 2-layer and 3-layer models were evaluated. This study attempts to develop a geophysical characterization technique applicable to shallow groundwater estuarine lakes of varying salinity.

This study investigated the adaptability of an efficient resistivity array configuration (Schlumberger or Dipole-dipole array) and determine the best approach on 1-D inversion parameter constraints of vertical electrical sounding (VES) model. Four different inversion scenarios, namely free model, constrained water depth, constrained water column resistivity, and constrained water depth and resistivity model, were compared. In the free model, both the surface water resistivity and depth were allowed to be unconstrained in the inversion. Whereas, for the constrained models, the water layer thickness and resistivity were fixed using the measured data using a calibrated rod and a YSI Probe. The accuracy of the inverse model is evaluated based on the goodness of fit, percent error of the parameters, constraining of the parameters, and similarity with the Occam's inversion.

The geophysical survey was conducted in the West Lake and Mrazek Pond, Mangrove Lakes of ENP. The VES was conducted using a floating Dipole-dipole and Schlumberger 14 electrode array using Advanced Geosciences Inc (AGI) Super Sting R1 IP meter. In addition, a coincident EM survey was conducted using GSSI Profiler EMP-400 multi-frequency EM conductivity meter in a Vertical dipole orientation using 1 to 15 KHz frequencies and selected frequency of 2, 8, and 15 KHz.

4.2. Data and Methods of Analysis

4.2.1. Data Collection

On this project, initially, a floating array was designed to gain better information on the lake sub-bottom conductivity and associate the results from the electrical resistivity, well data, and EM Profiler. We designed a floating Schlumberger electrical resistivity array

using a PVC tube of 10 m long and 6 cm in diameter. The potential electrodes were set at 0.25 m, and 0.50 m spacing and the current electrodes were set between 0.5 m to 5.0 m spacing. The floating Schlumberger electrical resistivity array works properly when deployed on the freshwater pond at Florida International University. However, in the brackish Mangrove lakes of ENP at a specific electrode number, a random error generated and distorted the sounding curve. This distortion could be associated with electrical inductive interference. Besides, the hose clamp used as electrodes oxidized and corroded quickly in the brackish water, and it was difficult to conduct repeated measurements. As a result of this, we order a passive graphite electrode cable from Advanced Geosciences Inc (AGI), designed for corrosive environments.

Electrical resistivity and EM surveys were conducted in West Lake and Mrazek Pond Mangrove Lakes of ENP between June to August 2019 (Figure 4.1). The specific site, survey date, and array types are summarized in Table 4.1. The electrical resistivity surveys were conducted using a floating Dipole-dipole and/or Schlumberger array of 14 graphite electrodes spaced at one-meter intervals using AGI Supersting resistivity meter (Figure 4.2). A schematic diagram of the Dipole-dipole and Schlumberger electrical resistivity array is shown in Figures 4.3 and 4.4. In Dipole-Dipole arrays, the dipoles are equal in width (a) and separated by a distance n*a, where n is an integer multiplier (Figure 4.3). In Schlumberger array, the potential electrodes (M and N) are placed close together in the center and the current electrodes (A and B) are moved outward to a greater separation throughout the array (Figure 4.4).

In the Dipole-dipole array, 48 measurements were recorded with 1-meter and 2-meter dipole length. Thirty-two measurements were recorded with 1-meter dipole length

at a spacing ranging between 1 and 11 m. and 16 measurements were recorded with 2-meter dipole length at a spacing of 2, 4, 6, and 8 m. However, the 16 measurements recorded with 2-meter dipole length were not modeled because the software only supports inverting data measured at one dipole length. The measurements included reciprocal measurements where the current and potential electrode pairs are exchanged. These reciprocal measurements provide redundancy and the ability to estimate measurement uncertainty. In the analysis, the average value of the measurements with 1-meter dipole length and its reciprocal were used.

In the Schlumberger array, 12 measurements were recorded in each sounding survey that includes the reciprocal measurements. The potential electrode spacing was set at 1-meter spacing and the current electrodes were set between 3 m to 14 m spacing. In the analysis, similar to the Dipole-dipole array, the average value of the measurements and its reciprocal were used.

The EM survey was conducted using GSSI Profiler EMP-400 multi-frequency EM conductivity meter deployed in a flat-bottomed plastic kayak integrated with a GPS receiver (Figure 4.5). The instrument is calibrated at the GSSI factory by suspending it well above the ground and zeroing the field values. Besides, before data acquisition, field calibration is performed on-site. This field calibration procedure removes any electromagnetic effects of the operator and other equipment in the surrounding area. The Profiler can record data at frequencies on the range 1 to 16 KHz and measure at three frequency at a time. During the survey, the data were recorded in vertical dipole orientation using all the frequencies between 1 and15 KHz in June 2019 and selected frequency of 2, 8, and 15 KHz in June and August 2019. The 1 to 15 KHz data set were recorded by

continuously changing three frequency after each sounding. During the geophysical survey, surface water conductivity, temperature, and salinity were measured with the help of water quality YSI probe measurement. In addition, the depth of the water column was measured using a calibrated rod. These measurements were used to constrain the parameters in the inversion.

In June 2019, the survey was conducted in West lake dock (Table 4.1) and planned to develop field procedures and to compare resistivity array configuration of Schlumberger or Dipole-dipole. The measurements were performed both with the cable placed on the lake bottom and floating on the surface using foam noodles to provide flotation. However, due to poor water visibility in the lakes, it was difficult to see the cable on the lake bottom and to verify that the electrodes were at their proper positions. Hence, all future deployments were conducted using a floating array. The results from this survey were the baseline for future data collection dates. A detailed comparison of the Schlumberger and Dipole-dipole is presented in section (4.3.1).

A preliminary data analysis of the surface water conductivity from the YSI probe and the Dipole-dipole resistivity model showed a 27 % variation on the results. Hence, calibration of the instruments was required to acquire accurate results. We calibrated the YSI Probe in the office using standard conductivity solutions of 1000 µS/cm and 12890 µS/cm, according to the in-situ Inc (https://in-situ.com) instructions. The DC resistivity meter was tested using the super sting receiver test box. The measured resistance was 440 mΩ, with a standard deviation of 0.3%. According to AGIUSA recommendation, the measured resistance value should be equal to 500 mΩ (+/-5%) with an acceptable range of 475 to 525 mΩ (https://www.agiusa.com/). As a result of this, the DC resistivity meter was

returned to the AGIUSA factory for proper instrument maintenance and calibration. After calibration, most of the sounding results were consistent with the YSI probe measurements (Appendix 4A). Therefore, it is advisable to clean the YSI probe with distilled water before every measurement and calibrate the YSI probe frequently.

In July 2019, after the instrument calibration, a Dipole-dipole resistivity sounding was conducted in the West lake system (Table 4.1). However, due to a calibration error of the EM instrument, we were unable to conduct an EM survey. The July 2019 data set analysis is presented in chapter five in detail. Later in August 2019, the Dipole-dipole resistivity and EM measurements were repeated in West Lake dock and Mrazek Pond to assess the modeling approach of 2-layer and 3-layer models (Table 4.1).

4.2.2. Data Analysis

The resistivity and EM data were inverted to a 1-D sounding model using IX1D V3 software (http://www.interpex.com/ix1dv3/ix1dv3.htm). IX1D V3 allows modeling of the subsurface using either ridge regression or a smooth model approach (Occam's Inversion). In the ridge regression both the layer thickness and resistivity are modeled (Stoyer 2008; Inman 1975). IX1D V3 also provides an equivalency analysis that shows the possible range of models that can fit the data and provides information about the non-uniqueness of the model. The equivalency analysis is based on the resolution matrix, which is a byproduct of the inversion process. When the inverse solution reaches the best fit, the parameters increment to adjust until the fitting error reaches 1.2 times the best-fit error and uses to determine the range of the equivalent parameters (Stoyer 2008). However, this analysis assumes linearity in the model.

For the smooth model inversion, the layer thicknesses are fixed and the algorithm produces the best fit of the data while minimizing the change in resistivity between the layers (Constable et al. 1984). Occam inversion provides the smoothest possible model and generally doesn't show sharp changes (Constable et al. 1984). In this study, in the Occam's inversion, 10 layers over an infinite half-space were used, and the layer thickness increased progressively from 0.1 to 5 m. The Occam's inversion is a smooth model that depends weekly on the starting value and avoids the problem in the selection of the starting model (Chang-Chun et al. 2019).

The resistivity data were inverted to a 2-layer model and compared four different inversion methods, such as free model, constrained water depth, constrained water column resistivity, and constrained water depth and resistivity models. In the free model, both the surface water resistivity and depth were allowed to be unconstrained in the inversion. Whereas for the constrained water depth model, the water layer thickness was fixed, and for the constrained water column resistivity model, the surface water resistivity was fixed. In the constrained water depth and resistivity model, both the surface water resistivity and depth were fixed. In addition, a comparison of constrained water depth 2-layer and 3-layer models were performed on the data collected in August 2019 in West Lake and Mrazek Pond.

In all the inversion scenarios, the starting model of the 2-layer model used was the resistivity and depth of the water column measured using a YSI probe and a calibrated rod. These values were constrained depending on the inversion approach. In addition, the lake bottom resistivity value was assumed five times higher water column resistivity based on

the previous study. In the 3-layer models, we used the same constraining approach as the 2-layer model and assumed 1 m starting depth for the 2nd layer. This second layer thickness remained unconstrained in the inversion.

The frequency-domain EM data were inverted using IX1D V3 as a 2-layer model. During inversion, the inphase values were masked, because a few inphase measurements in the lower frequency range were negative. Therefore, only the quadrature component was inverted. Similar to the resistivity model, the best fit model was obtained by constraining the parameters using the measured value from the YSI probe and calibrated rod. The Occam's inversion used a 10 layer model and the thickness of the layer increases with depth that ranges between 0.1 m to 5 m.

4.3. Results and Discussion

In this study, we compared geophysical approaches to characterizing the electrical conductivity and salinity of the groundwater beneath the lakes. This included comparing vertical soundings using the dipole-dipole and Schlumberger arrays (section 4.3.1). In addition, we compared the effect of model parameter constraints (resistivity and depth) on the inversion quality (section 4.3.2). Next, we explored the ability of VES to distinguish between a 2 -layer model corresponding to surface water over limestone bedrock from a 3-layer model which included a clay sediment layer over the limestone (section 4.3.3). Finally, the results of resistivity and EM soundings were compared to determine the accuracy and consistency of the two methods (section 4.3.4). The modeling techniques developed in this study can be used to effectively characterize the salinity of shallow-water estuarine lakes and/or aquifers.

4.3.1. Comparison of Dipole-dipole and Schlumberger resistivity array

The resistivity survey on June 06, 2019, was planned to develop field procedures and to select efficient resistivity array configuration. We compared Schlumberger and dipole-dipole array, and its reciprocal measurements. The reciprocal measurements were conducted by swapping the current and potential electrodes. In this section, constrained water depth Schlumberger and Dipole-dipole array inversion is presented, as the constrained water depth inversion is used for the future analysis. In West Lake, during the survey, the surface water resistivity measured with the YSI probe was 0.36 Ω·m, and the depth of the water column measured was 1.0 m. During inversion, the depth of the water column was constrained to 1 m depth and the starting model of the surface water and lake bottom was 0.36 Ω·m and 1.8 Ω·m.

The Occam's inversion result is closely aligned with the best fit model of the Dipole-dipole array compared to the Schlumberger array. Generally, the Occam's inversion and the best fit model, in both the Dipole-dipole array and Schlumberger array models have a reasonable fit. In the Schlumberger array, both the best fit and Occam's inversion and the Dipole-dipole, the best fit model have a poor fit in the short spacing.

The Dipole-dipole array is highly constrained and repeatable compared to the Schlumberger array. For example, the Dipole-dipole array estimated the surface water resistivity to 0.26 Ω·m, and the lake bottom resistivity to 1.43 Ω·m and 1.47 Ω·m (Figure 4.6; Table 4.2). In contrast, the Schlumberger arrays estimated the surface water resistivity to 0.36 Ω·m and the lake bottom resistivity to 3.92 Ω·m 4.60 Ω·m. This showed the dipole-dipole array repeatability is superior compared to the Schlumberger array. In addition, based on the equivalency analysis, the Dipole-dipole array is highly constrained with a

lower and upper limit of less than 0.5 Ω·m range (Table 4.2). In contrast, in the Schlumberger array, the lower and upper limits ranged to 4.74 Ω·m and 6.86 Ω·m (Table 4.2). The comparison of the modeling results from Schlumberger and Dipole-dipole data indicated that the Dipole-dipole array provided better repeatability and parameter resolution than the Schlumberger array. Sharma and Verma 2015 also demonstrated the characteristics of different 2-D array configurations such as the Dipole-dipole, Pole-pole and Pole-Dipole, Wenner, and Wenner-Schlumberger. Among these array configurations, the authors suggested Dipole-dipole has the greatest degree of sensitivity to vertical structures.

4.3.2. Comparison of parameter constraints on VES model accuracy

The electrical resistivity data collected on July 15, 2019, in the West lake system and on August 16, 2019, in the West lake dock were inverted to a 2-layer model in IX1D V3. Four different inversion approaches, namely the free model, constrained water depth, constrained water column resistivity and constrained water depth and resistivity model, were compared (Figure 4.7; Table 4.3). The comparison results of the four resistivity inversion approaches, on the data collected on August 16, 2019, is presented below, and the results on the data collected on July 15, 2019, is summarized in the Appendix 4A. Further analysis of this data set is included in Chapter Five of this dissertation.

All the four inversion scenarios are similar to the Occam's inversion. In all the four inversion scenarios, the best fit and Occam's inversion showed a good agreement in estimating the water column resistivity. However, in estimating the lake bottom resistivity, in the top 3 m, the best fit model is higher than the Occam's inversion in the free model

and constrained water column resistivity (Figure 4.7a and 4.7c). In contrast, in the constrained water depth and constrained water depth and resistivity, the best fit model is within the average values of the Occam's inversion over the same depth range (Figure 4.7b and 4.7d). This suggests the Occam's inversion of the lake bottom resistivity has a better agreement with the best fit model of the constrained water depth and constrained water depth and resistivity.

The resistivity models obtained using the free model, constrained water column resistivity, constrained water depth, and constrained water depth and resistivity have the best goodness of fit and lower RMS error, respectively (Figure 4.7). The constrained water depth showed a reasonable fit and small deviation in the short spacing that corresponds with the water column resistivity. The constrained water depth and resistivity model has poor goodness of fit with an RMS value of 12 %. Day-Lewis et al. (2006) suggested that constraint-based inversion can improve the accuracy of the model, but a small error in the constrain measurements can lead to a large error in the inversion result. Therefore, the accuracy of the constraint value is critical in the inversion. As a result of this, the constrained water depth and resistivity model is not recommended to invert the data.

A percent error is calculated by comparing the inverse modeling result with the measurements obtained from the YSI probe and the calibrated rod. The percent error of the water depth constrained model is less compared to the free model and water column resistivity. The water column resistivity was 0.42 Ω·m measured using the YSI probe, and the water column depth was 1.2 m measured using the calibrated rod. In the inverse model, the free model estimated the surface water resistivity to 0.43 Ω·m with a percent error of 2 %, and the constrained water depth estimated to 0.35 Ω·m, with a percent error of 16 %.

However, the free model estimated the water column depth to 1.97 m with a percent error of 64 % and the constrained water column resistivity estimated to 1.91 m with a percent error of 59 %. This result showed in the inverse model, the percent error of the water column resistivity is greater than the depth. This result is consistent in all sounding curves (Table 4.3; Appendix 4A). Equivalency analysis showed that the variation of the water column resistivity of the inverted models, and the YSI probe measured values are minimal. But, the difference between the water column depth of the inverse models and measured values is large. Therefore, the models which don't constrain the water depth may lead to overestimating the lake bottom resistivity (Table 4.3). The constrained water depth model has less percent error and could be a reasonable approach to estimate the lake bottom resistivity.

All the models showed a highly constrained resistivity of the water column and a moderately constrained in the water depth and lake bottom resistivity. Based on the equivalency analysis, the four inversion scenarios estimated the water column resistivity on the range from 0.35 to 0.43 Ω·m and the water column depth on the range 1.20 m to 1.97 m and the lake bottom resistivity on the range from 1.15 to 2.85 Ω·m (Figure 4.7; Table 4.3). The estimated lake bottom resistivity of the free model and constrained water column resistivity models are higher than the constrained water depth and constrained water depth and resistivity models (Table 4.3). In the figures, where the equivalence analysis (dashed green line) showed a tightly constrained result, the best fit model is reasonably accurate. In cases where the equivalence analysis is unconstrained, the best fit model showed less confidence in the accuracy of the model (Al-Garni and El-Kaliouby

2009). Based on the equivalence analysis, lake bottom resistivity is highly constrained in the constrained water depth and constrained water depth and resistivity models.

Comparing all the four inversion cases, the constrained water depth and resistivity model has a poor fit. Both the free model and constrained water resistivity have the best fit and low RMS error but overestimated the depth of the water column. The best fit obtained using the constrained water depth is more similar to the Occam's inversion than other models. This model is highly constrained and has a less percent error. Therefore, based on these assumptions, the constrained water depth model is selected as the best model to invert the resistivity data.

4.3.3. Comparison of 2 and 3-layer resistivity models

A comparison of constrained water depth 2-layer and 3-layer resistivity models were conducted on the data collected on August 16, 2019, in Westlake dock and Mrazek Pond (Figure 4.8; Table 4.4). The comparison of 2 and 3 layers resistivity aims to develop an inversion procedure for the electrical and EM data collected between 2016 to 2019 and characterize the conductivity (salinity) of the groundwater beneath the lakes, in other words, to detect weathered product. The mangrove lake is found on top of the limestone aquifer, and two kinds of soil, marl, and peat occur in this region (Lodge 2010). Marl is the most common soil seen on the drive to Flamingo along the main park road (Figure 4.1; Stewart et al. 2002; NPS 2020). Marl is composed of calcium carbonate with variable amounts of clays and silt. Clay is known for its lower resistivity compared with other kinds of rock (Nor et al. 2006).

In West Lake, the thickness of the water column was fixed to 1.2 m measured using the calibrated rod, and the surface water resistivity was 0.42 Ω·m measured using the YSI probe. In the 2- layer model, the lake bottom resistivity is estimated to 1.44 Ω·m with a lower and upper limit on the range 1.18 to 1.85 Ω·m (Figure 4.8a; Table 4.4). In the 3-layer model, the lake bottom resistivity is estimated to 0.80 Ω·m with an acceptable range 0.58 to 0.98 Ω·m for the 2nd layer and 6.4 Ω·m with an acceptable range 3.44 to 9.15 Ω·m for the 3rd layer (Figure 4.8b; Table 4.4). The 2-layer model fits the data reasonably, and an improved fit obtained in the 3-layer model. The Occam's inversion estimated the lake bottom resistivity approximately to 1 Ω·m. The Occam's inversion is very similar to the 3-layer model and the 2-layer model is similar to the average Occam's inversion over the same depth range. The resistivity data is similar to an "A type" curve (where the resistivity increase continuously with depth), which makes it difficult to distinguish between 2 and 3 layer models. Based on the equivalency analysis, the 2-layer model is highly constrained than the 3-layer model. In the 3-layer model, the intermediate layer is not resolved uniquely. The 2-layer model is a simple model that represents the surface water and the lake bottom resistivity. Thus, the 2-layer and 3-layer comparisons show that adding another layer does not provide a better model. Consequently, a two-layer model appears to be adequate for modeling the data.

In Mrazek Pond, the depth of the water column was fixed to 0.77 m measured using the calibrated rod. In the inverse model, the 2-layer model poorly fits the resistivity data and has an RMS error of 16 % (Figure 4.8c; Table 4.4). This curve is an example of H-type curves that requires the resistivity first to decrease and then increase (Zhody 1968). Hence, it is impractical to fit a 2-layer model. The 3-layer model fit the resistivity data perfectly

and estimated the resistivity of the second and third layers to 0.67 Ω·m and 3.13 Ω·m, respectively, with an RMS error of 0.93 % (Figure 4.8d; Table 4.4). This low resistivity in the 2nd layer indicates the presence of clay material. The clay material was not resolved in the 2-layer model. Clays can dramatically decrease the resistivity (increase the conductivity), due to a huge surface area to volume ratio that enhanced a higher Cation Exchange Capacity (CEC) (Sill and Klein 1981). During the survey, at the base of the calibrated rod clay particles were observed. The results from the Occam's inversion is much more similar to the 3-layer model, and it is highly constrained. Therefore, the 3-layer model is superior over the 2-layer model and recommended to invert the data as a 3-layer model in Mrazek pond. Therefore, the selection of a 2-layer and 3-layer model needs careful interpretation of the data and the geology of the subsurface formation.

4.3.4. Comparison of Resistivity and EM models

A coincident electrical resistivity and EM sounding survey were conducted in West Lake on June 14, 2019, to compare the accuracy and consistency of the two geophysical methods. Both the electrical resistivity and EM methods showed a consistent result. In this section, we compared the Dipole-dipole sounding (Figure 4.9a), EM sounding using 1 to 15 KHz frequencies (Figure 4.9b), and selected frequencies of 2, 8, and 15 KHz (Figure 4.9c). In the inverse model, the water column depth was fixed to 1.05 m measured with the calibrated rod and a starting resistivity value of 0.36 Ω·m and 1.8 Ω·m were used for the surface water and lake bottom resistivity. In the inverse model, the surface water resistivity is estimated on the range 0.26 to 0.31 Ω·m. The slight variation in surface water resistivity

among the YSI measured value, and the inverse models could be due calibration problem of the YSI probe and/or the resistivity meter.

In general, the models estimated the lake bottom resistivity on the range of 1.60 to 1.89 Ω·m (Table 4.5). All the models are well constrained, have low RMS error, and have a similar pattern with the Occam's inversion. Surprisingly, both the electrical resistivity and EM sounding using frequencies 1 to 15 KHz estimated the lake bottom resistivity to 1.6 Ω·m. Based on the equivalency analysis, the EM best-fit model overlapped with the lower and upper confidence limits of the resistivity model. In addition, the EM model using selected frequencies of 2, 8, and 15 KHz estimated the lake bottom resistivity to 1.89 Ω·m (Table 4.5) and suggested the EM model using the selected frequencies is a reasonable approach to use for a rapid survey. The fact the resistivity and EM models are similar, highly constrained, and low RMS error suggests the consistency of the two geophysical methods and the ability to characterize the lake bottom resistivity. Besides, the goodness of fit in the models with low RMS error alone may not explain the subsurface formation in detail. Therefore, using different geophysical methods helps to resolve the subsurface formation accurately.

4.4. Conclusions

A geophysical survey of electrical resistivity and EM were conducted between June to August 2019 in the Mangrove Lakes of Everglades National Park, Florida, to develop techniques for making repeatable measurements of the electrical conductivity (salinity) of the groundwater. This study aims to select an efficient inversion method of 1-D constrained and unconstrained electrical resistivity and electromagnetic inversion methods and

compare the accuracy and consistency of the two geophysical methods. This paper investigated four different inversion methods, namely the free model, constrained water depth, constrained water column resistivity, and constrained water depth and resistivity models. The models were evaluated based on the goodness of fit, RMS error, percent error of the parameters, constraint of parameters, and similarity with Occam's inversion. In this study, we concluded:

1. The comparison of the modeling results from Schlumberger and Dipole-dipole data indicated that the Dipole-dipole array provided both greater depth penetration and better resolution than the Schlumberger array.
2. Comparing all the four inversion cases, the constrained water depth approach has reasonable goodness of fit; the best fit obtained is similar to the Occam's inversion; the model is highly constrained and has a less percent error. Therefore, based on these criteria, the constrained water depth model is selected as the best approach to invert the resistivity data and EM data.
3. The comparison of the constrained water depth 2-layer and 3-layer resistivity and EM models suggested, a 2-layer model is valid in West Lake and Seven Palm system, and a 3-layer model is recommended in the Mrazek Pond.
4. The Dipole-dipole array resolves a clay sediment layer overlying on the top of limestone bedrock
5. The compassion of the resistivity and EM models showed the consistency of two geophysical methods and the ability to characterize the lake bottom resistivity.

4.5. References

Acworth, R., Dasey, G. Mapping of the hyporheic zone around a tidal creek using a combination of borehole logging, borehole electrical tomography and cross-creek electrical imaging, New South Wales, Australia. *Hydrogeology Journal* 11, 368–377 (2003). https://doi.org/10.1007/s10040-003-0258-4

AGIUSA. (2019). SuperSting™ Wi-Fi. Retrieved July 30, 2019, from agiusa.com website: https://www.agiusa.com/supersting-wifi

Al-Garni, M. A., & El-Kaliouby, H. M. (2011). Delineation of saline groundwater and seawater intrusion zones using transient electromagnetic (TEM) method, Wadi Thuwal area, Saudi Arabia. *Arabian Journal of Geosciences*, *4*(3-4), 655-668.

Auken, E., Pellerin, L., & Sørensen, K. I. (2001). Mutually constrained inversion (MCI) of electrical and electromagnetic data. In *2001 SEG Annual Meeting*. Society of Exploration Geophysicists.

Auken, E., & Christiansen, A. V. (2004). Layered and laterally constrained 2D inversion of resistivity data. *Geophysics*, *69*(3), 752-761.

Auken, E., Christiansen, A. V., Jacobsen, B. H., Foged, N., and Sørensen, K. I. (2005). Piecewise 1D laterally constrained inversion of resistivity data. *Geophysical Prospecting*, *53*(4), 497-506.

Christiansen, A. V., Auken, E., Foged, N., and Sørensen, K. I. (2007). Mutually and laterally constrained inversion of CVES and TEM data: a case study. *Near Surface Geophysics*, *5*(2), 115-123.

Constable, S. C., Parker, R. L., and Constable, C. G. (1987). Occam's inversion: A practical algorithm for generating smooth models from electromagnetic sounding data. *Geophysics*, *52*(3), 289–300.

Day-Lewis, F. D., White, E. A., Johnson, C. D., Lane, J. W., and Belaval, M. (2006). Continuous resistivity profiling to delineate submarine groundwater discharge—examples and limitations. *The Leading Edge*, *25*(6), 724–728.

Dell'Aversana, P. (2005). The importance of using geometrical constraints in marine Controlled Source Electromagnetic data inversion. In *2005 SEG Annual Meeting*. Society of Exploration Geophysicists.

EPA. (2016). Resistivity Methods. Retrieved October 29, 2019, from EPA website: https://archive.epa.gov/esd/archive-geophysics/web/html/resistivity_methods.html

Inman, Joseph Robert. 1975. Resistivity Inversion With Ridge Regression. *Geophysics* 40 (5): 798.

Knödel, K., Lange, G., and Voigt, H. J. (2007). *Environmental geology: handbook of field methods and case studies*. Springer Science and Business Media.

Koefoed, O. (1979). Resistivity sounding on an earth model containing transition layers with linear change of resistivity with depth. *Geophysical Prospecting*, 27(4), 862–868.

Kunetz, G. (1966). Principles of direct current-Resistivity prospecting. Gebriider Bomtraege Gebrüder Borntraege, Berlin, pp.103 +xvi.

Mansoor, N., Slater, L., Artigas, F., & Auken, E. (2006). High-resolution geophysical characterization of shallow-water wetlands. *Geophysics*, *71*(4), B101-B109.

Nor, N. M., Haddad, A., and Griffiths, H. (2006). Performance of earthing systems of low resistivity soils. *IEEE transactions on Power delivery*, *21*(4), 2039-2047.

National Park Service (2020); Geology - Everglades National Park (U.S.) https://www.nps.- gov/ever/ learn/nature/evergeology.htm

Park, J., Stabenau, E., Redwine, J., and Kotun, K. (2016). Hypersalinity in Florida Bay: A low-dimensional nonlinear model. 10.13140/RG.2.2.34159.33440.

Sanuade, O. A., Amosun, J. O., Oyeyemi, K. D., Olaojo, A. A., Fagbemigun, T. S., and Faloyo, J. I. (2019, August). Analysis of principles of equivalence and suppression in resistivity sounding technique. In *Journal of Physics: Conference Series* (Vol. 1299, No. 1, p. 012065). IOP Publishing.

Shalem, Y., Weinstein, Y., Levi, E. et al. The extent of aquifer salinization next to an estuarine river: an example from the eastern Mediterranean. *Hydrogeol J* 23, 69–79 (2015). https://doi.org/10.1007/s10040-014-1192-3

Sharma, S., and Verma, G. K. (2015). Inversion of Electrical Resistivity Data: A Review. *World Academy of Science, Engineering and Technology, International Journal of Environmental, Chemical, Ecological, Geological and Geophysical Engineering*, *9*(4), 392–398.

Sill, W. R., and Klein, J. D. (1981). The Electrical Properties of Clay. *US Department of the Interior, Geological Survey.*

Stewart, M. A., Bhatt, T. N., Fennema, R. J., and Fitterman, D. V. (2002). The road to Flamingo: An evaluation of flow pattern alterations and salinity intrusion in the lower glades, Everglades National Park (p. 38). *US Department of the Interior, US Geological Survey.*

Stoyer, C. (2019). 1D Resistivity, IP, EM Software (Version 3). Retrieved from http://www.interpex.com/ix1dv3/ix1dv3.htm

Vignoli, G., Fiandaca, G., Christiansen, A. V., Kirkegaard, C., and Auken, E. (2014). Sharp spatially constrained inversion with applications to transient electromagnetic data. *Geophysical Prospecting*, *63*(1), 243-255.

Zohdy, A. A. (1968). A rapid graphical method for the interpretation of A-and H-type electrical soundings. *Geophysics*, *33*(5), 822-833

Table 4.1: DC resistivity and EM data collection dates. The electrical resistivity survey includes Dipole-dipole (DD), Dipole-dipole reciprocal (DDR), Schlumberger array (SL), and Schlumberger array reciprocal (SL) configuration. The EM survey includes measurements using frequency 1 to 15 KHz (EM-15), and selected frequency of 2, 8, and 15 KHz (EM-3).

Date	**Site**	**Resistivity Array Type**	**EM Frequency (KHz)**	**Resistivity (Ω.m)**	**Depth (m)**
June 06, 2019	West Lake dock	DD, DDR, SL, SLR		0.36	1.0
June 14, 2019	West Lake dock	DD	EM-15, EM-3	0.36	1.0
July 15, 2019	West Lake System	DD		Several	Several
August 16, 2019	West Lake dock	DD	EM-3	0.42	1.2
August 16, 2019	Mrazek Pond	DD	EM-3	1.14	0.77

Note: The surface water resistivity and depth of the water column were measured using a YSI probe and calibrated rod.

Table 4.2: Comparison of constrained water depth resistivity arrays in West Lake on June 06, 2019. (a) Dipole-dipole, (b) Dipole-dipole reciprocal, (c) Schlumberger and (d) Schlumberger reciprocal array. The range of the inverse model is based on the equivalency analysis. In the inversion, the water column depth and resistivity was fixed to 1. 0 m and 0.36 Ω·m measured using the calibrated rod and YSI probe. The lake bottom starting resistivity was 1.8 Ω·m.

No	**Cases**	**Water Column**		**Lake Bottom**		
		Rho 1	**Range**	**Rho 2**	**Range**	**RMS %**
1	Dipole-dipole	0.26	0.24-0.28	1.43	1.25-1.69	5.02
2	Dipole-dipole Reciprocal	0.26	0.24-0.28	1.47	1.29-1.70	4.47
3	Schlumberger	0.36	0.30-0.43	3.92	2.32-7.06	4.58
4	Schlumberger Reciprocal	0.36	0.30-0.42	4.60	2.64-9.50	4.67

Table 4.3: A comparison of resistivity constrained vs. free inversion model in Westlake dock on August 16, 2019. The bold numbers indicate the fixed value during inversion. Range, figure % Error inverted resistivity relative to YSI and calibrated rod

No	**Cases**	**Water Column**						**Sea Bottom**		
	Resistivity model	**Rho 1**	**Range**	**%Error**	**Depth**	**Range**	**%Error**	**Rho 2**	**Range**	**RMS**
1	**Free Model**	0.43	0.40-0.45	2.38	1.97	1.78-2.16	64.16	2.85	2.18-4.05	2.80
2	**Constrained depth**	0.35	0.32-0.39	16.6	**1.20**			1.44	1.18-1.85	8.18
3	**Constrained Res**	**0.42**			1.91	1.81-2.03	59.16	2.71	2.12-3.74	2.85
4	**Constrained depth and Res**	**0.42**			**1.20**			1.15	0.98-1.38	12.18

Table 4.4: Comparison of 2-layer and 3-layer resistivity model in West Lake and Mrazek Pond on August 16, 2019.

No	Cases	Water Column		2nd - Layer				3rd - Layer		
	2 and 3 layer	Rho 1	Range	Rho 2	Range	Depth 2	Range	Rho 3	Range	RMS %
1	West Lake-2	0.35	0.32-0.49	1.44	1.18-1.85					8.18
2	West Lake-3	0.41	0.39-0.43	0.80	0.58-0.98	3.06	2.33-3.62	6.40	3.44-19.15	2.26
3	Mrazek-2	0.70	0.53-0.96	1.35	1.13-1.67					16.5
4	Mrazek-3	1.09	1.06-1.12	0.67	0.62-0.71	2.21	2.07-2.37	3.13	2.85-3.50	0.93

Table 4. 5: Comparison of constrained water depth Resistivity and EM Model. The water depth was fixed to 1. 0 m during inversion

No	Cases	Water Column			Lake Bottom		
	Model	Rho 1	Range	Depth	Rho 2	Range	RMS %
1	Resistivity Model	0.26	0.24-0.28	**1.05**	1.60	1.37-1.92	4.9
2	EM using frequencies 1 to 15 KHz	0.31	0.31-0.31	**1.05**	1.69	1.63-1.76	0.25
3	EM using frequencies 2, 8, and 15 KHz	0.31	0.31-0.31	**1.05**	1.89	1.85-1.96	0.23

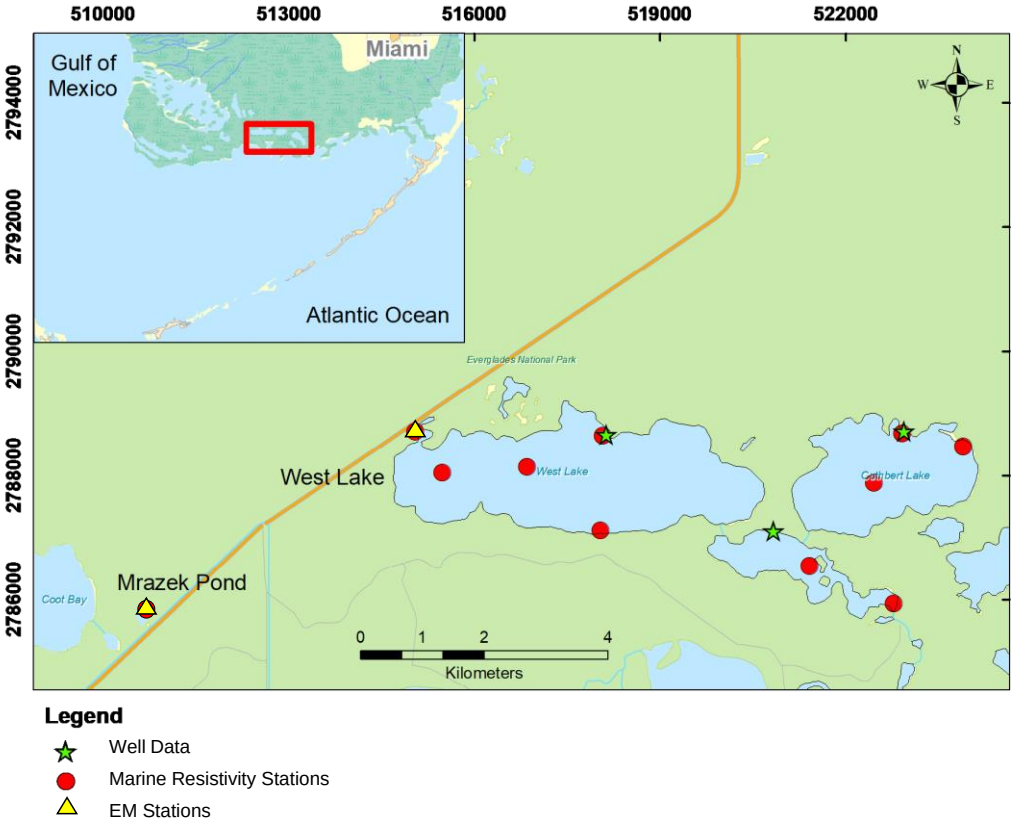

Figure 4.1: Mangrove Lake region of ENP and the location of the floating array electrical resistivity, frequency-domain electromagnetic survey, and well stations.

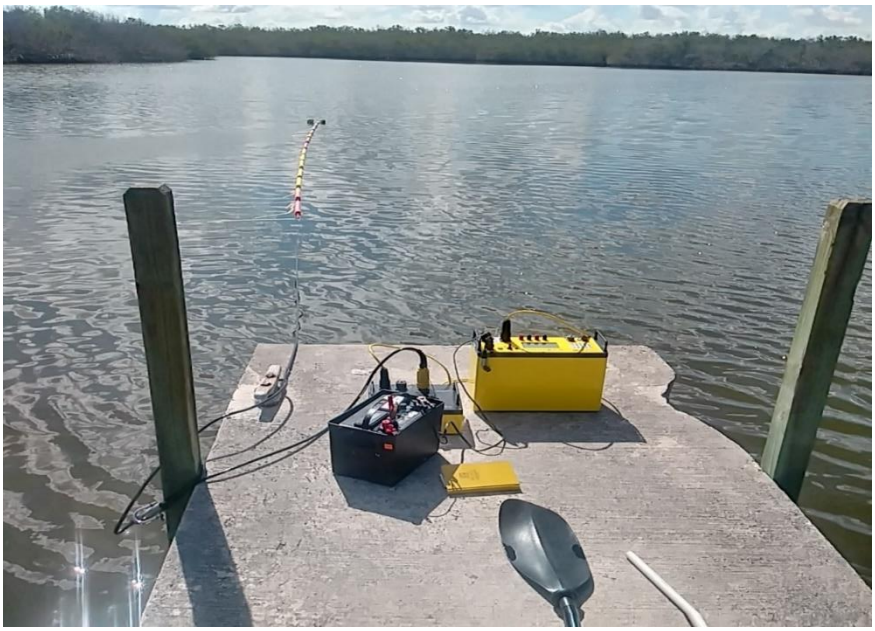

Figure 4.2: Floating electrical resistivity survey at West Lake dock, using the AGI Supersting R1/IP resistivity imaging system.

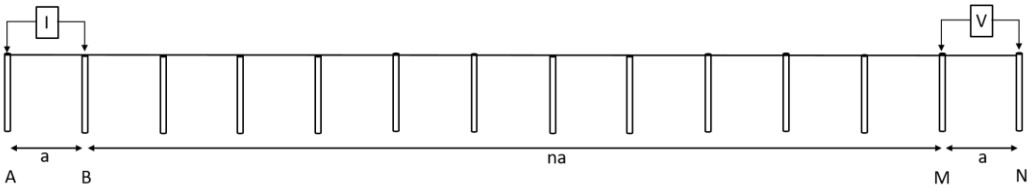

Figure 4.3:A schematic diagram of 14 electrode Dipole-dipole electrical resistivity array configuration with "a" spacing and expansion factor of "n". A and B, are the current electrode, and M and N, are the potential electrodes.

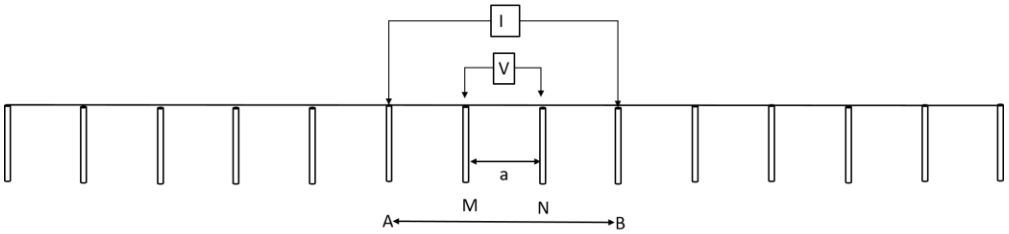

Figure 4.4: A schematic diagram of 14 electrode Schlumberger array electrical resistivity array configuration with "a" spacing. A and B, are current electrodes, moved outward to a greater separation throughout the array. M and N, are potential electrodes placed at the center.

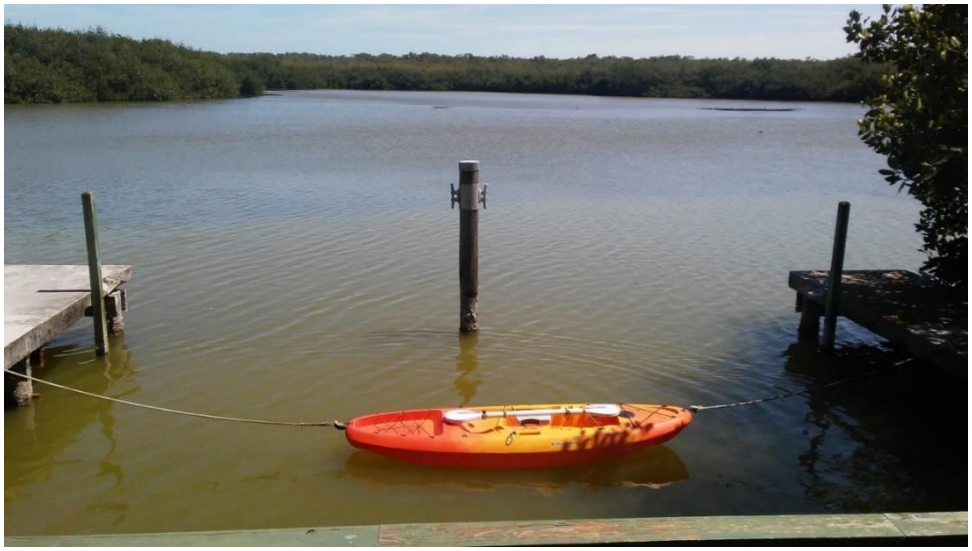

Figure 4.5: Frequency domain EM survey at West Lake dock, using the GSSI EMP 400 profiler on June 14, 2019.

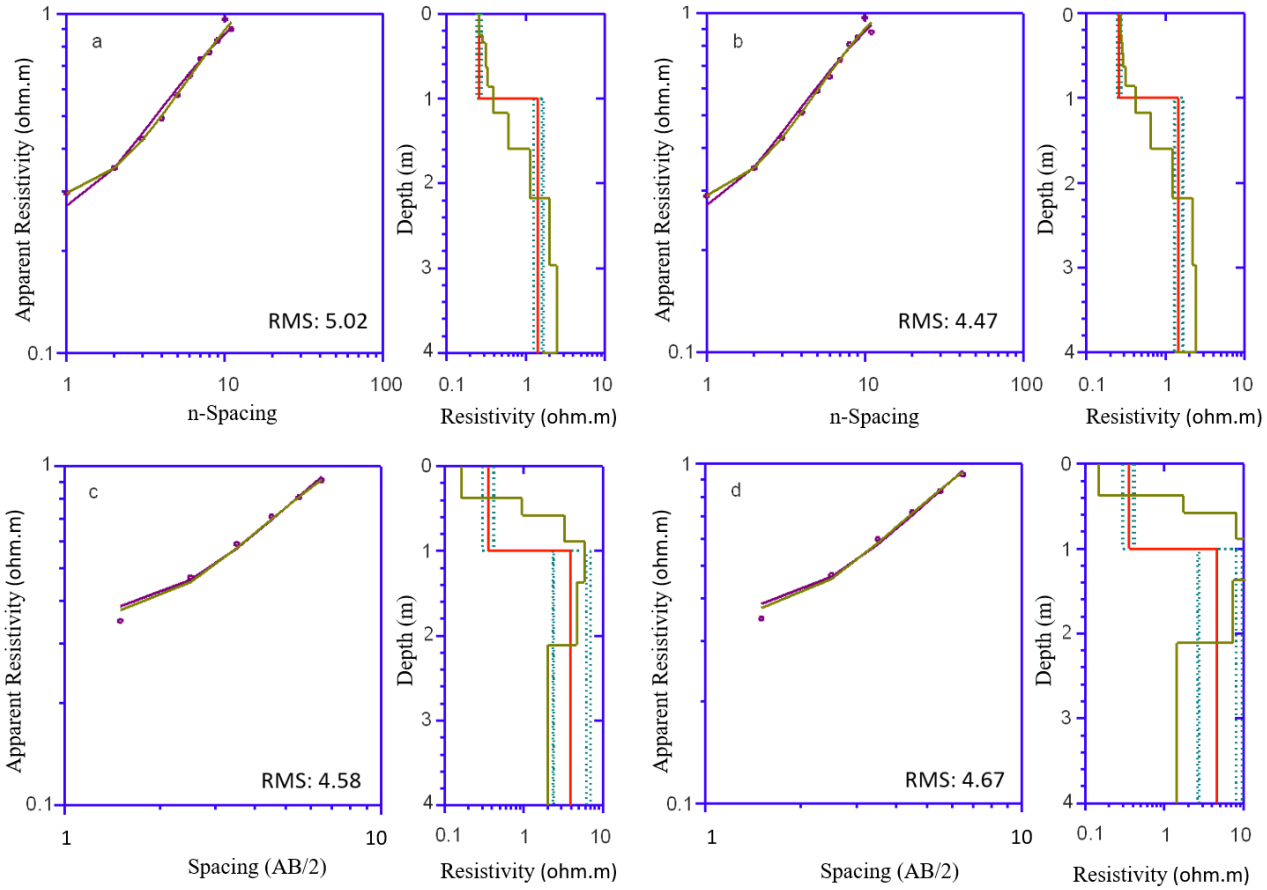

Figure 4.6: Comparison of constrained water depth resistivity arrays in West Lake on June 06, 2019. (a) Dipole-dipole, (b) Dipole-dipole reciprocal, (c) Schlumberger, and (d) Schlumberger reciprocal array. The left panel shows the observed and calculated data (lines), and the right panel shows the inverted model. In the left panel, the square dots indicates the observed data, the purple line indicates the best fit calculated data, and the olive color indicates Occam's inversion. In the right-panel, the red line indicates the best fit model; the green dashed lines indicate the equivalency analysis, and the olive line represents the Occam's inversion model.

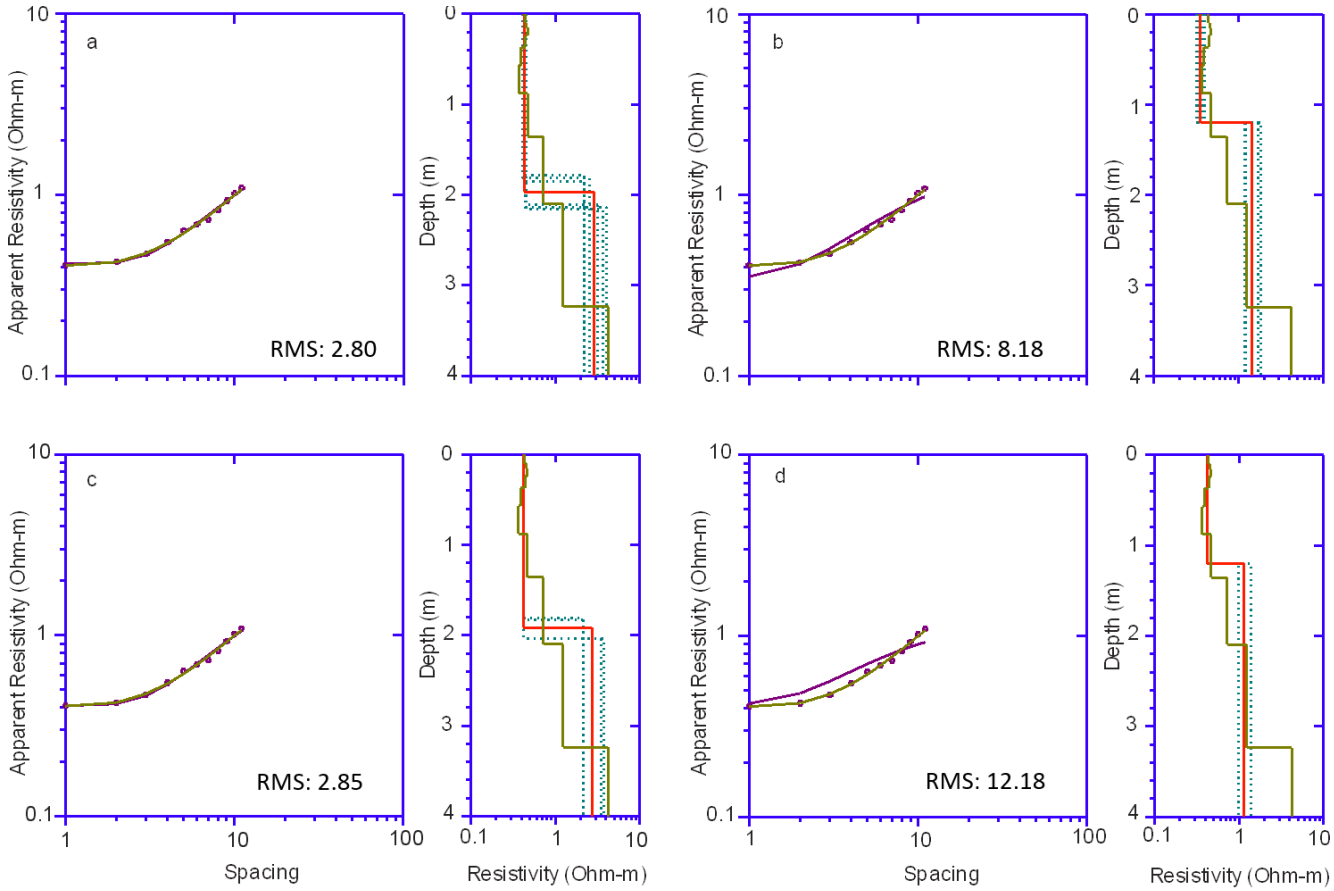

Figure 4.7: A comparison of four different inversion scenario in West Lake (WL) on August 16, 2019. (a). Free model, (b). Constrained water depth, (c). Constrained water column resistivity, and (d). Constrained water depth and resistivity model.

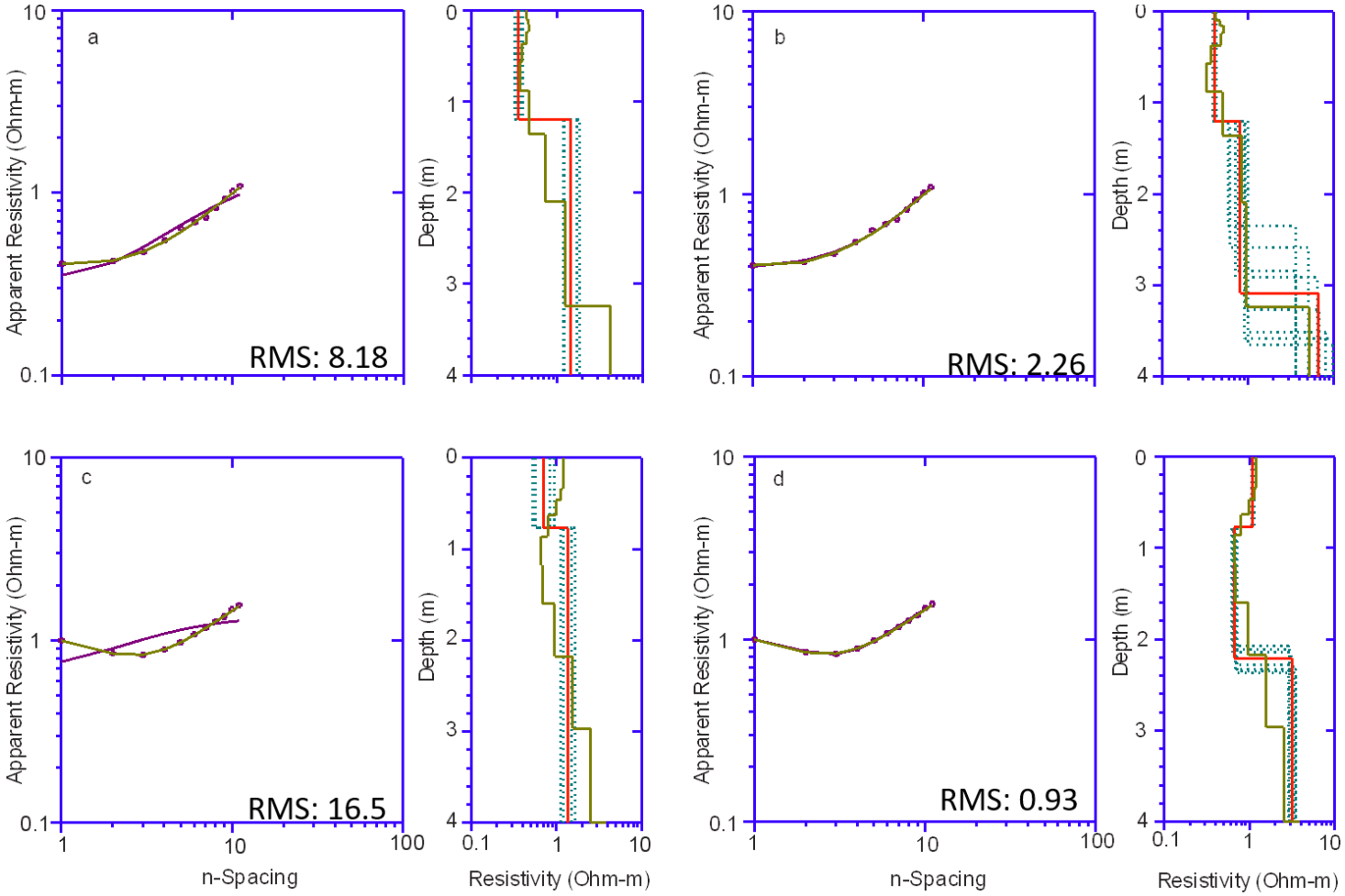

Figure 4.8: A comparison of 2 and 3-layer constrained water depth resistivity model in West Lake (a). 2-Layer (b). 3-Layer and in Mrazek Pond (c). 2-Layer and (d). 3- Layer.

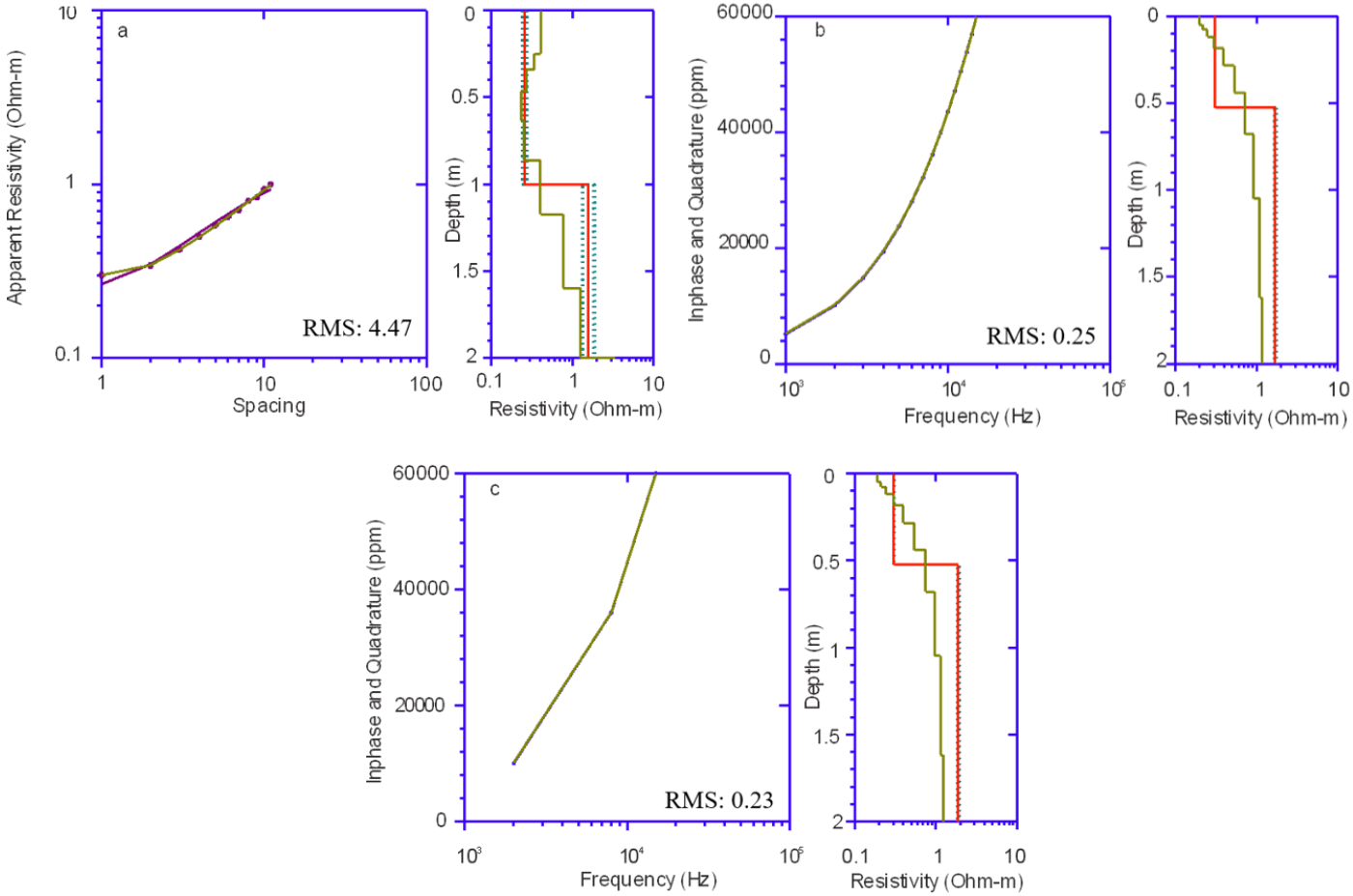

Figure 4.9: A comparison of 2-layer constrained water depth, resistivity, and EM model in West Lake on June 14, 2019. (a). Resistivity model, (b). EM Model using frequencies 1 to 15 KHz, (c). EM Model using selected frequencies of 2, 8, and 15 KHz

5. Geophysical Surveys of West Lake and Seven Palm Lake drainage systems of Everglades National Park (ENP)

Abstract

Everglades National Park (ENP) has been adversely impacted by past human activities that altered the freshwater flow through the system. The Comprehensive Everglades Restoration Plan (CERP) makes an effort to increase the flow of freshwater and modify the groundwater chemistry in Everglades National Park (ENP). This study describes the results of geophysical surveys conducted between 2016 to 2019 using electrical resistivity and EM methods in the mangrove lakes as part of a larger hydrologic and geochemical study in the ENP. This paper aims to estimate a formation factor and assess the spatial and temporal changes in the groundwater chemistry in the Southern Mangrove Lakes of ENP adjacent to Florida Bay. EM surveys were conducted from 2016 to 2017 using a multi-frequency a GSSI EMP-400 Profiler deployed in a flat bottomed plastic kayak towed behind a small boat and a floating Dipole-Dipole electrical resistivity survey was conducted on July 2019. Apparent conductivity calculated using the general equation from the EM surveys were used to assess the temporal and temporal change. Besides, the electrical resistivity data were inverted by constraining the depth of the water column as a 2 layer model.

A formation factor was estimated by comparing the bulk resistivity measured using the floating Dipole-Dipole array and coincident conductivity data from the wells. An average formation factor of 10.7 is estimated with a standard deviation of 1.81. However, this estimated formation factor is obtained from a single measurement in three Wells and

further research is needed to determine the accuracy of the value. The results of the EM survey showed, the apparent conductivity measurements systematically increased during the dry season of 2016, in the Seven Palm system. The general increase in the salinity reflects a decreased precipitation, increased evapotranspiration, and the influence of saline water from Florida Bay on the surface and groundwater. The spatial salinity variation on the lakes showed west to east increase in surface water salinity and a West to East decrease in groundwater salinity. In addition, the salinity of the surface water and groundwater increased from North to South and suggest freshening of the groundwater and may reflect the effects of increased flow due to restoration efforts. Based on this study, the floating electrical resistivity and EM methods can characterize the subsurface formation resistivity effectively and recommend further study to assess the temporal change of the groundwater chemistry.

5.1. Introduction

During the past century, the Everglades National Park (ENP) has been adversely impacted by past human activities that have altered the flow of fresh water through the system. Moreover, the highly permeable limestone aquifers bounded by the ocean and brackish estuaries to the south are highly susceptible to saltwater intrusion (SWI). In the 1950^{s} the U.S. Army Corps of Engineers developed canals, levees, and water conservation areas for flood protection. Even though this development plan has succeeded in controlling floods, South Florida does not receive sufficient quantity and distribution of water which results in ecosystem degradation. In 2000, Congress authorized the Comprehensive Everglades Restoration Plan (CERP) to restore, preserve, and protect the South Florida

ecosystem. The CERP makes an effort to restore the quantity, quality, timing, and distribution of water in the region. Major activities of the CERP, such as the raising of Tamiami Trail and construction of the C-111 Spreader Canal Project are expected to increase the flow of freshwater and modify the groundwater chemistry in the ENP.

Freshwater input to the ENP comes from direct rainfall and inflow from Lake Okeechobee across the water conservation area (WCA) reservoirs. The two main flow drainage inputs in ENP are the Shark River Slough (SRS) and Taylor Slough (TS). The Mangrove Lake region receives freshwater inflow from TS. Salinity in the Florida Bay varies in time and space and governed by the influence of precipitation, evapotranspiration, runoff, and mass exchange with the surrounding basins (Kelble et al. 2007). Evapotranspiration rates are high in this region and affect the freshwater input balance negatively (Dessu et al. 2018). The author also suggests freshwater inflow is critical to compensate for the net loss.

The degree of saltwater intrusion along the coast varies widely and is affected by the hydroclimate variability, hydrogeological setting, history of groundwater development, and sources of saline water within a particular area (Barlow 2003). Under natural conditions, the seaward flow of freshwater prevents saltwater from encroaching coastal aquifers. However, in comparison with the historical flow of freshwater, the flow of fresh water through the Everglades has been reduced by approximately 70 %. Due to this, the quality of the water is degraded and caused the salinity of the surface water to be between 20 to 30 PSU (McIvor et al. 1994). This reduced historical flow of freshwater input to the Florida Bay followed by drought in South Florida between 2014 to 2015 produced substantial die-offs of the seagrass (NPS 2015; Kelble et al. 2007).

Geophysical methods have been developed to identify and map the lateral and vertical distribution of shallow freshwater and saline water interface. These methods provide powerful tools to identify the position of saline or brackish water in an aquifer (Jansen, 2011). Electrical resistivity and electromagnetic (EM) are the most commonly used geophysical methods to study saltwater intrusion. Conventionally, mapping of saltwater intrusion in coastal aquifers has been conducted by collecting water samples from wells. Even though this approach provides reliable results, it is restricted to the existing and accessible wells. Moreover, it gives discrete information, which doesn't represent the overall spatial distribution of the area. As a result of this, the majority of the work depends on interpolation and extrapolation of the data and this leads the result to become less reliable. In addition, it is difficult to get permission to install wells in the Everglades National Park (ENP). The difficulty to get permission to install wells in the Everglades National Park and the advantage that the floating electrical resistivity array and EMP 400 Profiler are portable and don't require contact with the ground make an integrated approach of floating electrical resistivity and EM survey a better alternative to study Everglades National Park.

Electrical resistivity and EM are rapid and noninvasive geophysical methods for measuring groundwater properties and characterizing the spatial and temporal variability of subsurface formations. Electrical resistivity has an advantage because the non-uniqueness of the resistivity method is less compared with other geophysical methods such as electromagnetic methods. The electrical resistivity method is superior for imaging the electrical resistivity structure compared to other non-invasive geophysical imaging techniques. DC resistivity offers several advantages over EM methods because the array is

in direct galvanic contact with the water or earth and is not affected by external magnetic fields and nearby conducting bodies such as the boat and operator. The EM method provides a faster alternative to DC soundings (Corriols et al. 2009) and it is possible to record detailed information even in areas where accessibility is a major concern. But it is sensitive to electromagnetic noise produced by metals, pipelines, etc. Therefore, the DC resistivity sounding remains the gold standard to characterize subsurface formations.

This study investigated the spatial and temporal changes in the groundwater chemistry in the Mangrove Lakes of ENP using electrical resistivity, EM methods, surface water, and groundwater sampling. The EM survey was conducted from 2014 to 2017 in the Mangrove Lakes of ENP using the GSSI EMP-400 Profiler multi-frequency EM conductivity meter (https://www.geophysical. com/products/ profiler-emp-400) deployed in a flat-bottomed plastic kayak towed behind a small boat integrated with a GPS receiver. In addition, an electrical resistivity survey was conducted in July 2019 using a floating 14 electrode array using Advanced Geosciences Inc (AGI) Super Sting R1 IP meter (https://www.agiusa.com/supersting-wifi). Finally, groundwater specific conductivity measurements collected at four continuously monitored shallow wells on the shorelines of the lakes were compared to nearby inverted lake bottom resistivity to calculate a formation factor for the Lakes region. This formation factor was used to convert the inverted formation resistivity to groundwater resistivity and produce a regional map of groundwater salinity.

This paper aims to present the changes in surface and groundwater chemistry in Alligator Creek (West Lake) and McCormick Creek (Seven Palm) using EM surveys conducted during the dry season of 2016 and the seasonal change between 2016 to 2017. In addition, this paper presents the spatial change in surface and groundwater chemistry

using the floating Dipole-dipole electrical resistivity survey conducted in July 2029 and produced a regional map of groundwater salinity.

5.2. Previous Studies

Different studies showed that the application of a combination of DC resistivity and EM methods provide detailed information about the sub-surface formations. Integrated approaches of EM, electrical resistivity, and well data are the most effective technique to estimate a formation factor (Greenwood et al. 2006), which used to produce a regional map of groundwater salinity. The formation factor can be determined by coincident measurements of groundwater and formation conductivity or from empirical relationships such as Archie's Law (Archie 1942). Greenwood et al. (2006) conducted an integrated approach of EM and electrical resistivity on the wetland of Tampa Bay, Florida, and suggested that an effective technique to map pore water conductivities is to compute formation factor from resistivity surveys and pore water samples.

The study conducted by Fitterman and Prinos (2011) estimated a formation factor of 5.1 by comparing EM induction logs and water samples from wells in eastern Miami-Dade County. Similarly, in other studies, Fitterman et al. (1999) estimated a formation factor of 8.1 in Everglades National Park using similar methods and Tucker (2013) estimated a formation factor of 9.8 for Big Pine Key using ERT and water samples from wells. Formation factor depends on several parameters such as porosity, the degree of saturation, cementation, and pore fluid resistivity and heterogeneity.

Integrated approaches of electromagnetic using a floating EM-34 and EM-31instruments from Geonics Ltd and direct current resistivity were applied in the coastal

wetland on Tampa Bay, Florida (Greenwood et al. 2006). The authors mentioned the results obtained using EM-31 estimated a reasonable seabed conductivity. In another study, Mansoor et al. (2006) used a terrain-conductivity EM-31 in shallow water wetlands of Kearny Marsh, New Jersey, and characterized contamination of leachates from adjacent landfills to the marsh and/or residual effect of a past tidal connection. EM methods have been used for imaging saltwater intrusion in coastal aquifers, seaside groundwater basin, California (Nenna et al. 2013) and also used EMP 400 profiler to characterize the chemical properties of soil in Sidrolandia, MS, Brazil (Machad et al. 2015).

Several studies have been conducted in the ENP to assess the freshwater and saltwater interaction. A study conducted in the southern ENP (Fitterman and Deszcs-Pan 1998) aimed to assess saltwater intrusion and prepared a subsurface resistivity map using airborne frequency-domain electromagnetic (FDEM) method and borehole geophysical measurements. They concluded that EM methods are effective and provided a baseline for further detailed study (Fitterman and Deszcs-Pan 1998). In 2011, a time-domain electromagnetic (TDEM) method was conducted in Miami Dade county and delineated the freshwater and saltwater interface (Fitterman and Prinos 2011; Fitterman 2014). Recently, ongoing studies of hydrochemical conditions (Allen et al. 2016) and electromagnetic survey (Whitman et al. 2016; Kiflai et al. 2017) in mangrove Lake drainage systems of ENP showed the conductivity (salinity) of the surface water and groundwater increased during the dry season (February to April 2016) and decreased between 2016 to 2017. The limitation of the study is the EMP 400 instrument has a calibration problem and made it difficult to characterize the groundwater and surface water conductivity quantitatively. Hence, a qualitative description of the EM survey is provided in this study.

5.3. Data and Methods of Analysis

5.3.1. Data Collection

A GSSI Profiler EMP-400 multi-frequency EM conductivity meter was deployed in a flat-bottomed plastic kayak towed behind a small boat (Figure 5.2). The instrument is calibrated at the GSSI factory by suspending it well above the ground and zeroing the field values. In addition, before data acquisition, field calibration was performed on-site. This field calibration procedure removes any electromagnetic effects of the operator and other equipment in the surrounding area. The EM data were recorded at frequencies of 1, 4, and 16 KHz, and the coils were oriented in vertical dipole moment (VDM) with a sample interval of 2-seconds. The electromagnetic survey was conducted in West Lake and Seven Palm from August 2013 to February 2017 (Figure 5.1a). Overall, in the Mangrove Lake region, nine surveys have been performed successfully along the transect line (Table 5.1). The field survey dates were planned to assess the seasonal variability in conductivity between the wet and dry season. Coincident EM and DC resistivity measurements were planned, however, due to the failure of the EM instrument due to calibration, we were unable to collect data (Table 5.1).

A floating Dipole-dipole 14 electrode vertical electrical sounding (VES) array was deployed by boat in the Seven Palm and West Lake systems on July 10 and 15, 2019 in the mangrove lakes of ENP (Figure 5.1b). In the Dipole-dipole array, 48 measurements were recorded, with 1-meter and 2-meter dipole length. Thirty-two measurements were recorded with 1-meter dipole length at a spacing ranging from 1 to 11 m. and 16 measurements were recorded with 2-meter dipole length at a spacing of 2, 4, 6, and 8 m. However, the 16

measurements recorded with 2-meter dipole length were not modeled because the software only supports inverting data measured at one dipole length. The measurements included reciprocal measurements where the current and potential electrode pairs are exchanged. These reciprocal measurements provide redundancy and the ability to estimate measurement uncertainty. Foam noodles were used between the electrodes in order to float the array In the analysis, the average value of the measurements with 1-meter dipole length and its reciprocal were used.

In West Lake, Cuthbert Lake, Long Lake, and Seven Palm Lake Aqua Troll 200 data logger monitoring wells were installed in 2014 (Allen and Price, 2015; Figure 5.1), In the monitoring wells, the depth of the water level, temperature and specific conductivity of the surface water and groundwater were recorded. Coincident conductivity measurement recorded in the Wells and the floating Dipole-dipole electrical resistivity array in July 2019 were used to estimate the formation factor. During the EM survey, at different localities and different intervals of time, the surface water conductivity, temperature, Ph, and salinity were recorded with the help of a water quality YSI probe. These field measurements were repeated at the electrical resistivity measurement sites and listed in Appendix 5A. In addition to that, the depth of the water was measured using a sonar transducer and a calibrated rod during the EM survey, and the depth of the water column was measured using a calibrated rod during the electrical resistivity survey.

5.3.2. Data Analysis

In FDEM methods, the data of interest is in the in-phase (real), and quadrature (imaginary) field ratio components. Apparent conductivity was calculated using the

quadrature component. from the general equation given by (Keller and Frischknecht 1966; McNeill 1980) for a homogeneous half-space model. The calculated apparent conductivity is used to assess the spatial and temporal change during the dry season of 2016 and the change between 2016 to 2017 in the Mangrove Lakes. The apparent conductivity change map between 2016 to 2017 is produced by spatially joining the EM data to the nearest location. The depth penetration of the data is related to the input frequency. The higher frequencies (e.g. 16 KHz) have shallow penetration and represent the conductivity of the surface water. The lower frequency (e.g. 4 and 1 KHz) data have deeper penetration and reflect an average of the conductivity of the surface water and groundwater.

The choppy water pitches and rolls the instrument and this produces noise in the EM data. First, the outliers in the data greater than three standard deviations along 1 KHz, 4 KHz, and 16 KHz were removed. Then, a moving average convolution filtering technique was applied to smooth the data using the nearest 100 data. For example, Figure 5.3, represents an example of the data reduction and smoothing in Seven Palm System in April 2016. The data reduction and smoothing for all the dataset is summarized in Table 5.2.

The EM data were inverted into a two-layer model that represents the surface water and lake bottom (groundwater saturated) layer. The water depth values were obtained by regression analysis of the continuously measured water depth using a sonar transducer and a calibrated rod. The water depth measured using the calibrated rod and the surface water conductivity measured using the water quality YSI probe were take at several locations along the profile line. The conductivity of the surface water measured using the YSI probe was interpolated using kriging interpolation techniques in GIS. Then, the conductivity of the surface water was extracted along the EM profile line. The inverted EM model is higher

than the measured data in the Wells, which may be due to the static shift of the EM instrument during calibration. Hence, a qualitative description of the apparent conductivity is presented in this study.

The VES data were inverted to a two-layer model by constraining the depth and resistivity of the water column measured with a calibrated rod and YSI probe in IX1D V3 software (http://www.inter pex.com/ix1dv3/ix1dv3.htm). Thus, the VES data is inverted only for the seabed conductivity (lake bottom). In the Seven Palm system, on July 10, 2019, high winds caused considerable chop in the water which made work difficult and required modification of the float system for the cable. Due to the poor field conditions, the data collected was noisy and thus specific outlier measurements associated with the larger spacing (n = 10 and 11) were masked. In the inversion, the average value of the measurements and its reciprocal were used. Water depth in the model was constrained to a rod measurement at the array center, but the water layer and lake bottom layer resistivity were left unconstrained in the inversion. See the discussion in Chapter Four of this dissertation for details about constrained water depth inversion. Finally, the inverted resistivity was converted to salinity using the general equation given by (Wagner 2006).

In the Mangrove Lakes, the formation factor is estimated using the bulk resistivity measured by the floating Dipole-dipole array and coincident conductivity data measured using Aqua troll 200 transducers in the wells. From these Wells, the Dipole-dipole sounding data recorded at a distance of 68 m in West Lake, 41 m in Seven Palm, 48 m in Cuthbert Lake, and 807 m in Long Lake were used to calculate the formation factor. The average conductivity (µS/cm) measurement in the wells of in the day was converted to resistivity, where the resistivity (Ω·m) = 10000/ Conductivity water (µS/cm). Then, the

formation factor was calculated from the average value of the ratio of bulk resistivity modeled from the geophysical data and the pore water resistivity measured in the shallow groundwater wells. This estimated formation factor was used to produce a regional map of groundwater salinity.

5.4. Results

5.4.1. Electromagnetism

The EM data were recorded at frequencies of 1, 4, and 16 KHz. The depth penetration of the data is related to the input frequency. The higher frequencies (e.g. 16 KHz) represent the conductivity of the surface water and the lower frequency (e.g. 4 and 1 KHz) reflects an average of the conductivity of the surface water and groundwater. In this section, we present apparent conductivity changes during the 2016 dry season in Seven Palm and changes between 2016 and 2017 in West Lake and Seven Palm systems.

I. Changes during the 2016 Dry Season in the Seven Palm system

In the Seven Palm system at monthly intervals during the 2016 dry season, the apparent conductivity measurements systematically increase from February to April, 2016 (Figure 5.4). The 1 KHz apparent conductivity ranged from 800 mS/m at the northern end of Seven Palm Lake to 1400 mS/m in the southern end in February 2016, whereas in April 2016 it ranged from 930 to 2150 mS/m. Similarly, the apparent conductivity along 4 KHz range from 900 to 1500 mS/m in February 2016 to a range of 1000 to 2800 mS/m in April 2016 (Figure 5.4). This showed the apparent conductivities increased from north to south at all frequencies. In addition, for example, in northwest Seven Palm Lake, the 1 KHz apparent conductivities increase from around 800 mS/m in February to around 1070 mS/m

in March to over 1100 mS/m in April. In Middle Lake, the apparent conductivities increased from around 1500 mS/m in February to 1700 mS/m in March to over 1800 mS/m in April. In Monroe Lake, it increased from around 2300 mS/m in March to over 2500 in April.

The apparent conductivity of the 16 KHz data varies from 1100 to 2000 mS/m in February 2016 and from 1200 to 2400 mS/m in March 2016 and from 1400 to 3200 mS/m in April 2016 from North to South along the profile line. This is consistent with the increase in conductivity and salinity measured in the surface probe measurements (Figure 5.7). This indicates a general increase in apparent conductivities (salinity) in the surface water over the dry season and from North to South along the profile line.

II. Changes between 2016 and 2017 in the Mangrove Lakes

The EM data shows a considerable decrease in apparent conductivity between February 2016 and January 2017 in both the Seven Palm and West Lake system. In McCormick Creek, the apparent conductivity showed a constant decrease of 150 mS/m in the Seven Palm system and 300 mS/m in the Middle lake (Figure 5.5). In the McCormick Creek system, the 1 KHz apparent conductivity ranged from 800 mS/m at the northern end of Seven Palm Lake to 1400 mS/m in southern end in February 2016, (Figure 5.5a) whereas in January 2017 it ranged from 740 to 1200 mS/m (Figure 5.5b). Similarly, the apparent conductivity along 4 KHz range from 870 to 4000 mS/m in 2016 (Figure 5.6a) to a range of 800 to 2400 mS/m in 2017 (Figure 5.6b).

The EM results show the same trend in the Alligator Creek System. The apparent conductivity of the 1 KHz data decreases from a range of 1200 to 1700 mS/m in 2016 to 950 to 1850 mS/m in 2017 (Figure 5.5). In addition to that, the result along 4 KHz and 16

KHz dropped from 1600 mS/m to 1500 mS/m and from 1800 mS/m to 1600 mS/m respectively (Figure 5.6 and Figure 5.7). In the West Lake system in January 2016, the highest apparent conductivities (2000 mS/m) were seen at the eastern end of the Long Lake and southern West Lake with the lowest conductivities in northern Cuthbert Lake.

The apparent conductivity change between 2016 to 2017 in the Seven Palm system is more significant than the West Lake system. The apparent conductivity change between 2017 to 2016, at all frequencies, decreased on average 30 % in the Seven Palm system and 10 % in the West Lake system (Figure 5.8). In Seven Palm, the apparent conductivity change decreased 20 % at the northern end of Seven Palm Lake near the well to 30 % in the southern end and clearly showed the trend from North to South. However, at the northern tip of Seven Palm, there is an increase of 30 to 40 %. Similarly, in the West Lake system, there is a gradual change from North to South and a significant change of 30 % observed on the northern tip of Long Lake. In addition, the apparent conductivity change of the surface water is significant compared to the groundwater. For example, near the well at 1 KHz, 4 KHz, and 16 KHz, the apparent conductivity change decreased by 18 %, 21 %, and 26 % respectively. In general, in the Mangrove Lakes, the decrease in apparent conductivity change is pronounced from West to East at all frequencies.

5.4.2. Electrical Resistivity

The resistivity data collected on July 10, 2019, in Seven Palm and on July 15, 2019, in West Lake were inverted to 2-layer constrained water depth model. The inverse model of each VES is presented in Appendix 5A. In this section, we focus on the spatial change in groundwater and surface water. The resistivity of the surface water measured using the

YSI probe and the inverted models showed a similar result. The resistivity varies between 0.37 Ω·m on the West to 0.27 Ω·m on the East. In the Seven Palm system, the resistivity varies from 0.27 Ω·m on the North to 0.17 Ω·m on the South (Figure 5.10a). Similarly, the inverted surface water resistivity varies between 0.29 Ω·m on the West to 0.22 Ω·m on the East. In the Seven Palm system, the resistivity varies from 0.23 Ω·m on the North to 0.16 Ω·m on the South (Figure 5.10b). Generally, the data showed west to east and north to south decrease in surface water resistivity.

The Lake bottom resistivity varies between 1.69 Ω·m on the West to 32. 85 Ω·m on the East. In the Seven Palm system, the resistivity is 32.85 Ω·m in the north and decreases gradually towards south to 1. 5 Ω·m (Figure 5.10c). The lake bottom resistivity generally showed a West to East increase in resistivity and north to South decrease in resistivity.

In the inverse model, the minimum and maximum lake bottom resistivity varied between 1.4 Ω·m to 3.7 Ω·m in Westlake and between 1.4 Ω·m to 32.8 Ω·m in Seven Palm. Based on equivalency analysis, in West Lake, the model showed a highly constrained model with the lower and upper limit between 1.1 Ω·m to 4.9 Ω·m (Figure 5.11), whereas in Seven Palm the model showed poorly constrained model with the lower and upper limit between 1.4 Ω·m to 362 Ω·m (Figure 5.11). This model is poorly constrained mainly on the upper bound. The lower and upper limits in West Lake are highly constrained compared with Seven Palm System (Figure 5.11). This uncertainty on the upper bound could be due to measurement errors induced by boat navigation, wind, or wave action.

5.4.3. Salinity

A formation factor in the Lakes is estimated by dividing the groundwater resistivity (ρ_w) measured in the shallow groundwater wells into the lake bottom resistivity (ρ_f) modeled from the geophysical data. In this study, the data collected on July 15, 2019, in the West Lake system was used to calculate a formation factor for the mangrove Lakes. An average formation factor in the Mangrove Lakes is estimated 10.7 with a standard deviation of 1.81. This estimated formation factor is calculated from the average formation factor of West Lake, Long Lake, and Cuthbert Lake (Table 5.3). The formation factor of Seven Palm was not considered in the calculation as the resistivity of the model was poorly constrained due to the noise in the data. This estimated formation factor (10.7) is slightly higher to previously published estimates for the ENP (Fitterman et al. 1999).

The surface water salinity measured using the YSI probe varies from 15 PSU in the West to 21 PSU in the East (Figure 5.12a). In the Seven Palm system, the salinity varies from 21 PSU in the North to 33 PSU in the South. The inverted surface water salinity has the same trend and increased from 19 PSU to 27 PSU from West to East and from 27 PSU to 35 PSU from North to South (Figure 5.12b). In contrast, the inverted groundwater salinity decreased from 42 PSU in the West to 2 PSU in the East. In the Seven Palm system, the salinity increased from 2 PSU in the North to 49 PSU in the South (Figure 5.12c). The data showed west to east increase in surface water salinity and a West to East decrease in groundwater salinity.

5.5. Discussion

In the Everglades, precipitation and evapotranspiration varies seasonally and affects the southward flow of freshwater input in the aquifer. A study conducted in the Florida bay, between 1998 to 2004, by Kelble et al. (2007) showed the surface water mean monthly salinity was minimum in January and maximum in July. The author mentioned the seasonal salinity patterns in Florida Bay are directly related to the seasonal climatic variability. In the study area, at the NCL station, between February to April 2016, the daily median water level data decreased from 0.6 feet to less than 0 feet NAVD88 and the total daily evapotranspiration increased from 1 mm to 5 mm (Figure 5.9). During this dry season of 2016, the EM result indicates that the apparent conductivity increased in the Seven Palm system. This change is in response to decreased precipitation, increased evapotranspiration, and southward flow and reflects a general increase in apparent conductivities (salinity) in the surface water and groundwater over the dry season.

In the Florida bay, a study conducted between 2017 to 2016 documented, the surface water salinities were notably lower in 2017 than in 2016 (Madden et al. 2018). The authors suggested the historic drought occurred in 2015, associated with high temperature and low rainfall event recorded in 2016 caused lower freshwater inputs than average into the bay. However, the salinity decreased in October 2016, due to high rainfall event recorded in August 2016 (Figure 5.9) and freshwater inputs into the bay. In this study, the EM result shows a considerable decrease in apparent conductivity between February 2016 and January 2017 in both the Seven Palm and West Lake system. In the Seven Palm system, the apparent conductivity (salinity) decreased from north to south at all frequencies. These

changes suggest a freshening of the surface water and groundwater and may reflect the effects of increased flow due to restoration efforts.

Between 2017 to 2016, the apparent conductivity change decreased on average 30 % in the Seven Palm system and 10 % in the West Lake system. These apparent conductivity change at all frequencies (surface and ground water), suggests the restoration efforts may have made a positive contribution in the Seven Palm system but not yet in the West Lake system. The fact that the Seven Palm system is close to the Taylor Slough, the change observed can be a reflection of the C-111 spreader canal western project that reduce water loss from Taylor Slough and increase freshwater flow to the Lake and Florida Bay. Furthermore, the apparent conductivity change of the surface water (16 KHz) is significant compared to the groundwater (1 KHz). This indicates the surface water apparent conductivity (salinity) is more temporally variable than the groundwater apparent conductivity (salinity). This shows that surface water salinity in south Florida is highly dependent on the climatic variability.

Some limitation of the EM study was for a portion of the EM measurements at coincident locations, certain measurement were different. This difference could be due to instrument drift, the operator changing position during the survey that affects the position of the coils, and the calibration problem after Bluetooth connection failure, which caused a new calibration in different environmental settings.

For the electrical resistivity soundings collected in 2019, the resistivity of the surface water measured using the YSI probe (Figure 5.10a) was generally consistent with the inverted models (Figure 5.10b). This indicates that the modeling technique is well-calibrated and that the inverted lake water resistivity accurately represents the actual

conditions. The regional pattern shows a general East to West and a South to North *increase* in resistivity consistent with a general freshening of the lake water in those directions. In contrast, lake bottom resistivity shows an East to West *decrease* in resistivity which suggests that the groundwater increases in salinity in that direction (Figure 5.10c). These results suggest the floating electrical resistivity array can map the resistivity of the subsurface formation effectively.

When the modeled resistivity is converted to salinity, the surface water salinity showed a general increase from north to south and from west to east (Figure 12a and 12 b). In contrast, the groundwater salinity decreased from west to east and increased from north to south (Figure 12c). In the Everglades Lakes, surface water salinity is driven by seasonally variable winds and evaporation whereas groundwater salinity is less temporally variable and reflects regional groundwater flow. A study conducted in two small estuaries in Cape Cod, USA indicates a large variation in salinity due to the influence of strong wind (Geyer 1996). The study demonstrated onshore winds reduce the flushing rate and increase the salinity gradient along the estuary. In contrast, offshore winds enhance surface outflow and decrease the salinity gradient (Geyer 1996).

In West Lake, the less saline surface water overlies over the more saline groundwater. In contrast, the more saline surface water overlies the less saline groundwater in Seven Palm Lake. This inverted salinity profile in Seven Palm Lake is gravitationally unstable and likely has a profound effect on recharge and discharge mechanisms to and from the aquifer.

An average formation factor in the Mangrove Lakes is estimated 10.7 with a standard deviation of 1.81. The previously conducted work estimated a formation factor 5.1 in

eastern Miami-Dade County (Fitterman and Prinos 2011), 8.1 in eastern Everglades National Park (Fitterman et al. 1999), 9.6 in southern Everglades National Park (Fitterman and Deszcz-Pan 1998), and 9.8 in Big Pine Key (Tucker 2013). The estimated formation factor 10.7 in this study is slightly higher to previously published estimates for the ENP. In the mangrove Lakes, the shallow wells only extended to the base of the peat layer and did not penetrate the underlying limestone. This method assumes that the groundwater sampled from the wells is derived from the underlying limestone. The estimated formation factor is obtained from three measurements in the nearby Wells. Hence, repeated measurements are required to determine the accuracy of the estimated formation factor value. We used the estimated formation factor 10.7 on this study to calculate the salinity of the groundwater. This approach has the advantage of forcing the geophysics derived salinities to be consistent with the in-situ well measurements.

5.6. Conclusions

The Geophysical methods can map the difference in conductivities (salinity) of a subsurface formation effectively. The results of the EM survey shows the apparent conductivity measurements systematically increased from February to April 2016, in the Seven Palm system. This demonstrates how the salinity of the groundwater changes during the dry season. The general increase in the salinity reflects a decreased precipitation, increased evapotranspiration, and the influence of saline water from Florida Bay on the surface and groundwater. The apparent conductivity showed a considerable decrease between February 2016 and January 2017 in both the West Lake and Seven Palm system. These changes suggest a freshening of the groundwater and may reflect the effects of

increased flow due to restoration efforts. Furthermore, the apparent conductivity change between 2016 to 2017, is more pronounced in Seven Palm than the West Lake system. This suggests the restoration efforts may have made a positive contribution to the Seven Palm system but not yet in the West Lake system.

The floating resistivity survey efficiently characterizes the spatial variations in surface water groundwater salinity. In general, both the surface water and the groundwater increase in salinity from North to South. In contrast, the surface water salinity increased from West to East while the groundwater salinity decreased from West to East. We estimated a formation factor of 10.7 for the mangrove Lakes of ENP. This estimated formation factor is slightly higher from the average regional formation factor of 8.1 estimated in other studies. The fact that the formation factor is obtained from a single measurement may limit the finding of the salinity value in the mangrove lakes. Hence, a further research study is needed to determine the accuracy of the estimated formation factor. Another limitation of this study could be the groundwater wells are situated approximately (1 m) deep and may not represent the deeper groundwater.

5.7. References

AGIUSA. (2019). SuperSting™ Wi-Fi. Retrieved July 30, 2019, from agiusa.com website: https://www.agiusa.com/supersting-wifi.

Allen, J.M., and R.M. Price. (2015). Hydrologic Conditions in West and Seven Palm Lake Drainage Systems in the Florida Everglades. 2015 LTER All Scientists Meeting, Estes Park, Colorado, August 30-02, 2015.

Allen, J. M., Price, R. M., Frankovich, T. A., Whitman, D., and Fourqurean, J. W. (2016). Hydrologic and nutrient condition in West and Seven Palm Lake drainages in the Florida Everglades. Presented at the GSA Annual Meeting, Denver, Colorado, USA. https://doi.org/10.1130/abs/2016am-287882.

Archie, G. E. (1942). The electrical resistivity log as an aid in determining some reservoir characteristics. *Transactions of the AIME, 146*(01), 54–62.

Barlow, P. M. (2003). Groundwater in freshwater-saltwater environments of the Atlantic Coast. *United State Geological Survey* (USGS).(Vol 1262).

Corriols, M., Ryom Nielsen, M., Dahlin, T., and Christensen, N. B. (2009). Aquifer investigations in the León-Chinandega plains, Nicaragua, using electromagnetic and electrical methods. *Near Surface Geophysics*, *7*(5-6), 413-426.

Dessu, S. B., Price, R. M., Troxler, T. G., and Kominoski, J. S. (2018). Effects of sea-level rise and freshwater management on long-term water levels and water quality in the Florida Coastal Everglades. *Journal of Environmental Management, 211*, 164–176.

Kelble, C. R., Johns, E. M., Nuttle, W. K., Lee, T. N., Smith, R. H., and Ortner, P. B. (2007). Salinity patterns of Florida Bay. *Estuarine, Coastal and Shelf Science*, *71*(1-2), 318-334.

Keller, G. V., and Frischknecht, F. C. (1966). Electrical methods in geophysical prospecting.

Fitterman, D. V. (2014). Mapping Saltwater Intrusion in the Biscayne Aquifer, Miami-Dade County, Florida using Transient Electromagnetic Sounding. *Journal of Environmental & Engineering Geophysics*, *19*(1), 33–43.

Fitterman, D. V., and Deszcz-Pan, M. (1998). Helicopter EM mapping of saltwater intrusion in Everglades National Park, Florida. *Exploration Geophysics*, *29*(2), 240–243.

Fitterman, D.V., Deszcz-Pan, M., and Stoddard, C.E., 1999, Results of time-domain electromagnetic soundings in Everglades National Park, Florida (on CD–ROM): U.S. Geological Survey Open-File Report 99–426, 152 p.

Fitterman, D.V., and Prinos, S.T., 2011, Results of time-domain electromagnetic soundings in Miami-Dade and southern Broward Counties, Florida: U.S. Geological Survey Open-File Report 2011–1299, 289 p.

Geyer, W. R. (1997). Influence of wind on dynamics and flushing of shallow estuaries. *Estuarine, coastal and shelf science*, *44*(6), 713-722.

Greenwood, W. J., Kruse, S., and Swarzenski, P. (2006). Extending electromagnetic methods to map coastal pore water salinities. *Ground Water*, *44*(2), 292–299.

Jansen, J. R. (2011). Geophysical Methods to Map Brackish and Saline Water in Aquifers. *Proceedings of the 2011 Georgia Water Resources Conference*. Retrieved from http://smartech.gatech.edu/handle/1853/46031.

Kiflai, M. E., Whitman, D., Price, R., Frankovich, T., and Allen, J. (2017). Geophysical Characterization Of Groundwater in the Mangrove Lakes Region of Everglades National Park. *AGUFM*, *2017*, NS13B-0021.

Machado, F. C., Montanari, R., Shiratsuchi, L. S., Lovera, L. H., and Lima, E. de S. (2015). Spatial Dependence of Electrical Conductivity and Chemical Properties of the Soil By Electromagnetic Induction. *Revista Brasileira de Ciência Do Solo*, *39*(4), 1112–1120.

Madden, C.J., Strazisar, T., Stachelek, J. (2018). Synoptic Ecological Mapping in Florida Bay. South Florida Environmental Report (SFER) – The Florida Bay Project: Water Quality Conditions and Status https://www.sfwmd.gov/our-work/florida-bay

Mansoor, N., Slater, L., Artigas, F., and Auken, E. (2006). High-resolution geophysical characterization of shallow-water wetlands. *Geophysics*, *71*(4), B101-B109.

McNeill, J. D. (1980). Electromagnetic terrain conductivity measurement at low induction numbers.

Nenna, V., Herckenrath, D., Knight, R., Odlum, N., and Mcphee, D. (2013). Application and evaluation of electromagnetic methods for imaging saltwater intrusion in coastal aquifers : Seaside Groundwater Basin , California. *Geophysics*, *78*(2), B77–B88.

McIvor, C. C., Ley, J. A., and Bjork, R. D. (1994). Changes in freshwater inflow from the Everglades to Florida Bay including effects on biota and biotic processes: a review. *Everglades: The ecosystem and its restoration*, 117-146.

NPS gov (2015). Florida Bay Seagrass Die-Off National Park Service, *U.S. Department of the Interior, South Florida Natural Resources Center Everglades National Park.* https://www.nps.gov/ever/learn/nature/upload/seagrassDieoff_final_web_hi_res.pdf

Wagner, R. J., Boulger, R. W., Jr., Oblinger, C. J., and Smith, B. A. (2006). *Guidelines and standard procedures for continuous water-quality monitors: station operation, record computation, and data reporting* (Vol. 1–D3). U.S. Geological Survey.

Whitman, D., Price, R. M., and Frankovich, T. A. (2016). Electromagnetic Surveying in the Mangrove Lakes Region of Everglades National Park. In *National Conference on Ecosystem Restoration (NCER),* Coral Spring, FL.

Tucker, N. M. (2013). Analyzing tidal fluctuations in the Big Pine Key freshwater lens with time-lapse resistivity (Florida International University). https://doi.org/10.25148/etd.FI13080512

Table 5.1: This table shows the EM Survey dates where data was collected (✓).

Year	**2013**	**2014**	**2016**				**2017**	
Month	Aug	May	Jan	Feb	Mar	Apr	Jan	Feb
West Lake	✓	✓	✓					✓
Seven Palm		✓		✓	✓	✓	✓	

Table 5.2: Data reduction and smoothing: Column (1) represents the sample number, EM data less than 3 standard deviations, and the second filter of EM data less than 3 standard deviations and smoothing 100 consequent samples.

No	**Date**	**EM Observed Data**	**EM Data < 3 std**	**EM Data < 3 std and Convolution**	**Data Removed**
1	**EM_021017_WL**	6248	6176	6077	171
2	**EM_012516_WL**	8923	8899	8872	51
3	**EM_012017_SP**	5709	5709	5709	0
4	**EM_022016_SP**	4012	4010	3998	14
5	**EM_031716_SP**	6380	6357	6346	34
6	**EM_040616_SP**	4710	4659	4555	155

Table 5.3: Formation factor in the Mangrove Lakes of Everglades national park

Site	Date	Distance from well (m)	Well Data		Geophysical Model		***F*ormation Factor** $F = \frac{\rho_f}{\rho_w}$
			Surface water	**Ground water** ρ_w	**Surface water**	**Lake bottom** ρ_f	
West Lake	7/15/2019	68	0.32	0.26	0.29	3.23	12.6
Long Lake	7/15/2019	807	0.19	0.20	0.14	2.11	10.6
Cuthbert Lake	7/15/2019	48	0.28	0.31	0.27	2.77	9.0
Seven Palm	7/10/2019	41	0.23	1.12	0.22	32.85	*29.41*

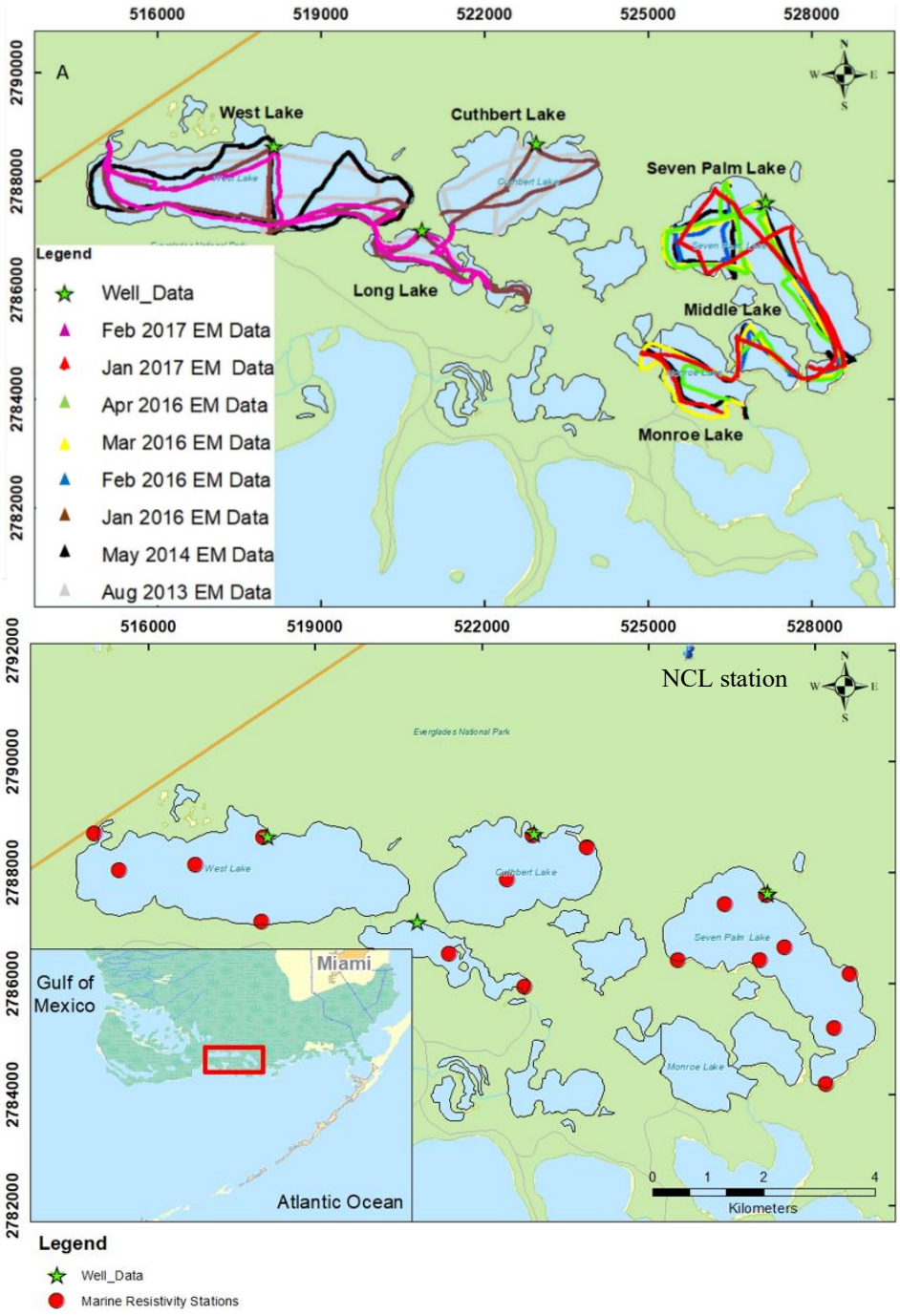

Figure 5.1: Mangrove Lake region of ENP and the location of the well stations, and geophysical survey (a) EM surveys (b) floating electrical resistivity soundings. The blue pin showing location of the NCL gage station.

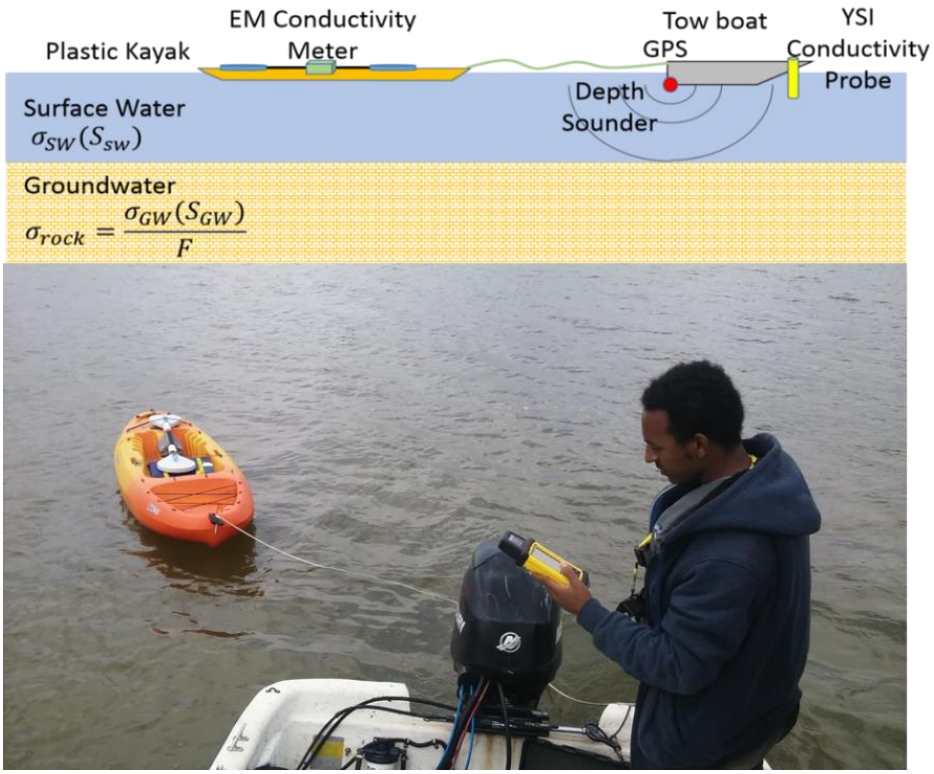

Figure 5.2: EM Experimental set up in Seven Palm Lake, Everglades National Park, FL.

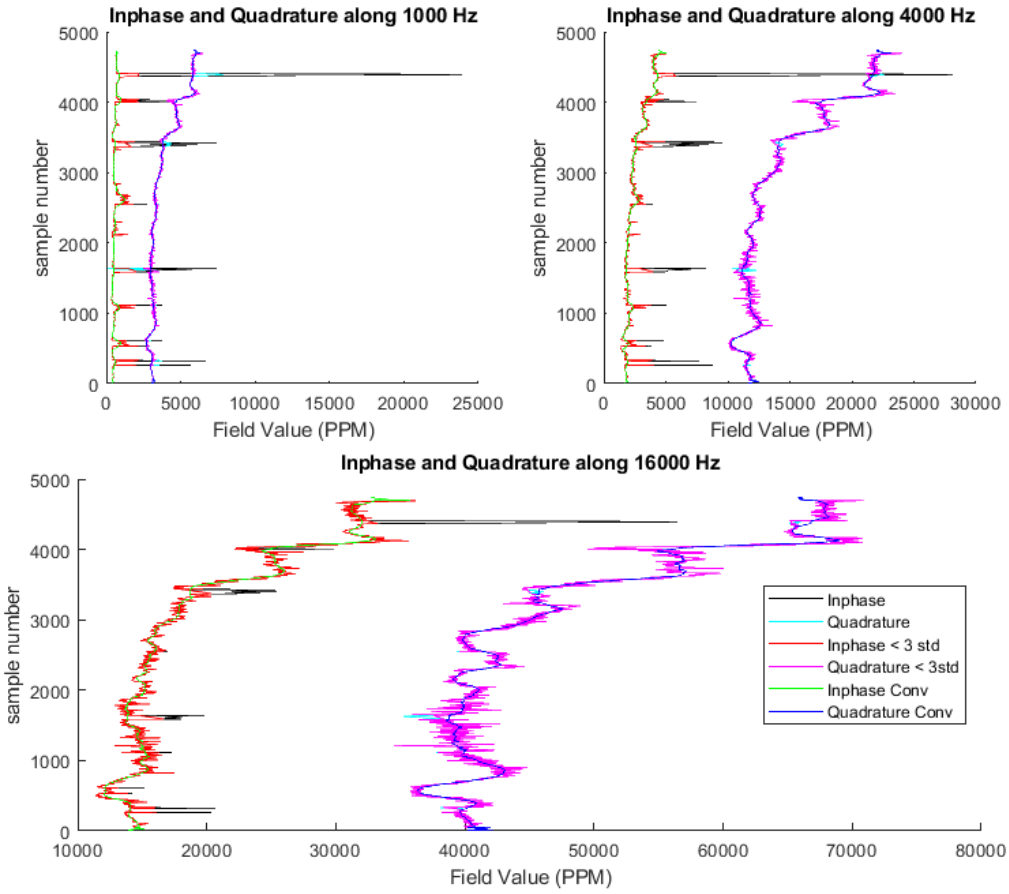

Figure 5.3: EM data reduction and smoothing in Seven Palm System on April 06, 2019.

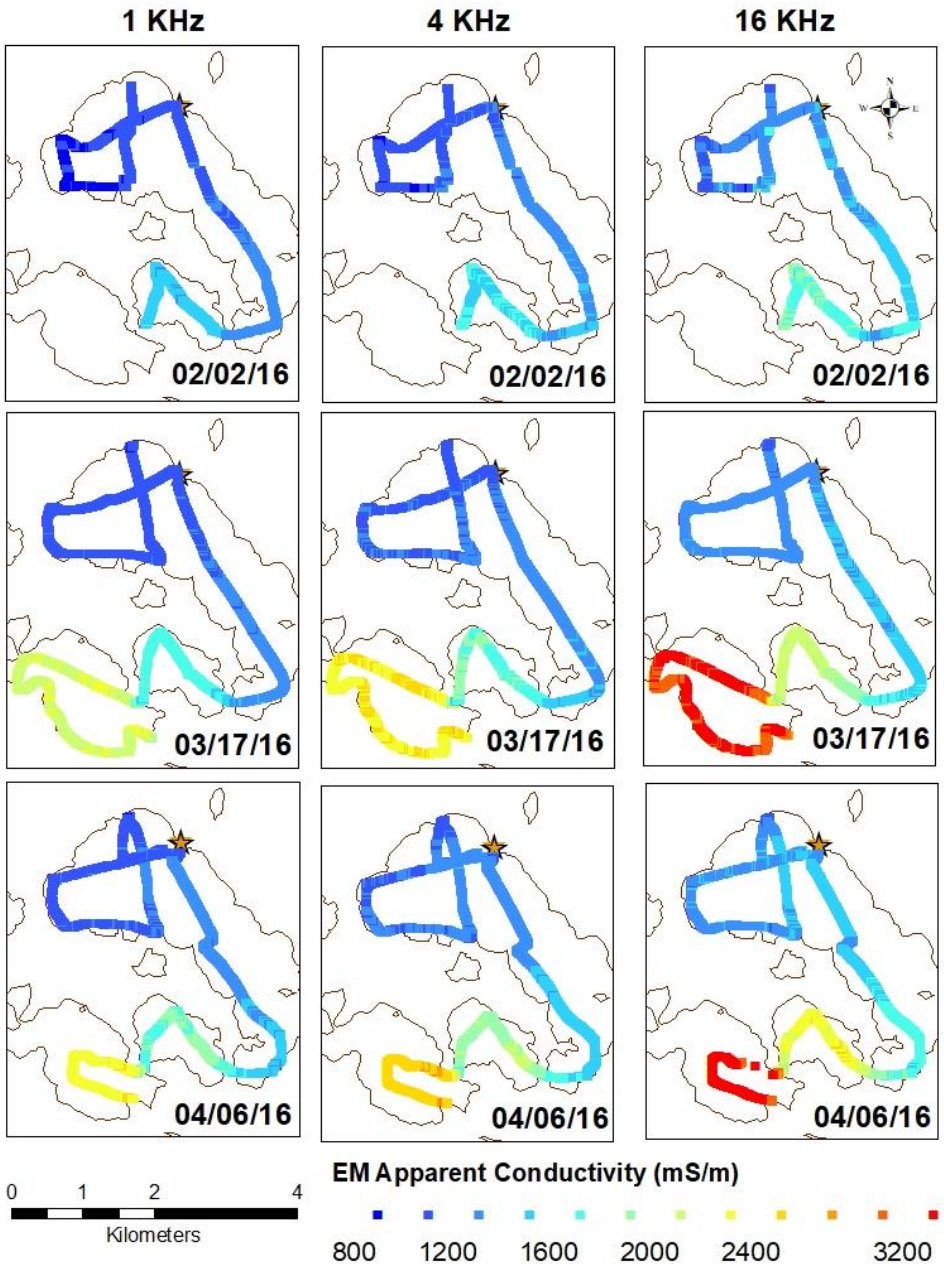

Figure 5.4: Map of apparent conductivities at 1, 4, and 16 KHz in 2016 in Seven Palm System, Middle Lake, and Monroe Lake. The 1 and 4 KHz data represents the average surface water and lake bottom conductivity and the 16 KHz data represents the surface water conductivity.

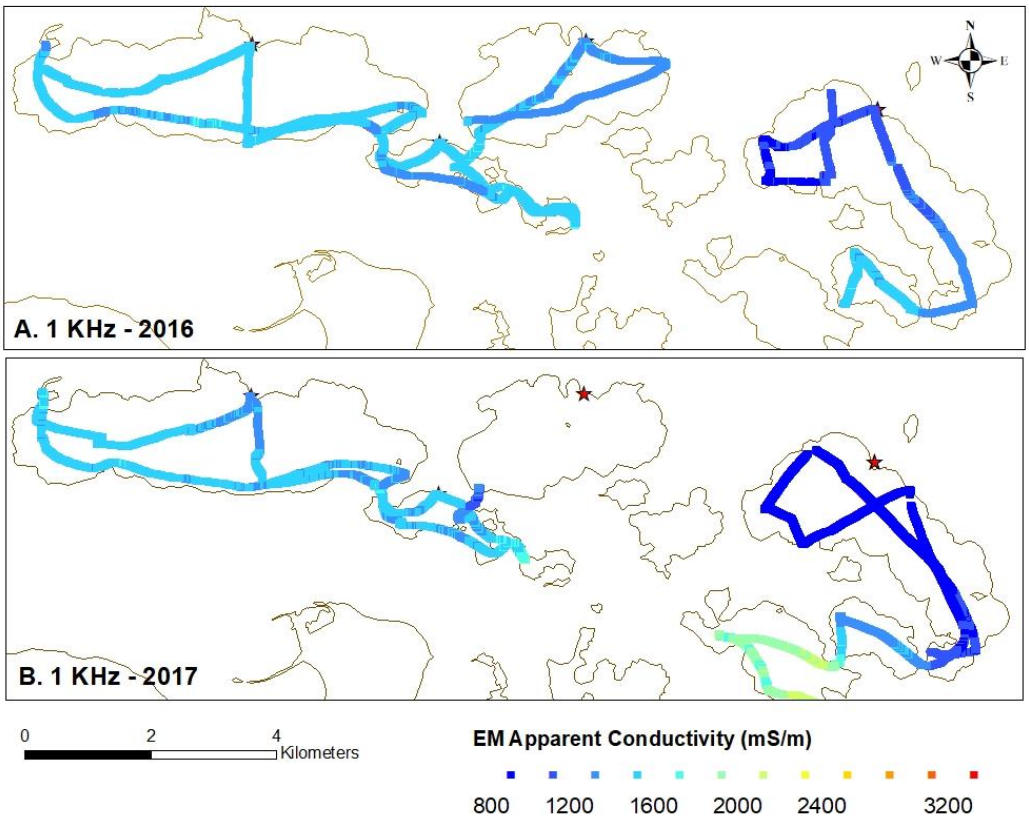

Figure 5.5: Map of apparent conductivities at 1 KHz in West Lake and Seven Palm system. In West Lake, the data was collected on January 25, 2016, and February 10, 2017. In Seven Palm, the data was collected on February 06, 2016, and January 20, 2017.

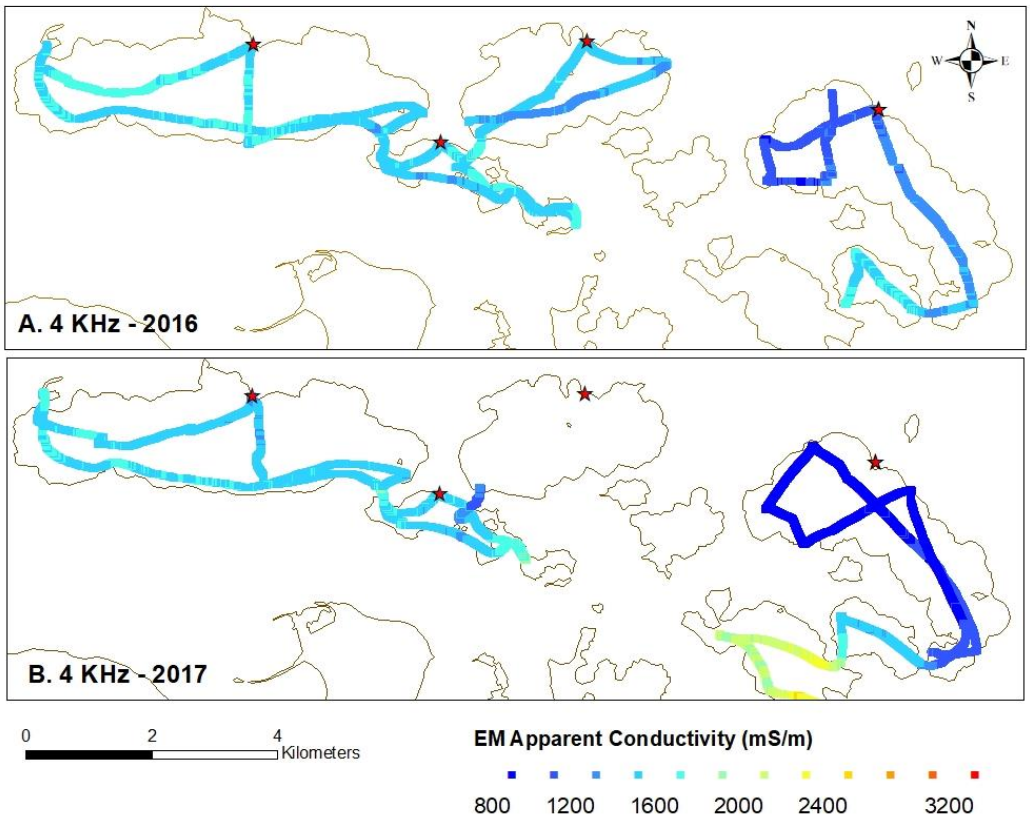

Figure 5.6: Map of apparent conductivities at 4 KHz in West Lake and Seven Palm system. In West Lake the data was collected on January 25, 2016 and February 10, 2017. In Seven Palm the data was collected in February 06, 2016 and January 20, 2017.

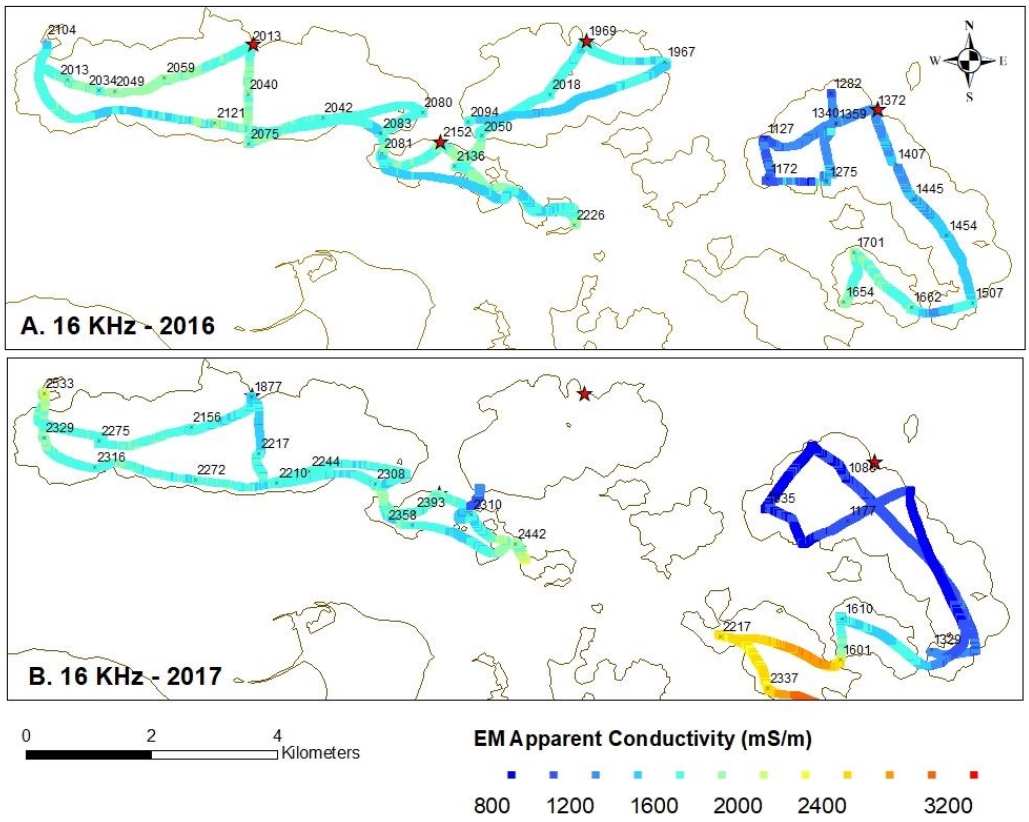

Figure 5.7: Map of apparent conductivities at 16 KHz in West Lake and Seven Palm system. In West Lake, the data was collected on January 25, 2016, and February 10, 2017. In Seven Palm, the data was collected on February 06, 2016, and January 20, 2017.

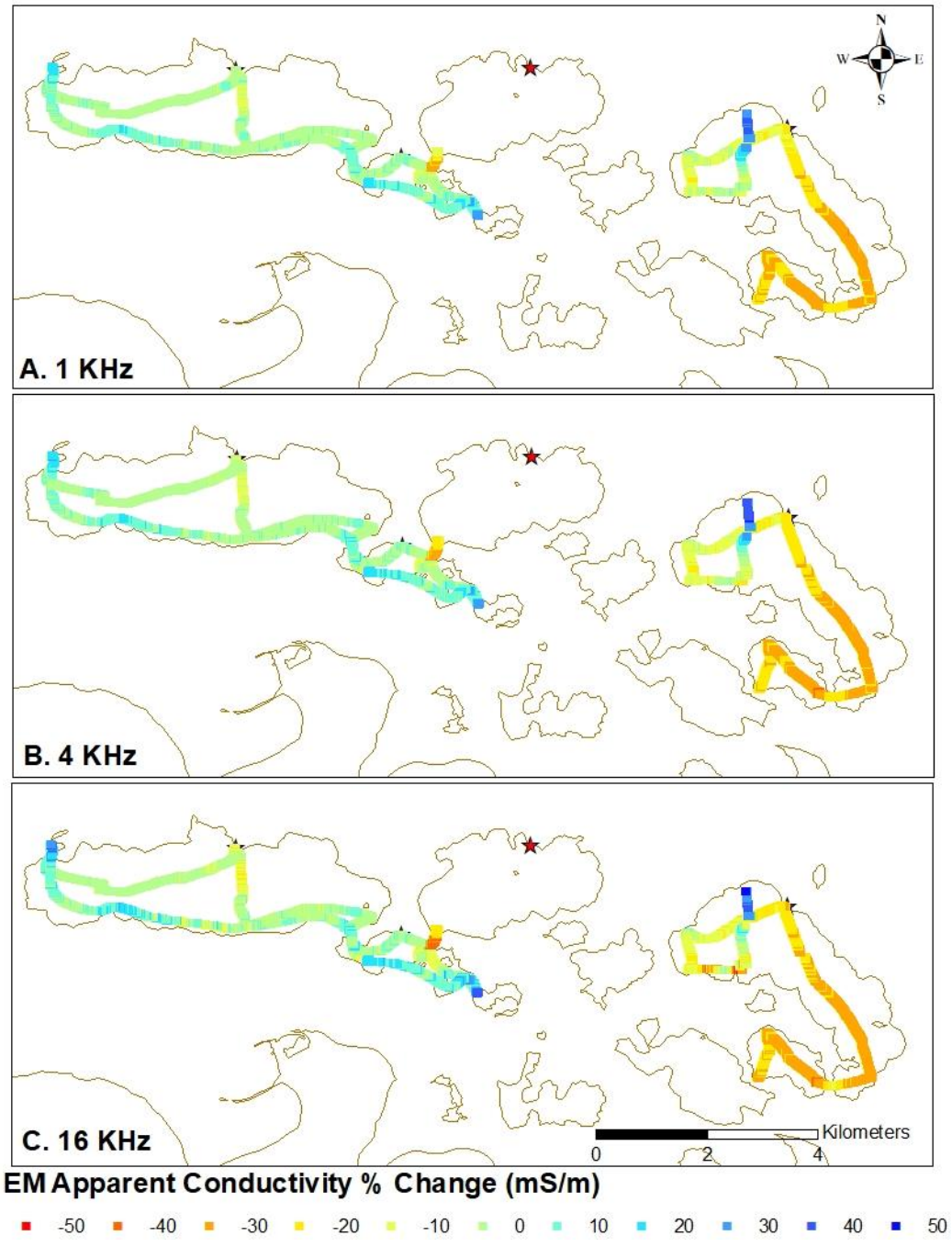

Figure 5.8: Apparent conductivity percent change between 2017 to 2016 in West Lake and Seven Palm System

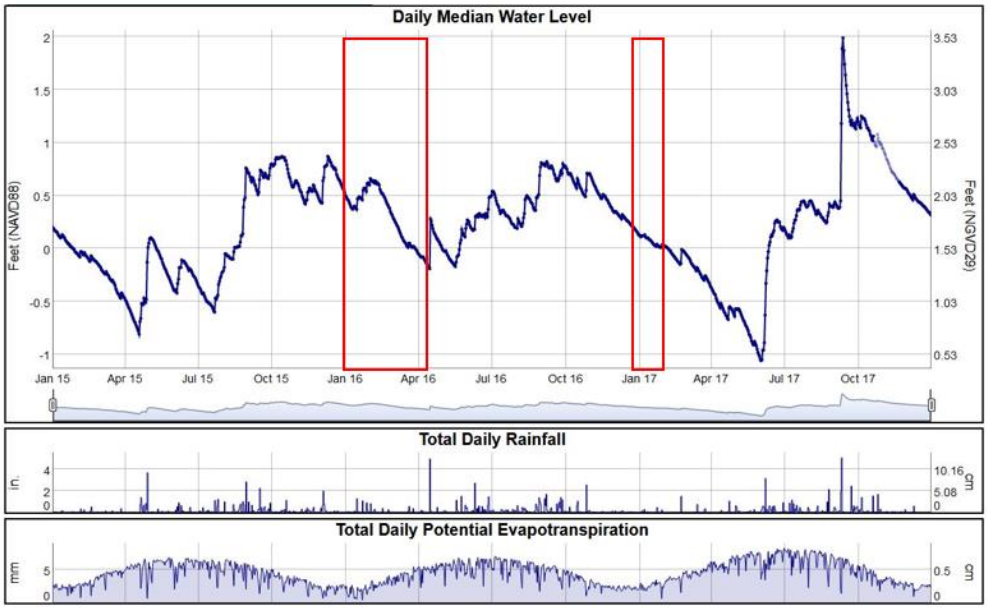

Figure 5.9: Water level, Rainfall and Evapotranspiration data between January 2015 to December 2017, at the NCL gage station, Everglades National Park. The red rectangle indicates the EM Survey period in 2016 and 2017. The data is found from the Everglades Depth Estimation Network (EDEN), USGS website *http://sofia.usgs.gov/eden/station.php*

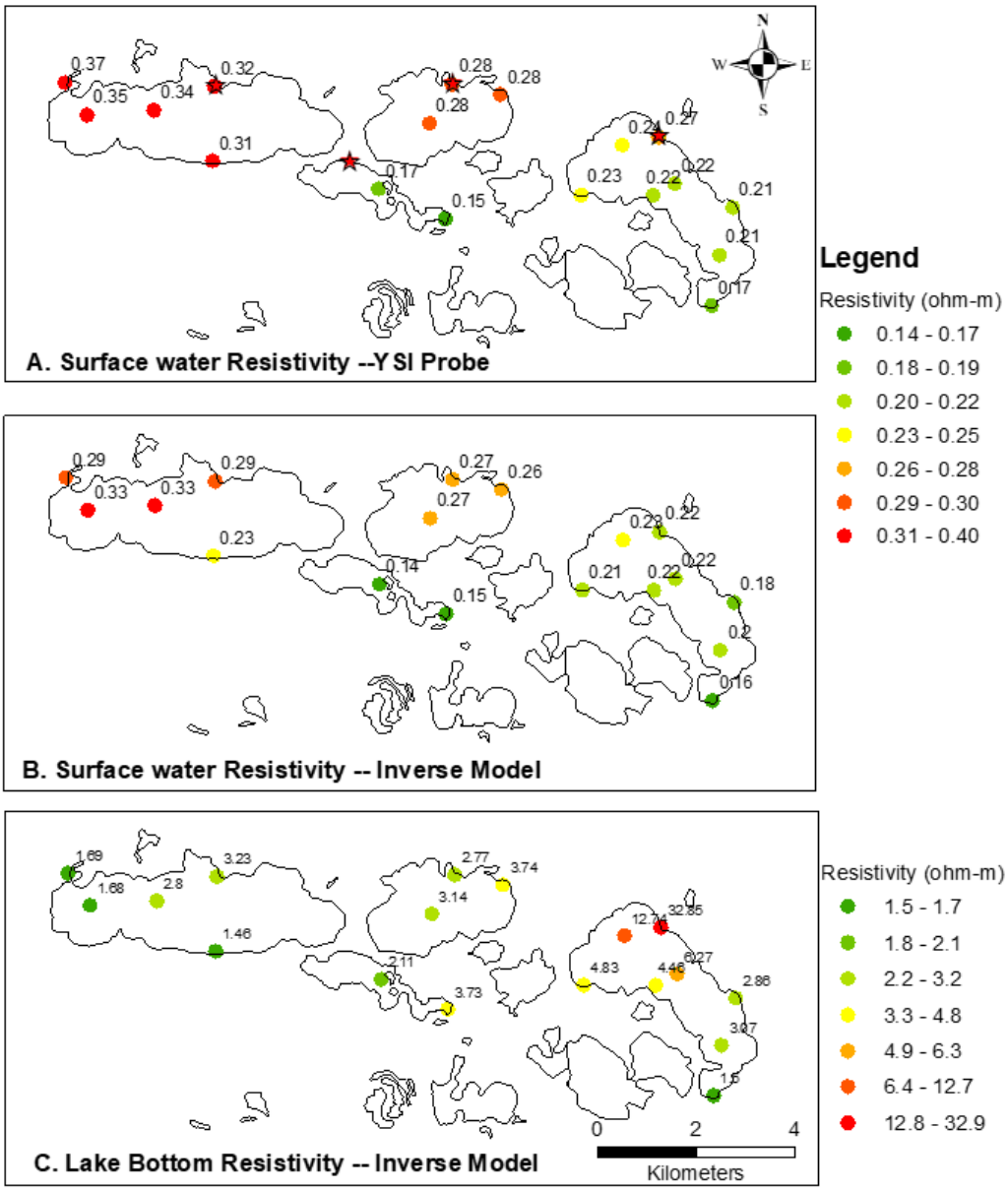

Figure 5.10: Resistivity in West Lake and Seven Palm. (a). surface water using YSI Probe. (b). Surface water from the Inverse model c. Lake bottom Resistivity from the Inverse model.

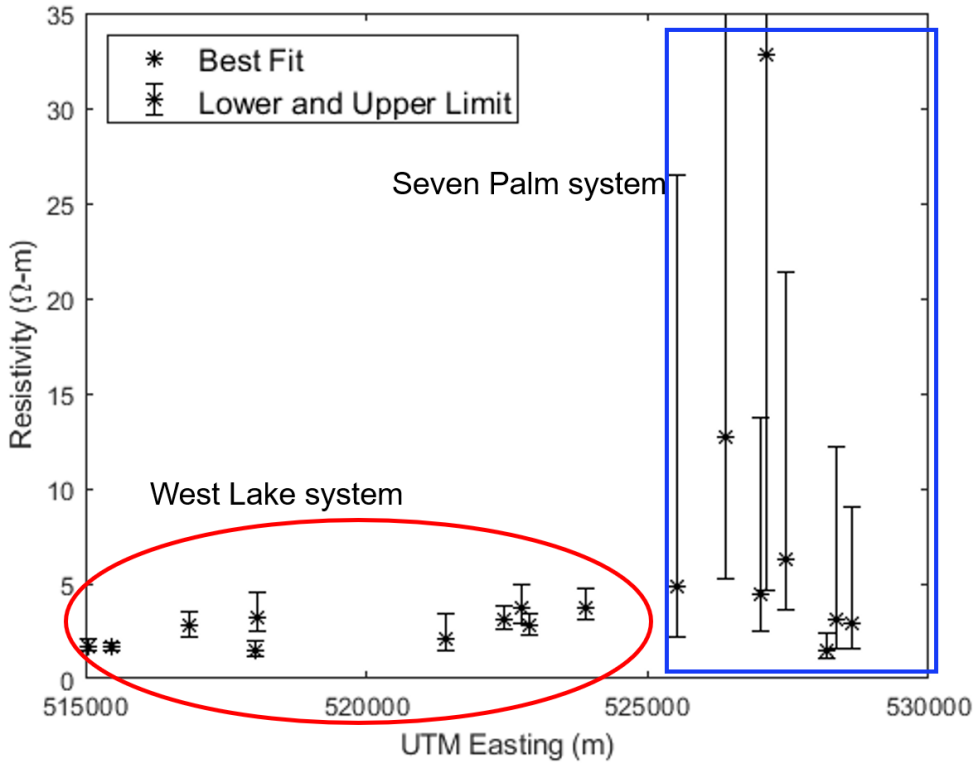

Figure 5.11: Inverted resistivity model with the lower and upper acceptable limits of equivalence analysis. West Lake system is located between 515000 to 525000 m and the Seven Palm system is located between 525000 to 530000 m.

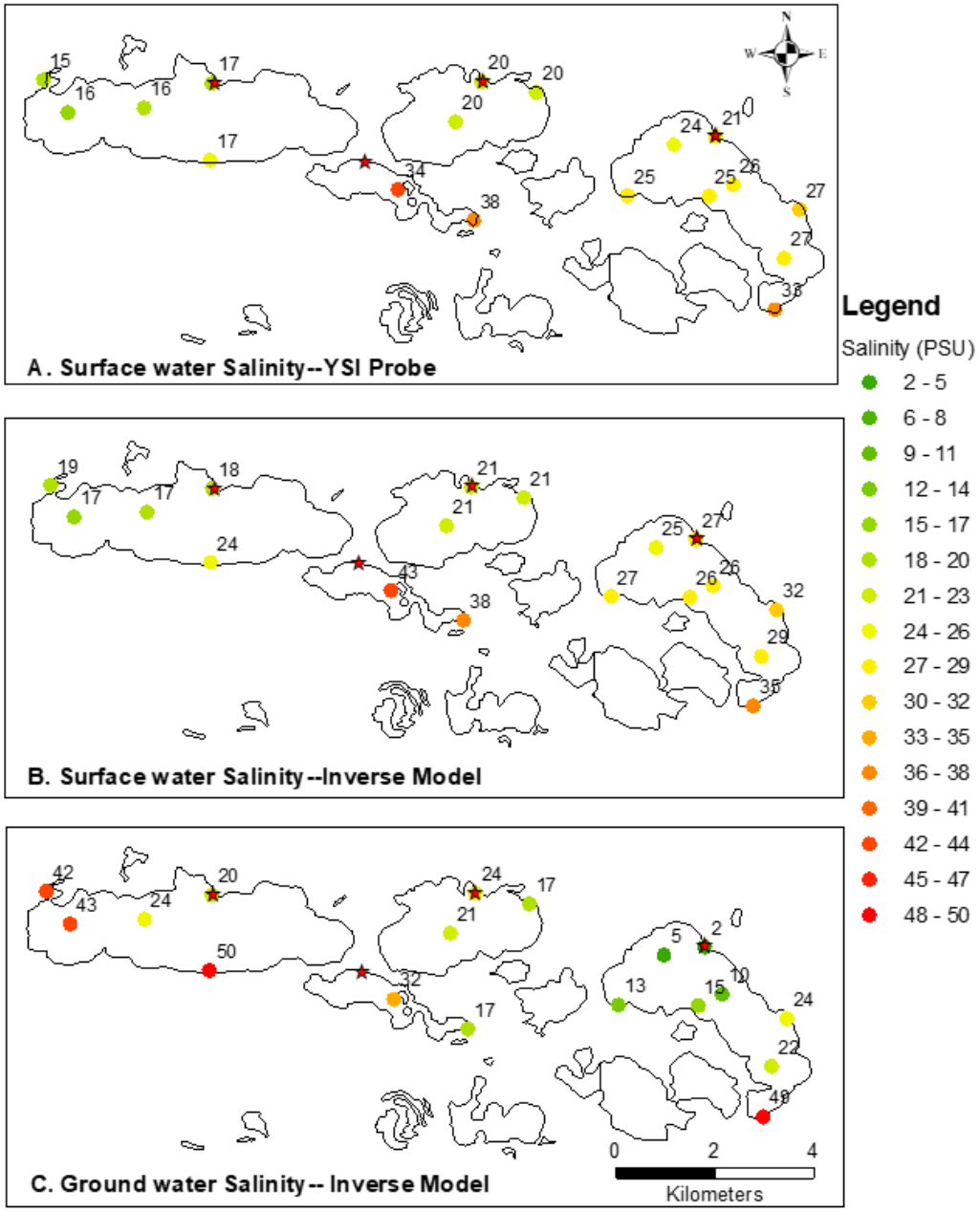

Figure 5.12: Salinity in West Lake and Seven Palm. (a). surface water using YSI Probe (b). surface water from the Inverse model (c). Groundwater from the Inverse model

Appendices

Appendix 3A

Vertical Sounding Curve along Profile B1 in January 2018: The Occam's Inverted model has a characteristic of K-Type curves. The location from the ERT starting point at a. 27 m, b. 55 m, c. 83 m, d. 111 m, e. 139 m, f. 167 m, and g. 195m.

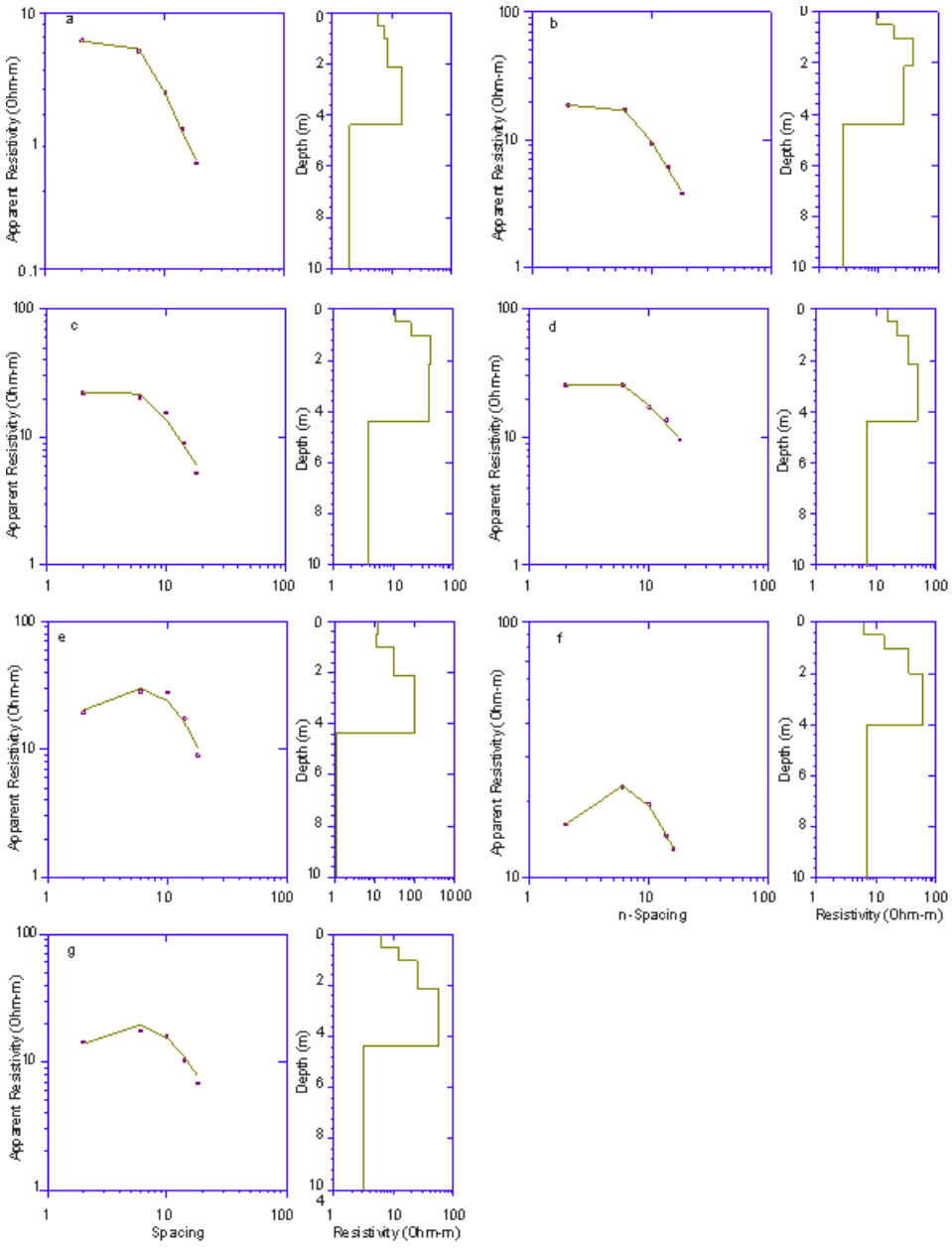

Vertical sounding curve along Profile B1 in December 2018: The Occam's Inverted model has an inclination to Q-Type. The location from the ERT starting point at a. 27 m, b. 55 m, c. 83 m, d. 111 m, e. 139 m, f. 167 m, and g. 195m.

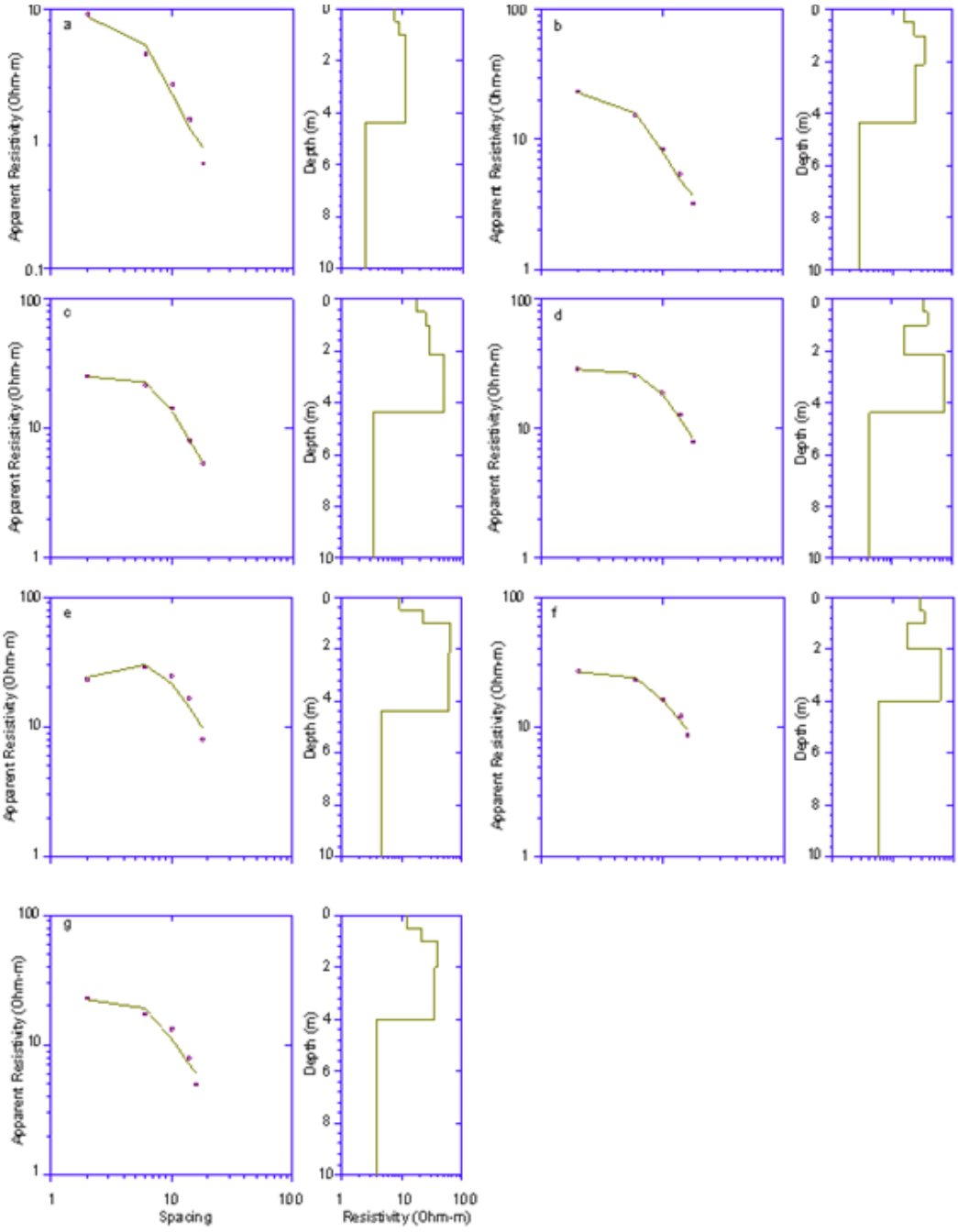

Appendix 4A

A comparison of four different inversion scenario in West Lake (WL) on July 15, 2019. WL#1 (a). Free model, (b). Constrained water depth, (c). Constrained water column resistivity, and (d). Constrained water depth and resistivity model. WL#2 (e). Free model, (f).Constrained water depth, (g). Constrained water column resistivity, and (h). Constrained water depth and resistivity model. WL#3 (I). Free model, and (j). Constrained water depth.

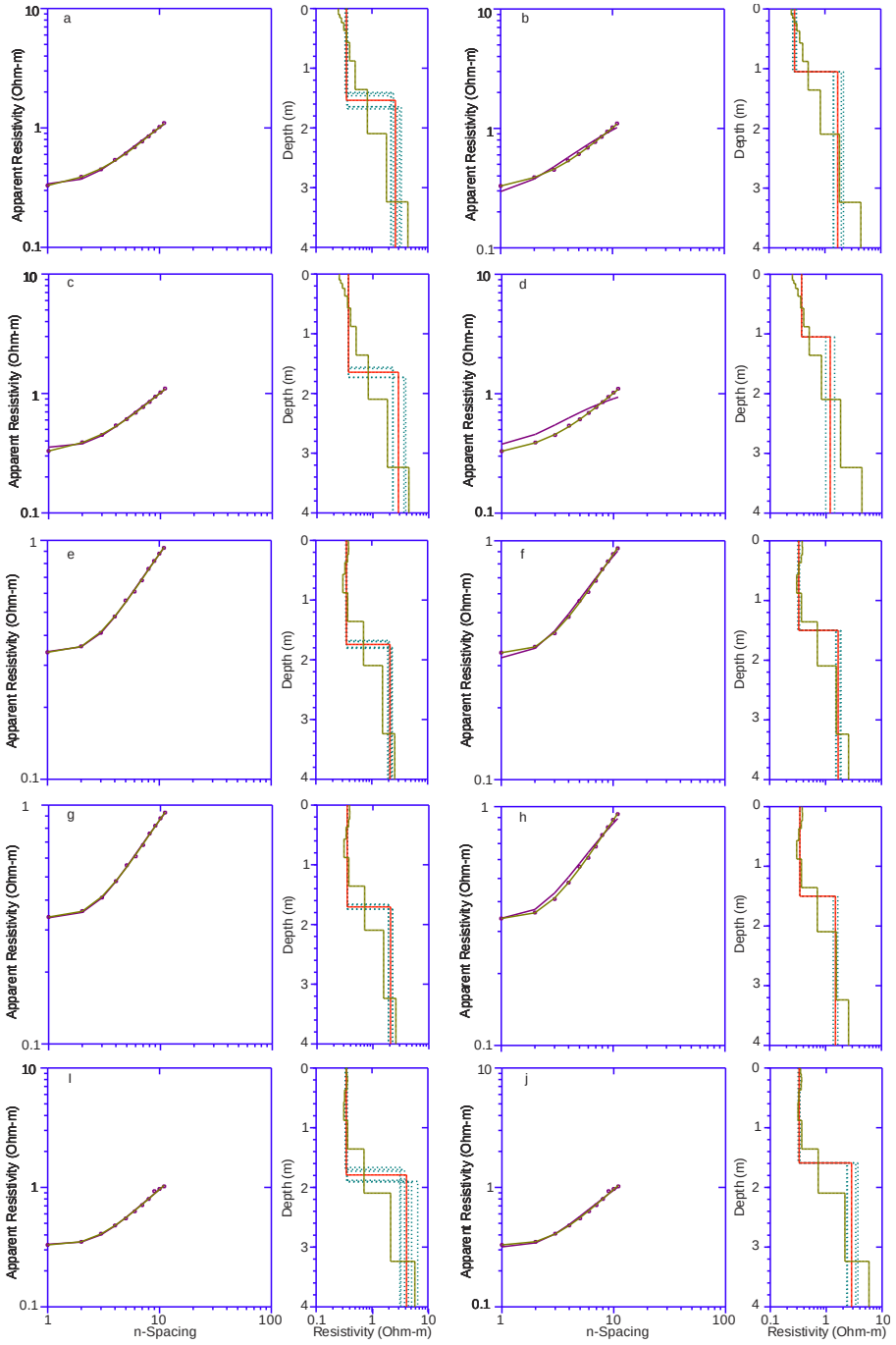

A comparison of four different inversion scenario in West Lake. WL#3 (a). Constrained water column resistivity, and (b). Constrained water depth and resistivity model. WL#4 (c). Free model, (d). Constrained water depth, (e). Constrained water column resistivity, and (f). Constrained water depth and resistivity model. WL#5 (g). Free model, (h). Constrained water depth, (I). Constrained water column resistivity, and (j). Constrained water depth and resistivity model.

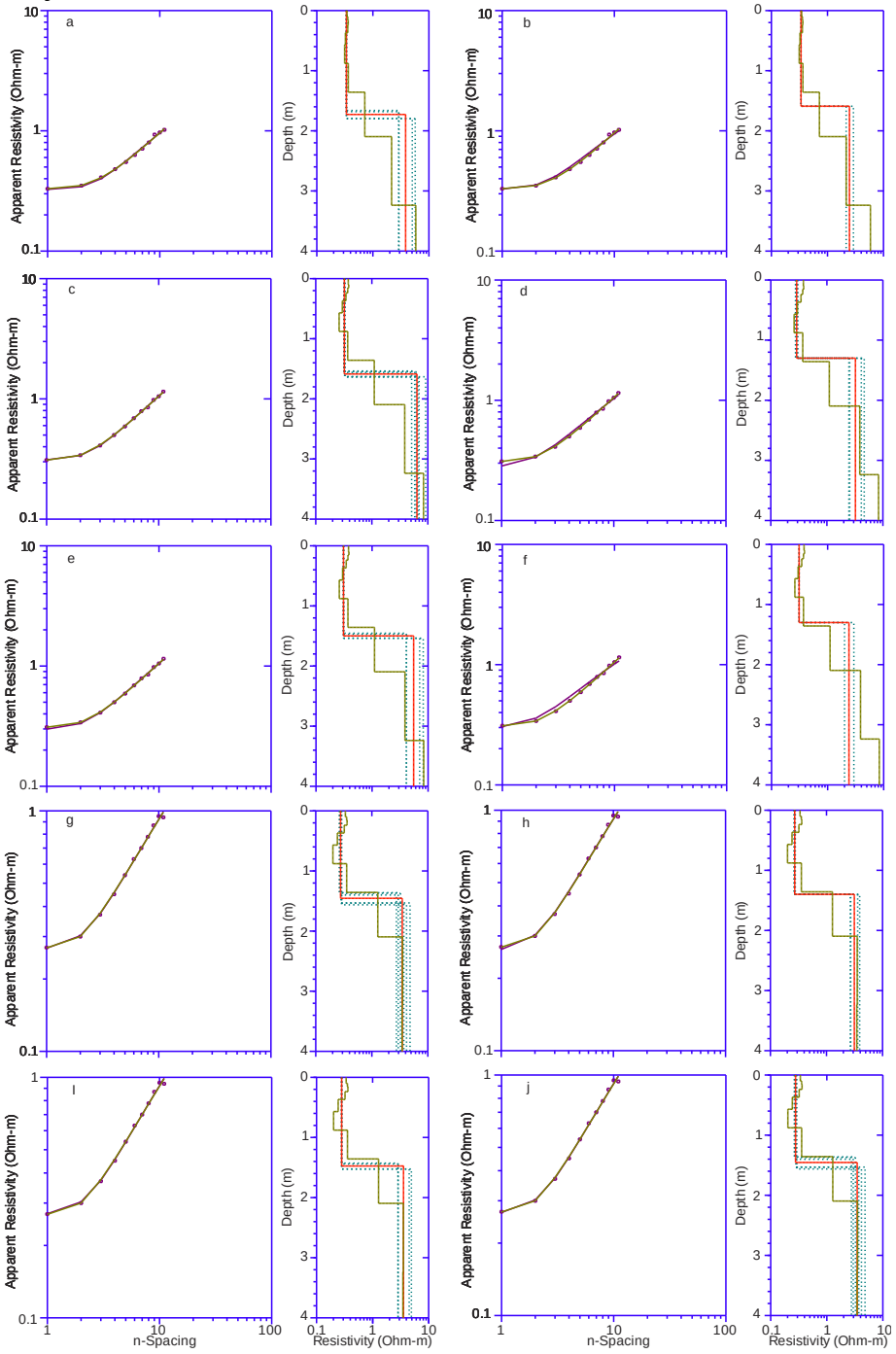

A comparison of four different inversion scenario in West Lake. WL#6 (a). Free model, (b). Constrained water depth, (c). Constrained water column resistivity, and (d). Constrained water depth and resistivity model. WL#7 (e). Free model, (f). Constrained water depth, (g). Constrained water column resistivity, and (h). Constrained water depth and resistivity model. WL#8 (I). Free model, and (j). Constrained water depth.

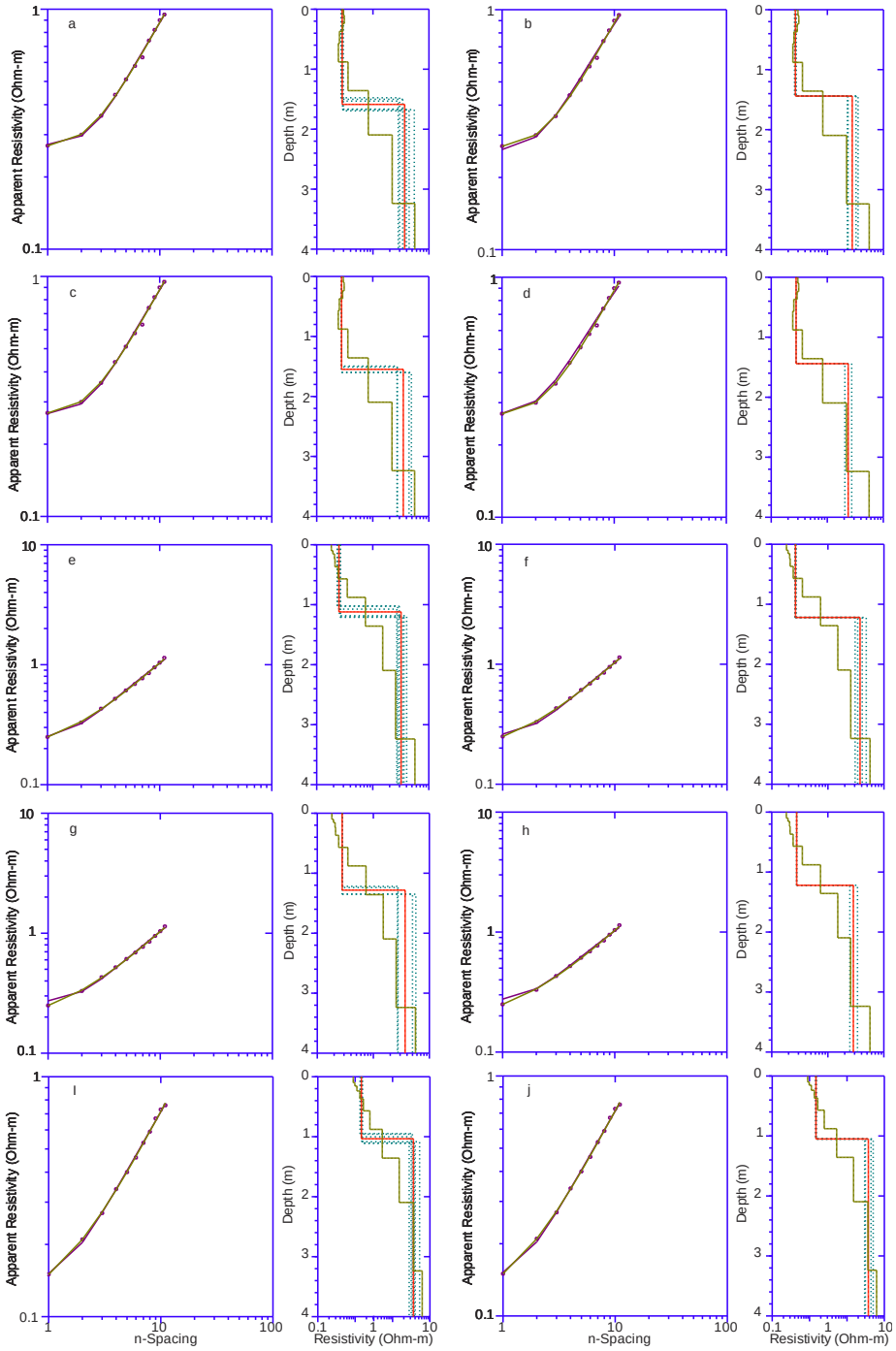

A comparison of four different inversion scenario in West Lake. WL#8 (a). Constrained water column resistivity, and (b). Constrained water depth and resistivity model. WL#9 (c). Free model, (d). Constrained water depth, (e). Constrained water column resistivity, and (f). Constrained water depth and resistivity model. WL#10 (g). Free model, (h). Constrained water depth, (I). Constrained water column resistivity, and (j). Constrained water depth and

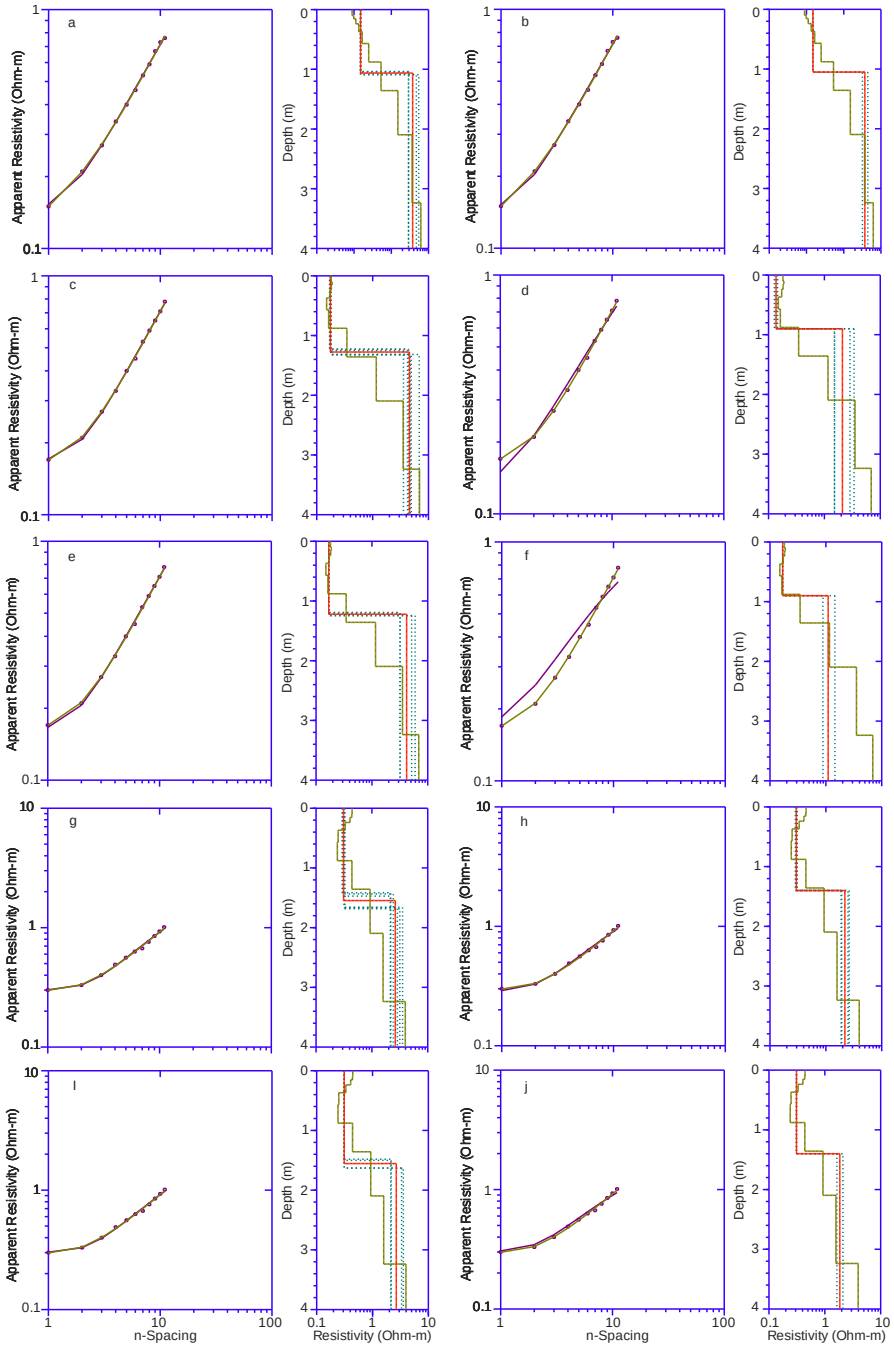

Field data measurements in the West Lake, the Seven palms, and the Mrazek Pond

Site Name	Date	Easting (m)	Northing (m)	Azimuth (°)	Depth 1 (m)	Depth 7 (m)	Depth 14 (m)	Salinity (PSU)	Temperature (°C)	Conductivity (µS/cm)	Resistivity (ohm.m)
WL dock	6/06/2019	515096.3	2788680	N/A	0.89	1	1.05	14.75	30.6	27077	0.36
WL dock	6/14/2019	515096.3	2788680	N/A	1	1	1	14.9	29.6	26793	0.37
SP01	7/10/2019	527113.1	2787601	130	1.08	1.07	1.12	21.1	30.6	37430	0.27
SP02	7/10/2019	526371.3	2787435	130	1.5	1.5	1.5	24.3	30.6	42544	0.24
SP03	7/10/2019	525537	2786428	140	1.2	1.23	1.22	24.5	31.3	43454	0.23
SP04	7/10/2019	527004.7	2786421	130	1.49	1.5	1.48	25.2	31.4	44667	0.22
SP05	7/10/2019	527442.5	2786651	130	1.64	1.64	1.6	25.9	31	45373	0.22
SP06	7/10/2019	528629	2786166	160	1.22	1.22	1.35	26.5	31.8	47050	0.21
SP07	7/10/2019	528350.6	2785200	140	1.6	1.6	1.6	27.3	31.3	47846	0.21
SP08	7/10/2019	528193.2	2784181	140	1.2	1.2	1.25	32.8	33.3	58499	0.17
WL01	7/15/2019	515034.8	2788703	140	1.05	1.05	1.1	14.8	31.1	27338	0.37
WL02	7/15/2019	515477.5	2788047	140	1.45	1.5	1.5	15.8	30.7	28796	0.35
WL03	7/15/2019	516843.4	2788143	132	1.56	1.59	1.52	16.2	30.6	29545	0.34
WL04	7/15/2019	518065.7	2788636	132	13.5	1.3	1.3	16.6	33.1	31590	0.32
CL05	7/15/2019	522450	2787876	150	1.4	1.4	1.4	20.1	30.4	36322	0.28
CL06	7/15/2019	522910	2788672	150	1.44	1.44	1.4	19.7	31.6	35925	0.28
CL07	7/15/2019	523895.6	2788461	150	1.2	1.22	1.28	19.6	32	35940	0.28
LL08	7/15/2019	522771.6	2785938	145	1.05	1.05	1.1	38.4	34.3	68458	0.15
LL09	7/15/2019	521414.4	2786542	123	0.85	0.9	0.9	33.5	33	59195	0.17
WL10	7/15/2019	518035.5	2787114	105	1.39	1.4	1.43	17.1	32.6	32035	0.31
WL dock	8/16/2019	515096.3	2788680	N/A	1.29	1.2	1.31	12.9	30.1	23710	0.42
Mrazek Pond	8/17/2019	5150639	2785738	N/A	0.8	0.77	0.87	4.4	30.4	8732	1.14

A comparison of the constrained and unconstrained free inversion models in Westlake on July 15, 2019. The bold numbers indicate the value was fixed during inversion.

No	Inverse Model Cases	Water Column						Sea Bottom		
1		**Rho 1**	**Range**	**% Error**	**Depth**	**Range**	**% Error**	**Rho 2**	**Range**	**RMS**
	Free Model	0.35	0.33-0.37	2.78	1.54	1.41-1.68	-46.67	2.63	2.18-3.36	2.38
	Constrained depth	0.29	0.27-0.31	19.44	**1.05**			1.69	1.41-2.15	6.12
	Constrained resistivity	**0.36**			1.64	1.56-1.73	-56.19	2.86	2.27-3.86	2.78
	Constrained depth and resistivity	**0.36**			**1.05**			1.19	0.99-1.42	13.45
2	**Free Model**	0.35	0.35-0.36	0	1.74	1.68-1.81	16.00	2.12	1.94-2.33	1.03
	Constrained depth	0.33	0.32-0.34	5.71	**1.50**			1.68	1.52-1.89	2.7
	Constrained resistivity	**0.35**			1.71	1.66-1.75	-14.00	2.07	1.89-2.26	1.12
	Constrained depth and resistivity	**0.35**			**1.50**			1.50	1.37-1.65	3.78
3	**Free Model**	0.35	0.33-0.36	-2.94	1.79	1.67-1.91	-12.58	4.15	3.16-6.57	2.11
	Constrained depth	0.33	0.32-0.34	2.94	**1.59**			2.84	2.33-3.68	3.12
	Constrained resistivity	**0.34**			1.73	1.66-1.80	-8.81	3.83	2.89-5.69	2.29
	Constrained depth and resistivity	**0.34**			**1.59**			2.46	2.15-2.90	3.64
4	**Free Model**	0.32	0.32-0.33	-3.23	1.59	1.54-1.64	-22.31	6.38	5.13-9.12	1.11
	Constrained depth	0.29	0.28-0.30	6.45	**1.30**			3.23	2.47-4.63	4.04

	Constrained resistivity	**0.31**			1.50	1.45-1.54	-15.38	5.51	4.08-8.17	1.79
	Constrained depth and resistivity	**0.31**			**1.30**			2.40	2.00-2.94	5.62
5	**Free Model**	0.28	0.26-0.29	0	1.46	1.36-1.56	-4.29	3.48	2.75-4.81	2.08
	Constrained depth	0.27	0.26-0.28	3.57	**1.40**			3.14	2.66-3.91	2.22
	Constrained resistivity	**0.28**			1.48	1.43-1.53	-5.71	3.56	2.83-4.91	2.10
	Constrained depth and resistivity	**0.28**			**1.40**			2.65	2.36-3.07	2.91
6	**Free Model**	0.28	0.27-0.29	0	**1.59**	1.48-1.69	-10.42	3.68	2.83-5.47	2.05
	Constrained depth	0.27	0.26-0.28	3.57	**1.44**			2.77	2.27-3.53	2.75
	Constrained resistivity	**0.28**			1.55	1.49-1.60	-7.62	3.51	2.72-4.90	2.13
	Constrained depth and resistivity	**0.28**			**1.44**			2.36	2.06-2.73	3.38
7	**Free Model**	0.25	0.23-0.26	10.71	1.12	1.02-1.21	8.20	3.20	2.69-4.03	2.02
	Constrained depth	0.26	0.26-0.27	7.14	**1.22**			3.74	3.06-4.82	2.46
	Constrained resistivity	**0.28**			1.28	1.22-1.35	-4.92	3.69	2.69-5.73	3.24
	Constrained depth and resistivity	**0.28**			**1.22**			2.85	2.47-3.38	3.81
8	**Free Model**	0.15	0.14-0.16	0	1.05	0.95-1.11	0	3.62	2.77-5.28	1.67
	Constrained depth	0.15	0.15-0.15	0	**1.05**			3.73	2.98-5.04	1.69
	Constrained resistivity	**0.15**			1.06	1.04-1.09	-0.95	3.74	2.90-5.47	1.74
	Constrained depth and resistivity	**0.15**			**1.05**			3.68	3.19-4.42	1.70

9	**Free Model**	0.17	0.17-0.18	0	1.28	1.23-1.32	-42.22	4.56	3.56-6.83	1.19
	Constrained depth	0.14	0.13-0.15	17.65	**0.90**			2.11	1.52-3.40	5.32
	Constrained resistivity	**0.17**			1.22	1.19 -1.24	-35.56	4.18	3.18-5.95	1.49
	Constrained depth and resistivity	**0.17**			**0.90**			1.10	0.89-1.45	12.08
10	**Free Model**	0.31	0.29-0.33	0	1.55	1.41-1.68	-10.71	2.63	2.14-3.54	2.52
	Constrained depth	0.30	0.29-0.31	3.23	**1.40**			2.19	1.87-2.62	3.07
	Constrained resistivity	**0.31**			1.55	1.48-1.63	-10.71	2.66	2.13-3.55	2.52
	Constrained depth and resistivity	**0.31**			**1.40**			1.85	1.65-2.12	4.26

Appendix 5A

Constrained resistivity model in Westlake System on July 15, 2019.

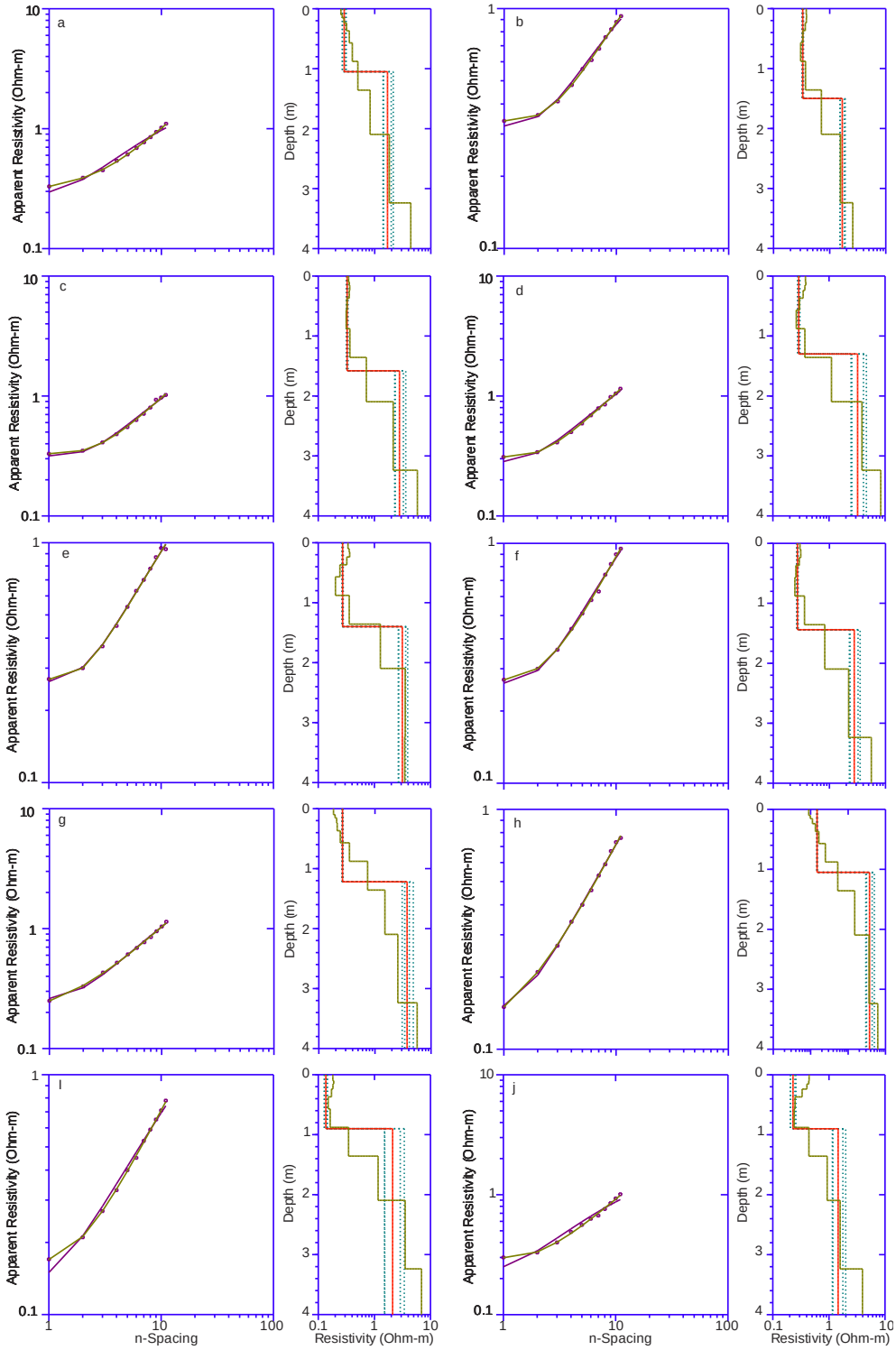

Constrained resistivity model in Seven Palm System on July 10, 2019. The outliers measurements represented by asterisks were masked during inversion

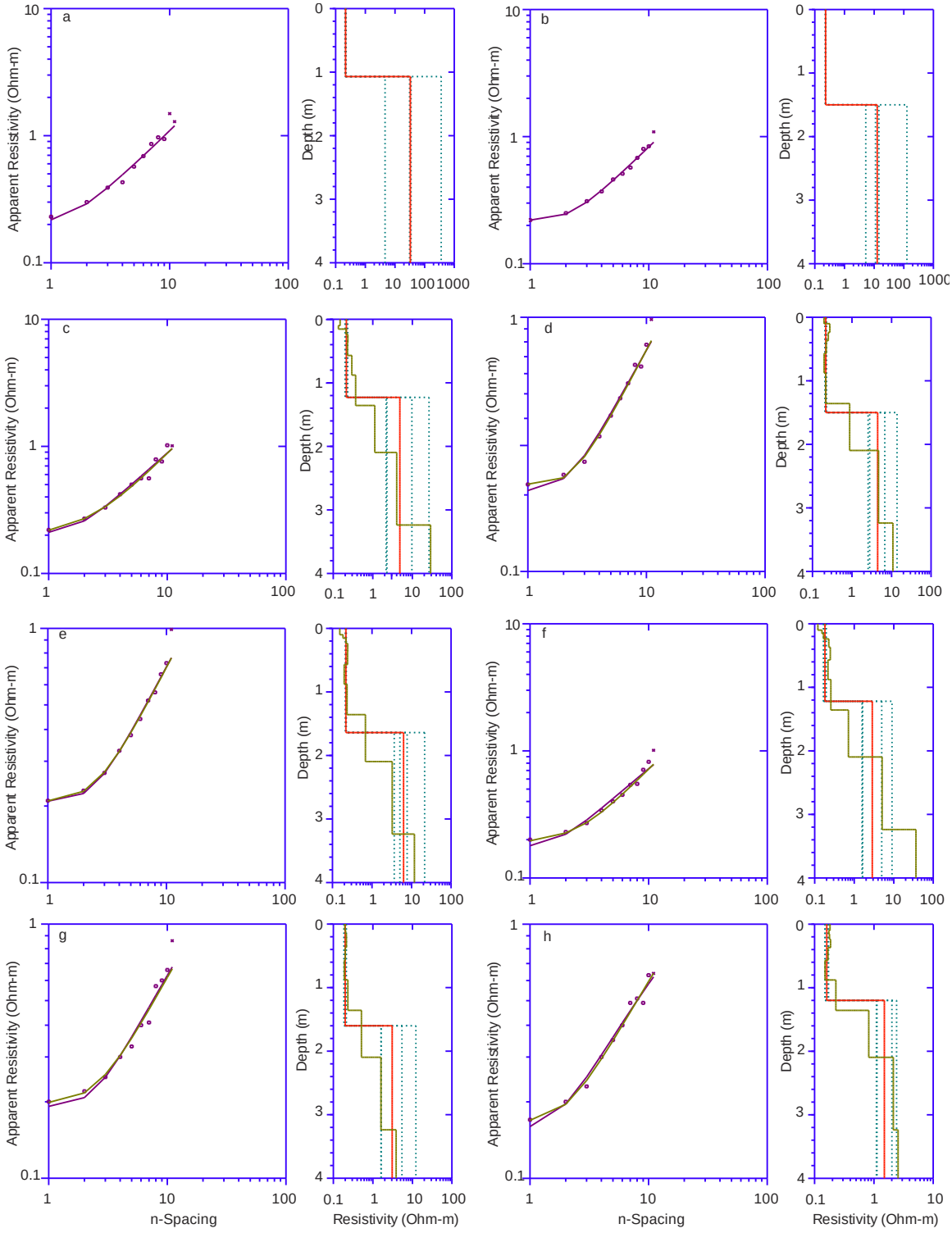

VITA

MICHAEL EYOB KIFLAI

Born, Asmara, Eritrea

2006-2011	B.Sc., Geology Eritrea Institute Technology Asmara, Eritrea
2010-2012	Environmental Technician SunRidge Gold Corp Asmara, Eritrea
2011-2015	Teaching Assistant Eritrea Institute of Technology Asmara, Eritrea
2015-2018	M.S., Geoscience Florida International University Miami, Florida
2015-2020	Ph.D., Geoscience Florida International University Miami, Florida
2019-2020	Dissertation Fellowship Award Florida International University Miami, Florida
2015-2020	Teaching Assistant Florida International University Miami, Florida

PUBLICATIONS AND PRESENTATIONS

Kiflai, M., D. Whitman, D.E. Ogurcak, and M.S. Ross (2019). *The effect of Hurricane Irma storm surge on the freshwater lens on Big Pine Key, Florida, using electrical resistivity tomography*, Estuaries and Coasts, 1-13.

Kiflai, M., D. Whitman, D.E. Ogurcak, and M.S. Ross (April 2019). *The effect of Hurricane Irma storm surge on the freshwater lens on Big Pine Key, Florida, using electrical resistivity tomography.* Paper presented at the meeting of the Greater Everglades Ecosystem Restoration (GEER), Coral Springs, Florida.

Kiflai, M., D. Whitman, D.E. Ogurcak, and M.S. Ross (December 2018). *The effect of Hurricane Irma storm surge on the freshwater lens on Big Pine Key, Florida, using electrical resistivity tomography.* Paper presented at the meeting of the American Geophysical Union (AGU), Fall meeting, Washington, D.C.

Kiflai, M., D. Whitman, R.M. Price, Tom A. Frankovich, J. Allen (December 2017). *Geophysical Characterization of Groundwater in the Mangrove Lakes Region of Everglades National Park.* Paper presented at the meeting of the American Geophysical Union (AGU), Fall meeting, New Orleans, Louisiana.

Kiflai, M., D. Whitman, R. M. Price, T.A. Frankovich, J. Allen (April 2017). *Hydrogeophysical Characterization of Groundwater in the Mangrove Lakes Region of Everglades National Park.* Paper presented at the meeting of the Greater Everglades Ecosystem Restoration (GEER), Coral Springs, Florida.

Kiflai, M., D. Whitman, R. M. Price, T.A. Frankovich, J. Allen (May 2017). *Hydro Geophysical Characterization and Imaging of Groundwater in the Mangrove Lakes Region of Everglades National Park.* Paper presented at the meeting of the Florida Coastal Everglades Long Term Ecological Research LTER (FCE LTER), Miami, Florida.